Erzeugung und Charakterisierung eines gepulsten, intensiven Neutronen- und Gamma-Strahls zur Anwendung in der Luftfrachtdurchleuchtung

Dissertation

zum Erlangen des akademischen Grades

doctor rerum naturalium
(Dr. rer. nat.)

im Fach: Physik

Spezialisierung: Experimentalphysik

eingereicht an der

Mathematisch-Naturwissenschaftlichen Fakultät
der Humboldt-Universität zu Berlin

von

MSc. Benjamin Bromberger

Präsidentin der Humboldt-Universität zu Berlin
Prof. Dr.-Ing. Dr. Sabine Kunst

Dekan der Mathematisch-Naturwissenschaftlichen Fakultät
Prof. Dr. Elmar Kulke

Gutachter/innen:

1. Prof. Dr. Andreas Jankowiak (Humboldt-Universität zu Berlin, Deutschland)
2. Prof. PhD. Ilan Mardor (Tel Aviv University, Israel)
3. Prof. Dr. rer. nat. Peter Michel (Universität Rostock, Deutschland)

Tag der mündlichen Prüfung: 26.11.2018

Generation and Characterization of a pulsed, intense Neutron- and Gamma-Beam to be used in Air Cargo Interrogation

A thesis in partial fulfillment of the requirements for a

doctor rerum naturalium
(Dr. rer. nat.)

in the subject: Physics

specialization: Experimental Physics

submitted at the

Mathematisch-Naturwissenschaftlichen Fakultät
of the Humboldt-Universität zu Berlin

by

MSc. Benjamin Bromberger

President of Humboldt-Universität zu Berlin
Prof. Dr.-Ing. Dr. Sabine Kunst

Dean of the Mathematisch-Naturwissenschaftlichen Fakultät
Prof. Dr. Elmar Kulke

Supervisors:

1. Prof. Dr. Andreas Jankowiak (Humboldt-Universität zu Berlin, Germany)
2. Prof. PhD. Ilan Mardor (Tel Aviv University, Israel)
3. Prof. Dr. rer nat. Peter Michel (Universität Rostock, Germany)

Date of oral exam: 26.11.2018

Selbständigkeitserklärung

Ich erkläre hiermit, dass ich die vorliegende Arbeit selbständig verfasst und nur unter Verwendung der angegebenen Quellen und Hilfsmittel angefertigt habe. Weiterhin erkläre ich, eine Dissertation in diesem Studiengebiet erstmalig einzureichen.

Bergisch Gladbach, den 22. Mai 2018 .....

Statement of authorship

I hereby state that I have completed this thesis on my own and that information which has been directly or indirectly taken from other sources has been noted as such. Furthermore, I state that neither this nor similar work in this field has previously been presented to an examination committee.

Bergisch Gladbach, February 22, 2019 .....

Kurzzusammenfassung

Die vorliegende Arbeit ist eingebettet in ein Projekt zur Entwicklung eines neuartigen Systems zur zerstörungsfreien und bildgebenden Untersuchung von Luftfracht. Hierbei soll im Gegensatz zu klassischen, auf Röntgenstrahlung basierten Systemen eine Durchleuchtung mittels Neutronen- und Gammastrahlung durchgeführt werden. Ein wichtiges Teilprojekt während des Projektes war die Entwicklung einer Strahlungsquelle, die in einem einsatzfähigen System z.B. auf einem Flughafen Verwendung finden kann. Die Entwicklung der Methode wurde im Beschleunigerlabor mithilfe eines Zyklotrons durchgeführt. Diese Strahlungsquelle ist einerseits nicht kompakt genug für den Einsatz am Flughafen, weiterhin liegt die Belichtungsdauer aufgrund der geringen Intensität bei der unwirtschaftlichen Zeit von mehreren Stunden. Desweiteren handelt es sich bei einem Zyklotron um einen komplexen Beschleuniger, der tiefreichende Kenntnis über das System zum Betrieb und zur Wartung verlangt.
Um diese Probleme zu lösen, wurde im Rahmen dieser Arbeit eine Strahlungsquelle entwickelt, die optimal auf die Anwendung angepasst ist. Die neue Quelle besteht aus vier Hauptkomponenten: Ein gepulster Deuteronenstrahl wird in einer Ionenquelle erzeugt und mittels eines niederenergetischen Strahltransportsystems zum Hauptbeschleuniger geführt. Dieser besteht aus einem Radiofrequenz Quadrupol (RFQ) mit einer finalen Energie von $6\,MeV$. Da für die Anwendung sehr kurze Pulse der Strahlung in der Größenordnung einiger Nanosekunden unabdingbar sind, musste eine neuartige Lösung zur Pulsung des Deuteronenstrahls gefunden werden, ohne die für die Anwendung notwendige Strahlladung pro Puls zu unterschreiten. Eine große Herrausforderung bestand hierbei im Zusammenspiel der kurzen Pulsdauer und hohen Pulsladung in Kombination mit der hohen Wiederholrate. Dieses wurde erreicht, indem ein spezielles Pulsungssystem innerhalb des Strahlentransportes zwischen Ionenquelle und RFQ eingefügt wurde. Dieses Pulsungssystem enthält neben einem strahlablenkenden auch ein strahlbündelndes Element. Der Deuteronenstrahl wird hinter dem RFQ auf ein Target geführt, welches aus Borcarbid (B_4C) besteht.
In dieser Arbeit wird das komplette physikalische Design der Strahlungsquelle diskutiert sowie Simulationen zu dem Pulsungssystem bzw. dem RFQ-Beschleuniger präsentiert. Weiterhin werden Proof-of-Principle Experimente beschrieben, die mithilfe eines Prototypen-Pulsungssystems entwickelt im Rahmen dieser Arbeit und gefertigt von der RI Research Instruments GmbH an einem speziell für diesen Zweck errichteten Teststands durchgeführt wurden. Um die Studie zu vervollständigen wurden mehrere Experimente sowohl an der Beschleunigeranlage der Physikalisch- Technischen Bundesanstalt (PTB) Braunschweig als auch am RFQ Beschleuniger der Nuclear Energy Corporation of South Africa (NECSA) in Pelindaba durchgeführt, um das Target zu optimieren und das erzeugte Strahlungsfeld zu charakterisieren.

Abstract

This thesis is embedded into a broader research project whose goal is to develop a novel, non-destructive imaging system to be employed for air freight security. In contrast to state-of-the-art X-ray based systems, the screening will be performed employing neutron- and gamma-radiation based techniques.

One of the critical issues in this project was the absence of an adequate particle source to be applied at, e.g., an airport environment. The method as well as the measuring equipment development took place at an accelerator lab that incorporates a cyclotron accelerator. This source is, on one hand, not compact enough to be deployed in an airport environment. Furthermore, the beam intensity is only sufficient to produce reasonable $n - \gamma$ images after an irradiation time of several hours. Additionally, a cyclotron is a rather complex accelerator that requires extensive knowledge about the system for operation and maintenance.

To deal with these issues, a new type of source was developed during this work. The new source consists of four main parts: A pulsed deuteron beam is formed in an ion source (IS) and is fed, via a matching low energy beam transport system (LEBT), into the main accelerator. The latter comprises a radio frequency quadrupole (RFQ) that produces a deuteron beam with a final energy of $6\,MeV$. Since pulsing of this beam in the regime of several nanoseconds is mandatory for the application, a novel solution had to be found to apply the required pulsing scheme, without undershoot the required beam charge per pulse. A major challenge in doing so was the combination of pulse length, high bunch charge as well as high repetition rate. This could be achieved by adding a pulsing system in between the LEBT section and RFQ: it consists of a beam-deflection, as well as a beam-bunching element. The deuteron beam is ultimately directed to a wobbling, plasma sprayed boron carbide (B_4C) target.

This work focuses on an entire physical design as well as simulation work of the pulsing system and RFQ. Furthermore, proof-of-principle experiments concerning a prototype of the pulsing system developed in the framework of this thesis and manufactured by RI Research Instruments GmbH could be performed at a test bench dedicated to this project. To round up the study, the suitability of the target and target reaction was demonstrated during multiple experiments performed at Physikalisch- Technische Bundesanstalt (PTB) at Braunschweig as well as the Nuclear Energy Corporation of South Africa (NECSA) in Pelindaba.

Contents

1 Introduction

Terrorism is one of the major global threats in recent years and civil aviation is still a target for terrorist activities. Although passenger security was dramatically since the 1990s (by implementing luggage and passenger screening), the security chain for air freight was considered rather vulnerable: This is particularly worrying since, 25-60 % of all air freight is shipped on passenger flights as so called bellyhold cargo [1][2][3] (from 2006 until March 2013). However, no freight on such planes shipped from the European Union was security screened at all, if the shipper declared himself as a so called known shipper at the logistics company by filling out a form to confirm his own security clearance [4]. Since March 2013, at least one additional regulatory authorization is necessary to apply for a known shipper (or known Consignor) approval [5]. In the USA, before 2007 at maximum 35% of all air freight was screened [6]. Although the US government passed a law in 2007 which required all inbound air freight transported on passenger flights to be screened 100 % at the airport of departure by the end of August 2010 [7], in June 2012, the Transport Security Administration (TSA) recognized the European air-cargo security procedure as a reasonable approach [8].

One of the principal aviation-cargo screening techniques still widely employed is X-ray scanning. Established in the middle of the 20th century, several optimizations to the cargo scanners have been implemented the recent years: On the one hand, new X-ray scanners are now capable of producing pictures under multiple angles or are even capable of performing entire computer tomography of the inspected goods. On the other hand, radiography at multiple electron beam energies permits rough electron density discrimination differentiating between organic materials and metals (compare figure 1.1[1]). Nevertheless, detection efficiency for e.g. explosives employing X-ray scanners is highly dependent on the status (skill, concentration, stamina, etc.) of the operator, since shape recognition by the human eye is the sole signature that can be brought into play. Pattern recognition or other artificial intelligence is not yet being employed in these systems.

[1]Private Communication - Israel Police Bomb Disposal Division

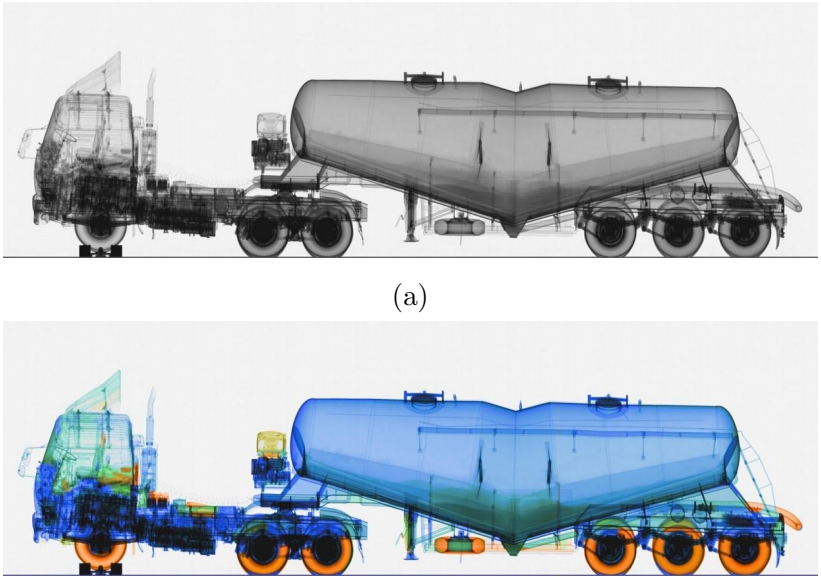

(a)

(b)

Figure 1.1: (a) single energy (b) dual energy x-ray image of the same truck

This dissertation is part of a bi-national German-Israeli research project with the goal of developing an entirely new air-cargo interrogation system capable of automatically detecting commercial and home-made explosives as well as special nuclear material (SNM). The project, called "Automated Contraband-in-Cargo Interrogation System" (ACCIS), is funded by the German Ministry of Education and Research (BMBF) as well as the Israeli Ministry of Science and Technology (MOST) in the context of the "Research for Civil Security" program [9].
The collaboration contains 10 groups: The seven German collaborators are the governmental institutions Bundesanstalt für Materialforschung und -prüfung (BAM) and the Physikalisch- Technische Bundesanstalt (PTB), the industrial partners RI Research Instruments GmbH (RI) and Roentdek Handels GmbH, as a representative for the German end-users the European Aviation Security Center Schönhagen e.V. and concerning the socio-scientific accompanying research the Human Factors Consult GmbH and the faculty of law at the Technical University of Berlin. The Israeli participants are the Weizmann Institute of Science as well as the Soreq Nuclear Research Center attend the scientific part of the project whereas the Israeli Police Bomb Disposal Division completes the group of end users.

The ACCIS project is split into two main research topics: Part one focuses on the development of the detection system and methods as well as the data analysis and

implementation of algorithms for hazardous material identification. Part two, wherein this thesis is embedded, is dedicated to developing a suitable radiation source for this particular application.
The present dissertation covers all main aspects of the second part of the ACCIS project:

The specific application of nuclear reaction-based cargo interrogation employing a pulsed, intense neutron and gamma-beam is described in detail in the second chapter. Knowledge of employed detection techniques and detector systems is essential to determine the optimal radiation source. This elaboration is pointing towards an accelerator based approach employing a deuteron beam to produce the required neutron and gamma-radiation at a production target. Concluding this chapter it is asserted that no accelerator exists on the market which entirely covers all requirements.
Evidently, a radio-frequency-quadrupole (RFQ) accelerator comes closest to what is needed, but raises questions concerning the required pulse structure. In the third chapter, an introduction to this type of ion accelerator is given and a dedicated RFQ accelerator able to accelerate an intense deuteron beam to $6\,MeV$ is designed. Since the manufacturing of an RFQ accelerator could not be covered by this thesis, an existing RFQ accelerator facility that was employed for later experiments is introduced at the end of this chapter.
As explained above, an RFQ accelerator is not capable of providing the required pulse structure, i.e. $1\,ns$ long pulses at a repetition rate of $3\,MHz$. To cope with this issue of a ns-long, high-current bunch at a high repetition-rate, a low-energy beam pulsing system had to be developed: it is presented in chapter 4. This system acts as a combined kicker and buncher system to be located between low-energy beam transport and RFQ accelerator. This is to enable single-bunch injection to the RFQ at the required repetition rate.
This pulsing system was manufactured and tested on a dedicated test bench consisting of ion source, low-energy beam transport as well as multiple diagnostic elements. The setup and optimization of the test bench, as well as commissioning and proof-of-principle experiments of the pulsing system, are described in chapter 5.
Since the radiation required by the application is not produced by the accelerator itself but at a production target located downstream, a high-current boron target was also under evaluation. The design of different target setups, as well as neutron and gamma-beam characterization experiments employing the latter, form chapter 6.
In chapter seven, the outcome of this thesis is summarized and a brief outlook is given.

2 The ACCIS Project

The ACCIS system is a combined system for detection of improvised as well as standard explosive devices and special nuclear material. The detection techniques are based on nuclear methods: for explosives detection the probing particles are neutrons employing Fast Neutron Resonance Radiography (FNRR). The nuclear material can be detected employing gamma radiation at two different energies utilizing the Dual Discrete Energy Gamma Radiography (DDEGR). Both methods combine imaging techniques with spectrographic methods. Thus, an operator will not only be able to make decisions based on shapes of objects, but also receive information on the elemental distribution of the inspected object. Details to both techniques are presented in section 2.1. A schematic view of a possible future demonstrator setup can be found in figure 2.1. As this drawing indicates, the system can be split into two principal

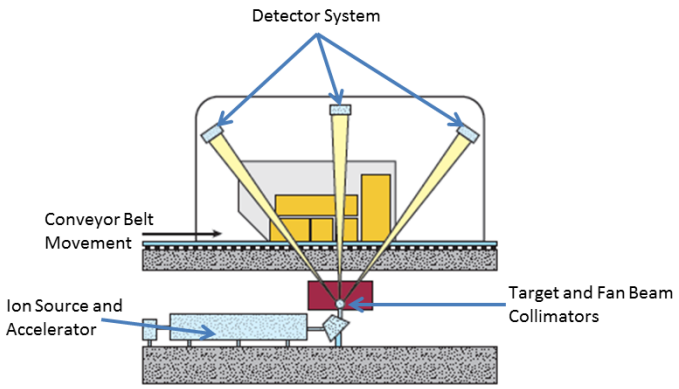

Figure 2.1: Schematic view of a possible demonstrator setup

components: the detector system and the radiation source. A short overview of the detector system will be given in section 2.2. The last section of this chapter leads over to the central topic of this work: the detector system as well as the size of the objects to be inspected define the requirements of the particle source. Since, among others, the neutron and gamma fluences determine the inspection time, an appropriate accelerator system for this purpose needs to be developed.

2.1 Overview of employed Techniques

The transmission of radiation through matter is highly dependent on the characteristics of the projectile (particle type and energy) as well as the target material (isotopic composition). Due to an interaction of the projectile with the matter (either an electron in the shell or the nucleus of the atom), the projectile might lose or gain energy or might even be deflected or absorbed. Thus, the energy spectrum of particles in a wide energy range is measured after the transmission though matter, exhibits a specific signature of the employed material. As an example, figure 2.2 shows the calculated transmission spectrum of neutrons in the energy regime of 2 to 12 MeV traversing 10 cm of polyethylene, melamine and Tri-Acetone Tri-Peroxide (TATP, an improvised explosive). The different curves reflect the different elemental compositions of the

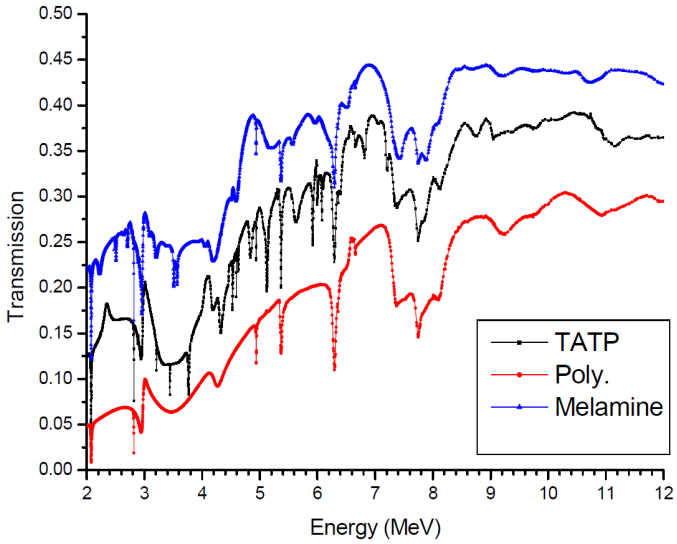

Figure 2.2: Calculated neutron transmission through different materials [10]

employed materials. Comparable spectra with different signatures can be achieved by employing gamma rays instead of neutrons, since the underlying interaction mechanisms are different. The probability for the occurrence of a specific interaction in a collision between projectile and material is described by the cross-section (see e.g. figure 2.4). In this context, the probability of each possible interaction (e.g. elastic or inelastic scattering of neutrons at the nucleus) is parametrized as a cross-section. The probability that any interaction occurs during the transmission of a particle though matter is represented in the total cross-section which is the sum of all individual interaction cross-sections.

In the ACCIS project, Fast Neutron Resonance Radiography (FNRR) and Dual Discrete Energy Gamma Radiography (DDEGR) are employed to determine the trans-

mission spectra of neutrons as well as gamma rays and compare them with known cross-section data in order to gain information about the elemental composition of the radiographed object. Furthermore, employing a pixelated detector permits producing images of the inspected items.

2.1.1 Time-Of-Flight Measurements

To enable simultaneous measurements at different incident particle energy ranges and even different particle types, the so called time-of-flight technique (TOF) is employed. For TOF measurements in the ACCIS project, a pulsed neutron/gamma ray beam with a broad energy neutron spectrum is employed. Such broad-energy neutron fields are provided by bombarding a thick target made of boron or beryllium with an approximately 5 - 12 MeV deuteron beam utilizing nuclear reactions such as e.g. $^9Be(d,n)^10B$. Since neutrons are massive particles (m_N stands for the neutron mass), the travel time (the so called time-of-flight t_{TOF}) from particle source to detector is dependent on the neutrons kinetic energy E_{kin}. A non-relativistic approximation is employed, because at energies of several MeV the neutron velocity is only a few percent of the speed of light.

$$E_{kin} = \frac{m_N \cdot d^2}{2 \cdot t_{TOF}^2} \tag{2.1}$$

The energy resolution as well as the lower energy detection limit of the measurement are mainly determined by the flightpath d. Further relevant parameters with influence to the energy resolution are time resolution of the detector as well as the pulse-width of the deuteron burst. The latter is a relevant specification for the radiation source. It should be not larger than a few nanoseconds.
Since photons have no mass, all travel at the speed of light independent of their energy. Therefore, photons are always the first particles to arrive at the detector followed by the neutrons. To measure a time-of-flight spectrum, the detector has to be synchronized to the pulsing of the neutron producing beam. Furthermore, for each detected event, the time relative to the last neutron production has to be measured. Figure 2.3 shows a typical TOF spectrum. At $30ns$, the gamma peak can be found, whereas the neutrons are following after $300ns$. The effect that the neutron counts at the end of the spectrum are not yet zero is due to so-called frame overlap: the missing neutron tail can be found at the beginning of the spectrum, overlaid with the gamma peak. This indicates, that the flight path at the measurement was too long so the lowest energy neutrons arrived at the detector even after the next gamma flash. The width of the gamma peak is a measure for the time-resolution of the measurement.

The resolution is influenced by the instrumental time-resolution of the detector as well as by the duration of the deuteron beam burst at the production target.
To determine the neutron energy, its net travel-time has to be measured at a given flight path length.

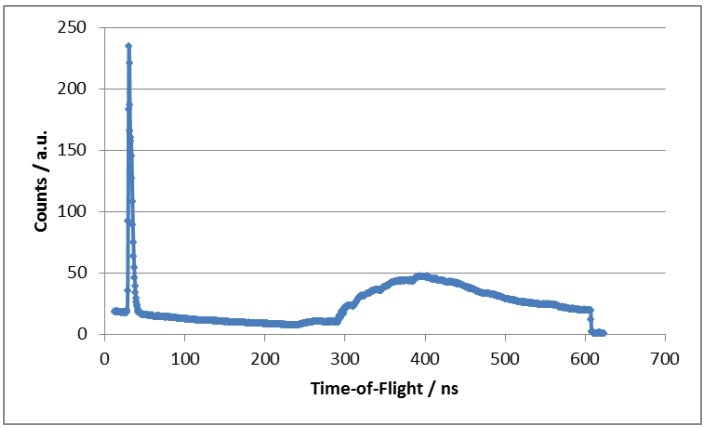

Figure 2.3: Typical neutron and gamma time-of-flight spectrum. The effect of frame-overlap is clearly visible.

2.1.2 Fast Neutron Resonance Radiography

The Fast Neutron Resonance Radiography (FNRR) is employed in the ACCIS System to enable explosives detection. Since most of the conventional as well as home made explosives are organic materials, it is sufficient to probe for the elementary composition of hydrogen, carbon, nitrogen as well as oxygen. As indicated in the introduction to this chapter, the probability of a neutron at a specific energy interacting with an atom of one of these four elements is dependent on the element. Figure 2.4 shows the different cross-sections for the mentioned elements. Each cross-section (except hydrogen) exhibits very special features, so called resonances, which can be utilized for identification of material composition. Carbon, for example, has a strong resonance in the neutron energy region between 7.5 and 8.5 MeV. If an energy spectrum of a neutron beam with and without a block of carbon placed between source and detector is measured, a significant decrease of neutron counts (proportional to the cross-section) is measured in this energy region. The contrary effect will be the case investigating e.g. oxygen in the neutron energy region from 2.5 to 3 MeV. Here, the lower cross-section will lead to a higher count rate, compared to the other elements.
Since not only bulk objects, but air cargo is to be investigated, a pixelated detector can be employed to measure not only position information but, in addition, neutron

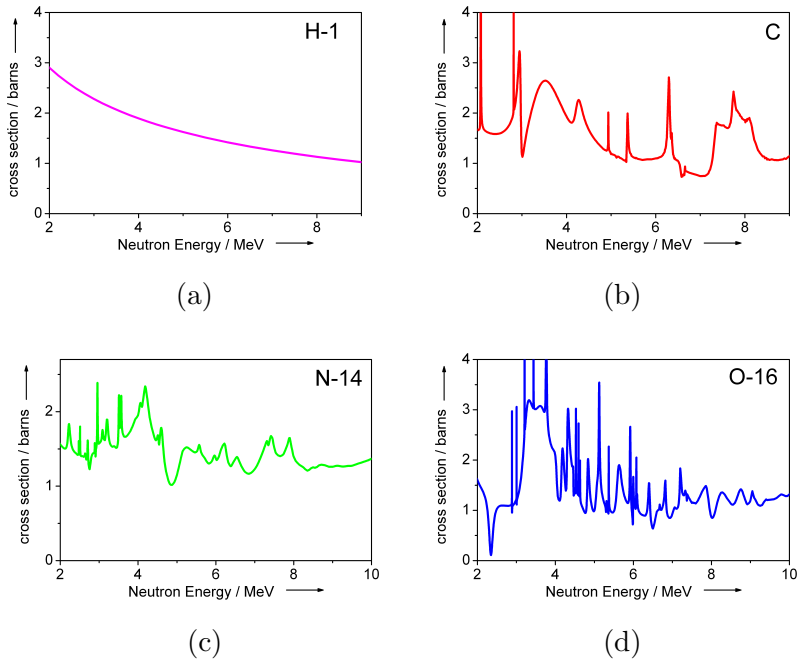

Figure 2.4: Total neutron cross-sections of (a) hydrogen, (b) carbon, (c) nitrogen (d) oxygen [11]

energy or rather neutron transit times for each pixel. Hereby, multiple images for different energy regions can be acquired and analyzed via time-of-flight [10]. By taking into account the cross-sections, the C/N/O ratios for each pixel can be reconstructed (see [12]). If the elemental compositions of suspicious materials is known, areas of the images which might contain e.g. explosives or drugs can be marked.

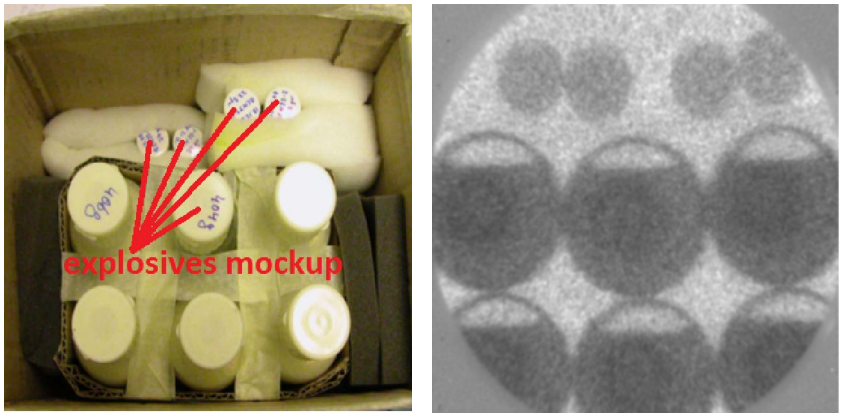

(a) picture of sample (b) gamma image

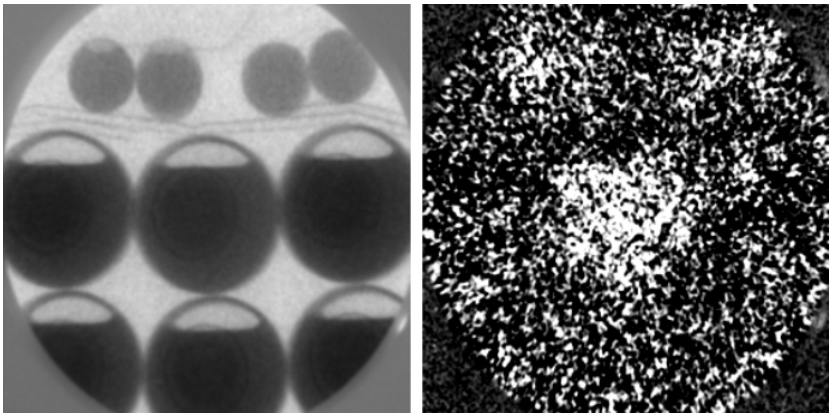

(c) total neutron image (d) reconstructed neutron image

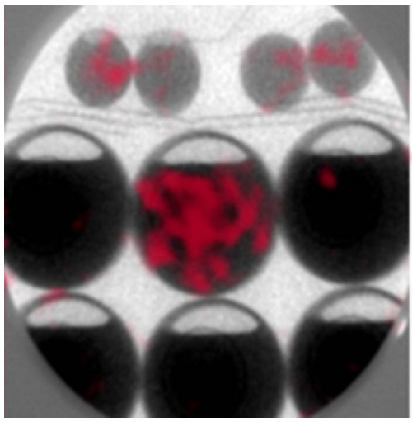

(e) total neutron image with suspicious areas

Figure 2.5: FNRR of milk bottles, some of them filled with an explosives mockup (employing TRIOR detector)[13]

Figure 2.5 shows an example of an FNRR measurement [13]. In a sample, several bottles (some filled with milk, others filled with an explosives mockup) were radiographed. In the gamma image (which is comparable to a regular x-ray image) there

is no possibility of differentiating the bottles. Also by analysis of the total neutron image, which is a summation of all neutron energies, no discrimination can be done. Via a reconstruction algorithm, the suspicious areas can be determined employing multiple radiographies taken at multiple energy intervals. When this image is overlaid on the total neutron/gamma image, the suspicious bottles can be found.

2.1.3 Dual Discrete Energy Gamma Radiography

The Dual Discrete Energy Gamma Radiography (DDEGR) is employed to detect special nuclear material (SNM). The term SNM is defined to be plutonium or uranium (appreciably enriched in U-235) but may include other radioactive elements in the future [14]. The technique was proposed and patented by some of the collaborators in the ACCIS project [15]. While high-energy X-ray scanners (based on MeV Bremsstrahlung techniques) probe the electron density of the inspected object, the discrimination between SNM and regular high-Z materials like tungsten is not possible. Employing DDEGR, an object under investigation is irradiated in parallel with gamma rays of two discrete gamma lines of different energies. In contrast to dual energy x-ray machines, where two Bremsstrahlung spectra are employed, in DDEGR the two separated discrete gamma lines increase the contrast sensitivity.
The transmission of gamma particles is dependent on the mass attenuation coefficient. This coefficient is taking into account all interactions of gamma particles with different matter (photo electric effect, compton-effect and pair-production). In the energy regime at gamma energies above $1\,MeV$ (regime where pair production starts to play a role), the mass attenuation coefficient strongly deviates not only depending on the material, but second also on the gamma energy as figure 2.6 indicates. Thus, employing two different energy gamma particles increases the discrimination sensitivity by analyzing the ratio of the attenuation at both energies.

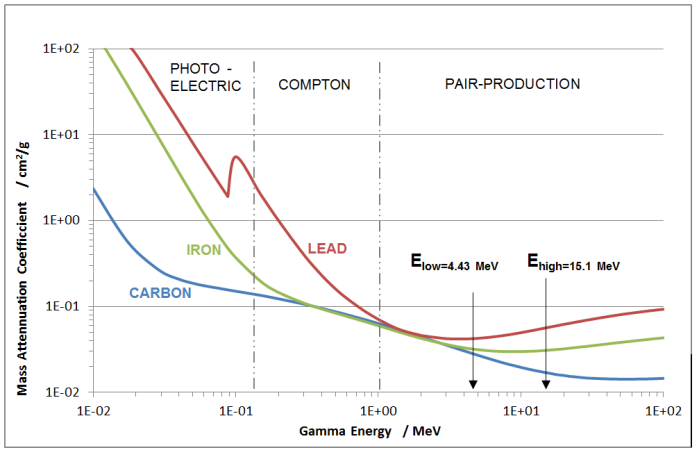

Figure 2.6: Mass attenuation coefficient of different materials

In the ACCIS project, two discrete gamma lines of the energy 4.43 and 15.1 MeV are employed utilizing the $^{11}B(d, n+\gamma)^{12}C$ reaction. In figure 2.7 the results of a demo experiment are presented. The sample setup was radiographed in the front view. For the analysis of the radiography, in addition to the mass attenuation coefficient, the sample thickness (could be calculated by employing few-view tomography in the final system) was taken into account to calculate the macroscopic attenuation coefficient. Employing a discrimination threshold on the analyzed data marks the suspicious regions in the radiograph.

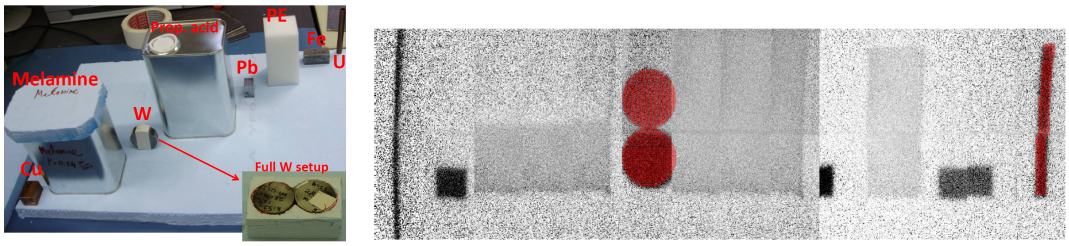

(a) (b)

Figure 2.7: DDEGR example - (a) picture of setup (b) analyzed radiography with suspicious materials marked in red [16]

2.2 Detector Concepts

A key element of a successful interrogation system is a working detector system which is on the one hand sensitive but on the other hand fast enough to deliver the important information on the inspected goods. In the 1990's an earlier approach to take into operation a comparable demonstrator system was performed by Tensor Technology, Inc

[17]. Although this approach seemed to be promising for bulk explosives detection, it failed due to the poor spatial resolution of the prototype detector system (see [18]). The detector resolution ($2.5\,cm$) was too low to effectively detect thin sheet explosives. Thus, for the detector of the ACCIS system spatial resolution of a few millimeters.

Two different approaches for an ACCIS detector system were investigated: The first system, denoted Time Resolved Integrating Optical Radiation (TRIOR) detector, is based on integrating accumulation of neutron images for different gamma- or neutron-energy windows. The second, denoted Time Resolved Event Counting Optical Radiation (TRECOR) detector is based on single neutron- or gamma-event counting and is able to simultaneously acquire position as well as particle energy and type. Both detector systems employ a neutron scintillator screen, which produces scintillation light from impinging neutrons and gammas; it is subsequently deflected out of the particle beam by a mirror oriented at 45° to the beam axis. A set of optical lenses and an image intensifier are then employed to focus the image onto a readout system. In the following sections, the special features of the two detector types and the differences between them are highlighted.

2.2.1 Time Resolved Integrating Optical Radiation detector

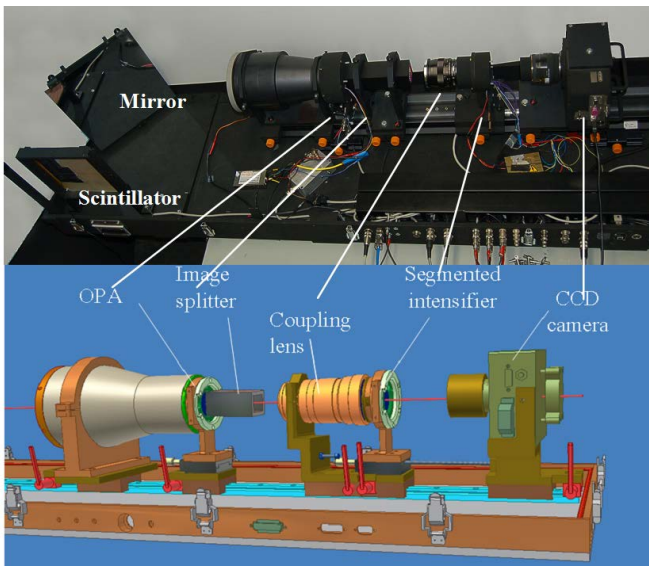

Figure 2.8: Schematic view of the TRIOR detector

The general setup of the TRIOR detector is shown in figure 2.8. Behind the mirror, the scintillation light is captured in a large-aperture lens and the image is de-magnified from $20 \times 20\,cm^2$ (size of scintillator) to the size of an inscribed square within a

circle of diameter 40 mm. Directly at the end of the large aperture lens, a special image-intensifier is mounted, which has a special phosphor screen with a very short decay time of only a few nanoseconds. This so-called optical preamplifier (OPA) is followed by the two key components of this detector system: An image splitter based on total reflection in a quartz crystal, which produces nine identical images, as well as a segmented image intensifier, which is equipped with eight independently nanosecond-gateable photo-cathode pads (see figure 2.9). The image-intensifier can be employed to select up to eight different energy windows by choosing specific gate windows on the neutron time-of-flight spectrum. Readout is performed by a CCD camera which is capable of integrating the final image over many deuteron pulses/beam bursts. For further details see [19]. Results obtained with this type of detector can be found in figure 2.5.

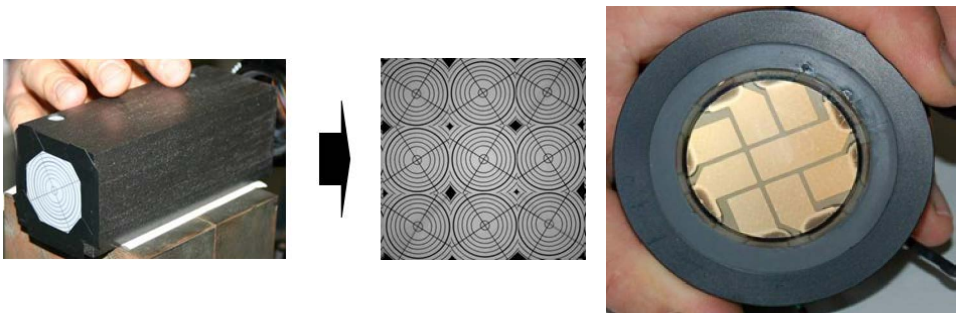

(a) (b)

Figure 2.9: (a) Image splitter (b) Segmented photo-cathode

2.2.2 Time Resolved Event Counting Optical Radiation detector

The initial stages of the TRECOR detector system (see figure 2.10) are comparable to the TRIOR setup up to the large aperture lens. In addition to the position-sensitive optical detector, a photomultiplier is coupled to the scintillator, in order to measure pulse-height information on detected gamma events. In TRECOR, the large aperture lens is followed by a special pulse-counting image intensifier [20]: In it, the phosphor screen is replaced by a resistive anode on a thin ceramic vacuum window, which permits a position-sensitive readout electrode to be placed outside the vacuum tube. This read out electrode consists of a special triple-layer printed circuit board (PCB), equipped with a two-dimensional pad structure. The two ends of each dimension are coupled to a meander-type delay line (see figure 2.11). If an electron avalanche from the micro-channel-plate (MCP) of the image intensifier hits the high-resistive anode, an electronic impulse is induced to the structure of the PCB. Due to the delay-lines, the position

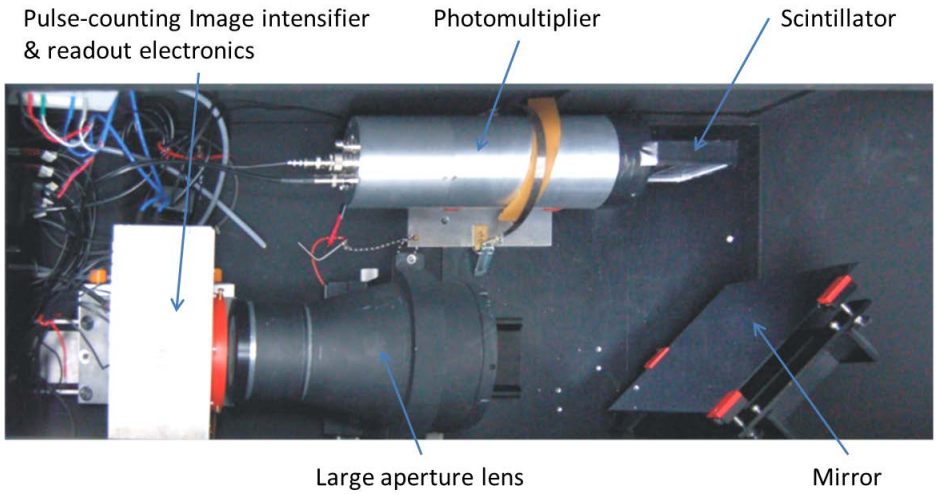

Figure 2.10: Picture of the TRECOR detector

coordinates of the avalanche event can be determined by measuring four time delays. The third layer/dimension is used to measure redundant position information. In further data analysis, this can be used to improve the position resolution or reconstruct measurements in which one of the first four time delays is corrupted. The special feature of this detector is its capability to accumulate single neutron or gamma events. Together with the time signals necessary for position determination, a time-of-flight signal is measured for each event. To differentiate between different gamma energies, the coincidently measured signal of the photomultiplier is correlated to each pixel event.

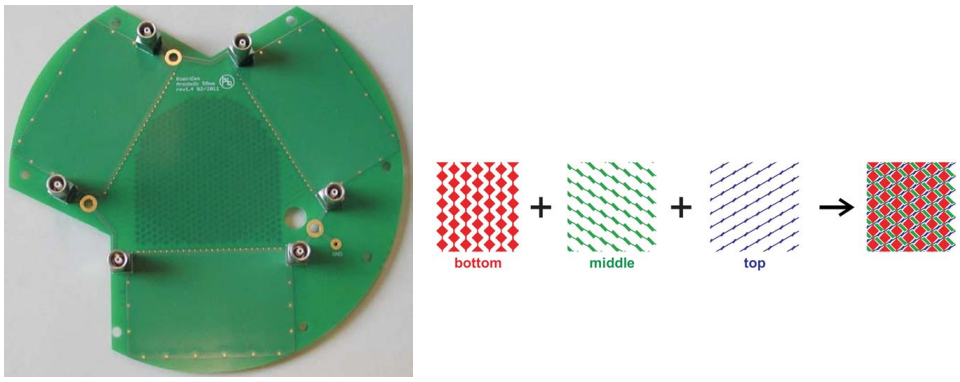

(a) (b)

Figure 2.11: (a) Electronic readout of the TRECOR detector (b) Scheme of the readout pattern [20]

Figure 2.13 shows an imaging result of the TRECOR detector: A wooden rack which contains different liquids and solids was radiographed and the accumulated de-

tected particles are displayed. Furthermore, each pixel of the image contains an entire neutron time-of-flight spectrum. By selecting specific energy intervals (e.g. at a high oxygen cross-section), regions of high oxygen content will have an decreased number of counts (in other words decreased brightness in the picture as it is a transmission image). Employing advanced analysis techniques on the entire four-dimensional (or five dimensional, including pulse-height spectra) result array of experimental results by comparing the spectral information with relevant cross-section data, the material content in a region-of-interest can be determined.

(a) (b)

Figure 2.12: (a) Photograph of test objects and (b) Radiograph (combined neutron and gamma image)

2.3 Specification of the Radiation Source

To define the parameters for a suitable radiation source for an ACCIS system, several aspects have to be taken into account: First of all, a particle source is required which is capable of producing simultaneously a broad-energy neutron spectrum at energies between $1-10MeV$ as well as gamma-rays in two well-separated energy regimes. The nuclear reaction $^{11}B(d,n+\gamma)^{13}C$ is proven to be capable of fulfilling these specifications. The neutron spectrum of this reaction employing deuterons of various energies can be found in figure 2.13a. This reaction also produces gamma-rays or events at two different discrete energies, namely $4.43\,MeV$ as well as $15.11\,MeV$. The gamma yield at different deuteron energies can be found in figure 2.13b. Other target reactions with comparable neutron production yield do not feature the dual discrete energy gamma production required for the application. Thus, a deuteron accelerator employing an enriched ^{11}B target appears to be the preferred radiation source.

To further define the source parameters, the dependence of the radiographic con-

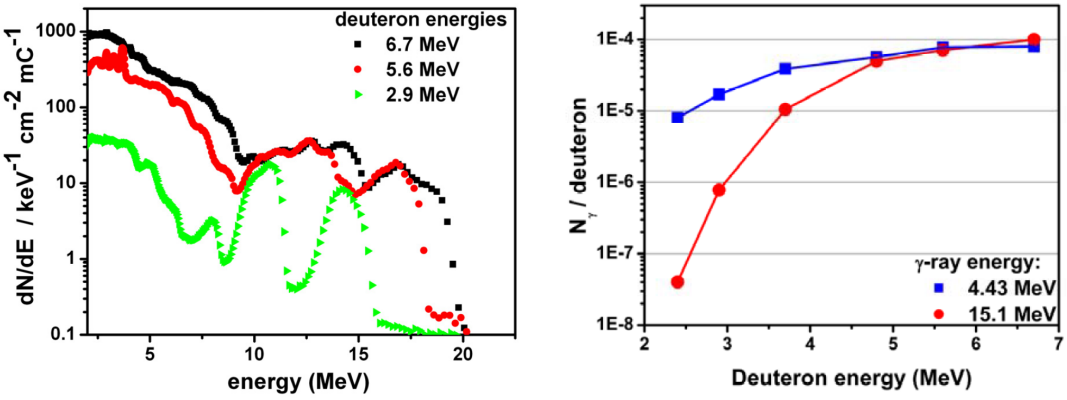

(a) (b)

Figure 2.13: (a) Neutron yield and (b) gamma yield of the $^{11}B(d, n + \gamma)^{13}C$ reaction [21]

straints on the source characteristics can be investigated. The quality of the radiographic images is, apart from the detector specifications, mainly dependent on the source geometry. The radiation source has to be a point-like source with lateral dimensions not exceeding $1\,mm$, to obtain reasonable spatial resolution in the images. The object will be located in the middle between source and detector, the source spot dimension limits the achievable spatial resolution in the detector plane. The aim of the project is to be able to detect this sheet explosives.

Furthermore, the source has to be pulsed, to permit utilizing time-of-flight methods such as FNRR and DDEGR. Since neutron energy as well as neutron-gamma discrimination is employed by measuring time-of-flight, the energy resolution is dictated by the duration of the neutron- and gamma-producing deuteron pulse. Therefore, the pulse duration should be of about $1\,ns$, but no longer than $2\,ns$. Employing formula 2.1 it can be calculated that a pulse duration of $2\,ns$ leads to an uncertainty in measured neutron energy of up to $168\,keV$ (for $7\,Mev$ neutrons), not taking into account uncertainties of the detector or during data analysis. So the measured spectrum will be blurred and resonances in the neutron cross-sections smaller than this value cannot be utilized.

A major functional requirement of the system its compactness. The distance between target and detector should not exceed $6\,m$. On the other hand, the lower neutron energy limit for FNRR is a detectable energy of $2\,MeV$. The time-of-flight for $2\,MeV$ neutrons at a distance of $6\,m$ is $306\,ns$. To be able to measure this energy without the occurrence of frame overlap, a beam-burst repetition rate of about $\leq 3\,MHz$ should

be employed, which corresponds to an RF cycle of $333\,ns$.
Another aspect that influences source specifications is the throughput of a future demonstrator machine: The neutron and gamma fluence and hence the deuteron energy and current determines the interrogation time of inspected objects. Calculations have determined (see [22]) that a deuteron beam with a time-averaged current of $600\,\mu A$ at $5-7\,MeV$ is sufficient for the interrogation of an LD3-type [23] container in less than 5 minutes. All these specifications lead to a deuteron pulse beam-charge of around $200\,pC$ per deuteron pulse.
An overview of all specifications can be found in table 2.1.

Ion Species	Deuterons
Energy	$5-7\,MeV$
Repetition Rate	$< 3\,MHz$
Pulse Length	$< 1\,ns$
Average Current	$600\,\mu A$
Pulse Charge	$200\,pC$
Peak Current	$200\,mA$

Table 2.1: Overview of the ACCIS source specifications

2.4 Selection of the Accelerator Type

The crucial points of the source specifications are the pulsing regime in combination with the desired beam current. Electrostatic beam accelerators such as Single-Stage or Tandem Van-De-Graaff accelerators are frequently employed to produce deuteron beams, but these are typically limited to several mA beam current or even less [24]. Classic RF-driven accelerators such as cyclotrons are also limited in maximum current to several mA [25] [26]. If the pulsing scheme would be realized merely by chopping the DC beam, an overall beam current of around $200\,mA$ would be required. This corresponds to rejecting 99.7 % of the beam, which is not a feasible option at these high initial beam currents and beam energies. Thus, an efficient longitudinal beam compression (beam-bunching) before or during the acceleration process is key in ensuring the viability of the inspection system.
A Radio-Frequency-Quadrupole (RFQ) accelerator, originally developed in 1970 in Russia by I.M. Kapchinskii and V.A. Teplyakov [27] is an RF-driven, linear accelerator that enables efficient acceleration of high-current ion beams from several 10 keV to

energies close to 10 MeV. It combines acceleration with continuous transversal focusing as well as longitudinal bunching. Unfortunately, the typical operation frequency of RFQ's are $80 - 500\,MHz$, so the required pulsing regime cannot only be achieved solely with the intrinsic RFQ bunching. To overcome this issue, an additional prepulsing system was designed (see chapter 4). Apart from the pulsing issue, all other requirements could be fulfilled in previous RFQ accelerator systems (see e.g. [28]), so an RFQ accelerator appears to be a suitable accelerator type for the ACCIS particle source.

3 Radio-Frequency-Quadrupole (RFQ-) Accelerator

In this chapter, the basic ideas as well as the physics of RFQ accelerators will be explained. Furthermore, the design study of a dedicated ACCIS RFQ will be presented. In the final section, the DWIK-RFQ of NECSA in Pelindaba, South Africa, which is considered to be a candidate for a demonstrator system for an ACCIS system, will be presented.

3.1 The Basic RFQ-Accelerator Concepts

Like the name indicates, an RFQ is an acceleration structure which is based on strong focusing: In 1952, E. D. Courant, M. S. Livingston and H. S. Snyder from Brookhaven National Laboratory in New York realized, that a quadrupole field with alternating gradient leads to a net focusing effect[29]. Although a quadrupole field focuses the beam only in one axis while the other is defocused, the defocused beam component is later on stronger focused due to the high field gradient in the transversal directions (see figure 3.1).

This principle was adapted to accelerate low-energy, high-current ion beams: Four

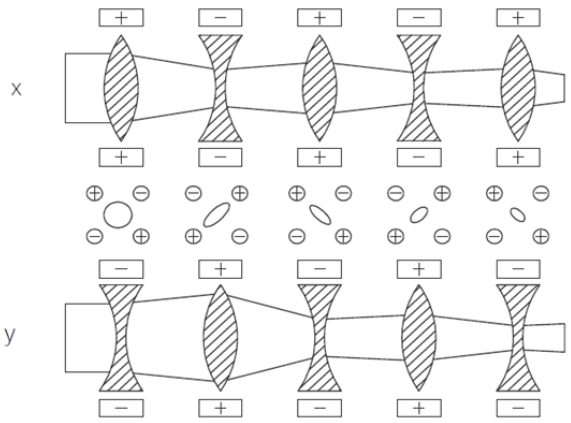

Figure 3.1: Principle of strong focusing [30]

so called rods are are arranged perpendicular to each other in a 90° symmetry like the poles in a magnetic or electrostatic quadrupole. To obtain alternating quadrupole fields, a radio-frequency is applied. Employing just smooth rods, the device would lead only to a focused beam. An acceleration can be achieved, if, in addition, the rods are shaped with a geometrically modulated profile, where the modulation phase of the perpendicular rods is shifted by 180°, such that a valley in one plane has a maximum in the perpendicular plane These features are indicated in figure 3.2. Figure 3.3 (a)

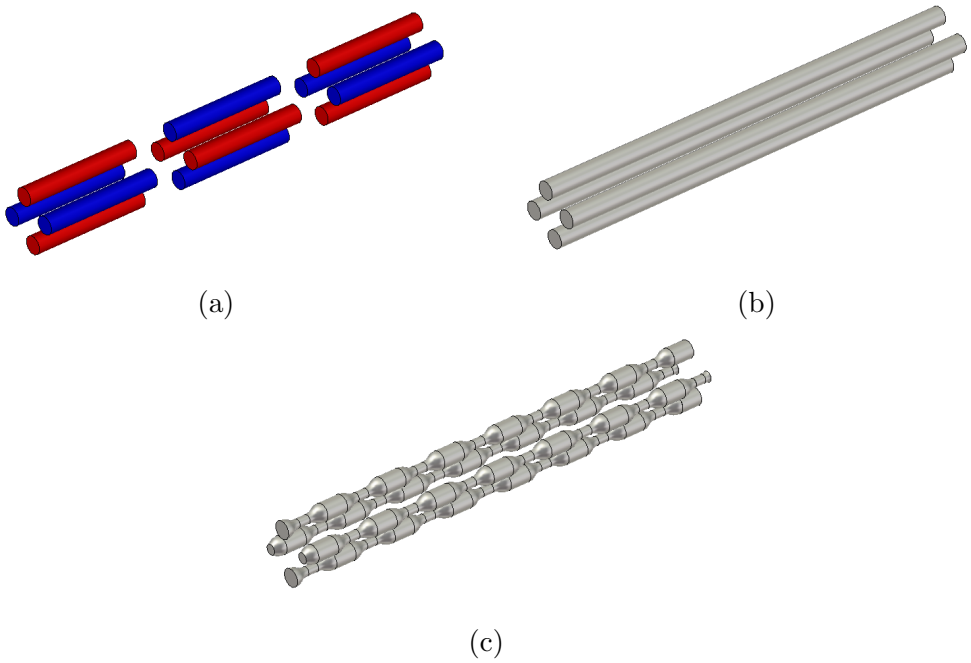

Figure 3.2: Evolution of the RFQ: (a) electrostatic quadrupoles, (b) RF-based quadrupole, (c) rod-type RFQ allowing for acceleration

shows a schematic view of the modulation geometry of a so called unit cell. The length of the unit cell is defined by the particle velocity as well as the resonance frequency. The modulation itself can be described employing the aperture a (minimal distance of the unit cell to the beam axis) as well as the modulation parameter m which is a factor (usually taking values between 1 and 2.3) to describe the maximum distance ($m * a$) from the beam axis (compare figure 3.3a). V stands for the inter-vane voltage, whereas two adjacent vanes are always oppositely charged. The length of the unit cell of such a structure is dependent on the desired particle energy, as it is defined to be $\frac{\beta \cdot \lambda}{2}$, where β is the velocity in units of the speed of light and λ the wavelength of the operation frequency. Thus, $\beta \cdot \lambda$ is the distance traveled during an RF period. Figure 3.3 (b) shows the simulation result of the electric field of a unit cell, which indicates a resulting field component in the longitudinal direction. Since the electric field in

the RFQ is not static but oscillating, only half of a continuous beam would see an accelerating field component, the other half would even be decelerated. To prevent this, the continuous beam has to be bunched before it can be accelerated.

In the past, an RFQ layout introduced by the Los Alamos accelerator group became

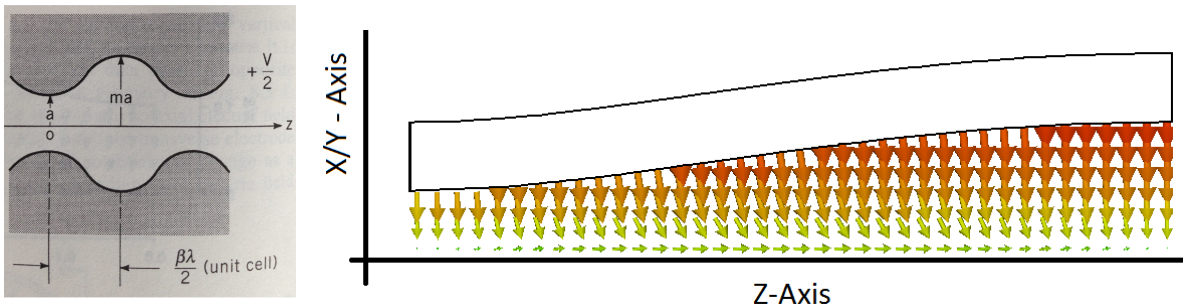

(a) (b)

Figure 3.3: (a) Schematic view of the RFQ modulation [31] and (b) electric field of an RFQ unit cell

widely accepted: As figure 3.4 shows, an RFQ consists of four functionally different sections: in the radial matching section (RM), the ion beam from the low-energy beam transport (LEBT) section or ion source is captured and transversally guided into the RFQ. In the shaper section, the beam is further focused such that a parallel beam is formed. To introduce a bunching, in the shaping section the modulation parameter m is slightly raised starting at 1, so some parts of the beam become just slightly accelerated and the rest slightly decelerated. In other words, the bunching process is gradually setting in. The main focus concerning the bunching strategy is particle loss due to space-charge of the low energy ions. Due to sequentially increasing bunching forces, the particle loss can be reduced to almost 0.

A special feature of the RFQ is the so called adiabatic bunching, which starts in the gentle buncher (GB) section. Prior to the GB, the net energy increase and the corresponding velocity increase are negligible. Within the GB section, the maximum spatial bunching is achieved. But, due to the acceleration of the bunch, there is further bunching: so called adiabatic bunching in the time domain. Thus, after the GB section, the maximum modulation depth is achieved and kept constant in the acceleration section until the final energy is reached.

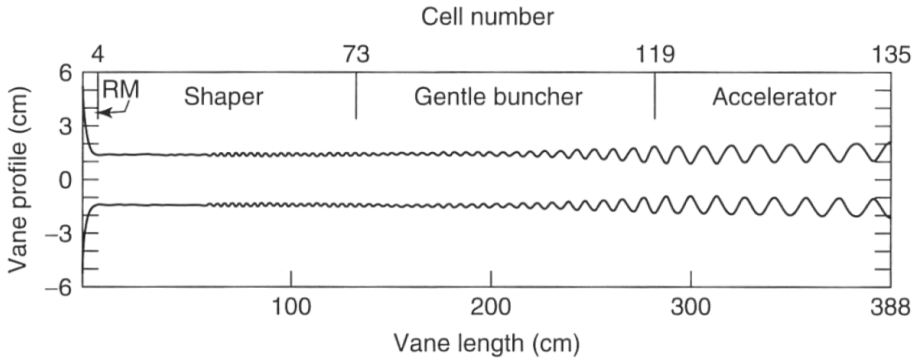

Figure 3.4: Layout of an RFQ developed by the LANL accelerator group [31]

There are two main types of RFQ accelerators: One distinguishes between rod and vane type RFQs. Figure 3.5 shows images of both types of structures. The rod type RFQ is historically the original RFQ design by Kapchinskii and Teplyakov which was developed in 1975 and published in 1977 [32], whereas the vane type design was developed at Los Alamos National Laboratory in 1980 (POP RFQ)[33].

In a rod type RFQ, four perpendicular rods carrying opposing modulations are

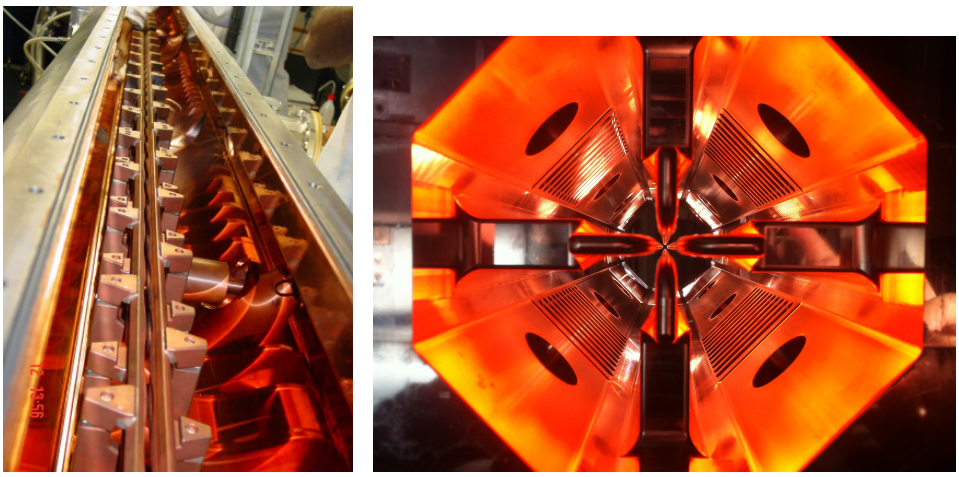

(a) (b)

Figure 3.5: Comparison between (a) 4-Rod-type RFQ (as used in the DWIK accelerator) and (b) 4-Vane-type RFQ (employed for the SNS injector)

placed in a vacuum tank. They are held in position by multiple, so called stems. Each stem holds two opposing rods at the same potential. Since, in the longitudinal direction, the rods held by the stems are alternating, the resonant system of a 4-rod RFQ is composed by the capacitance of the inter-rod gap as well as the inductance represented by a set of stems and the wall between them (see figure 3.6a). To tune

the resonance frequency, tuning plates can be added to this wall.

In a vane type RFQ, the modulation is machined into the inner section of the four vanes, which are typically directly brazed together to form the vacuum tank wall. In contrast to the rod type RFQ, the resonant system is located transverse to the beam direction: Although the inter-vane gap again acts as capacitance, the inductance of the 4-vane RFQ is composed by the tank surface and the neighboring surfaces of two vanes (see figure 3.6b). To tune the 4-vane RFQ, the inner volume of the tank has to be modified, employing so called slug-tuners, which are inserts to the RFQ walls, and whose penetration depth into the cavity can be varied (see section 3.2.2 for further details).

Since the outer tank of a 4-rod RFQ has only minor influence on the resonant fre-

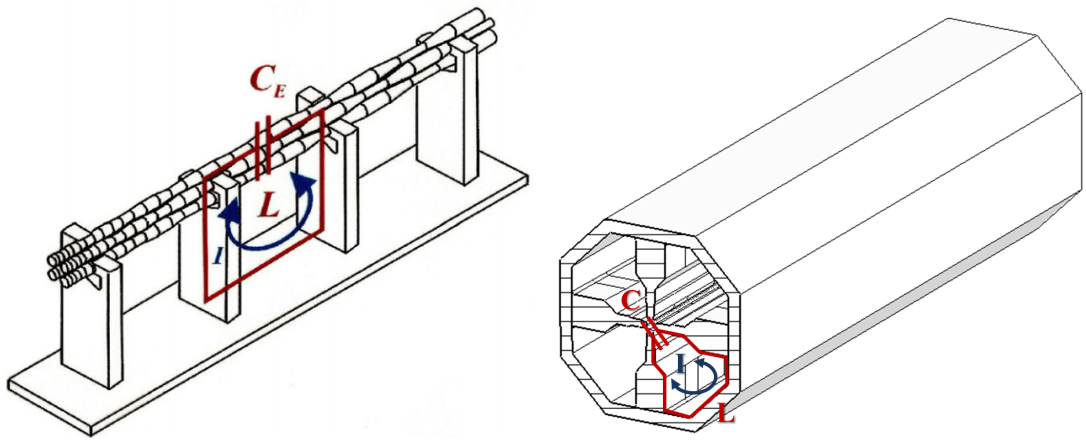

(a) (b)

Figure 3.6: Lumped circuit model of (a) 4-Rod-type[34] and (b) 4-Vane-type RFQ

quency, a low frequency, rod type RFQ can be designed much more compact than the equivalent vane type RFQ. As the lumped circuit model indicates, the operation frequency of a vane-type RFQ has direct influence on the geometrical dimensions of the entire cavity. Thus, applications which require low operation frequencies below approximately $100\,MHz$ (e.g. heavy-ion accelerators) favor the rod type design.
On the other hand, high-power and continuous operation RFQs (so called continuous-wave RFQs) favor a vane type design because of thermal issues: Typically in rod-type RFQs, the rods are only indirectly cooled through the stems, whereas in a vane-type RFQ, multiple cooling channels can be located throughout the entire cavity.

3.1.1 Electric field calculation in an RFQ

To calculate the electric field and also describe the rod or vane-tip geometry (since the vane tip is an equipotential surface in this problem), I.M. Kapchinskii and V.A. Teplyakov determined the following static potential function (see equation 3.1) as a solution of the Laplace equation in polar coordinates employing the method of separation of variables. It can be shown that the quasistatic approximation is valid as long as the distance from the vane tips to the beam axis is small with respect to the RF wavelength (compare with [31]). This is true for all regular operating frequencies, because the coulomb charge on the vane tips is the principal source of the electric field between them. In the equation 3.1, I_{2n} is the modified Bessel function and $k = \frac{2\pi}{L}$, where L is the length of a unit cell. To achieve the goal of synchronism (in other words being able to fill each modulation period with one distinct beam bunch) the length is defined to fulfill $L = \beta_s \lambda$, where β_s is the design velocity of a ideally synchronous accelerated particle.

$$V(r,\theta,z) = \sum_{s=0}^{\infty} A_s r^{2(2s+1)} \cos\left[2\left(2s+1\right)\theta\right] + \sum_{n=1}^{\infty}\sum_{s=0}^{\infty} A_{ns} I_{2s}\left(knr\right) \cos 2s\theta \sin knz \quad (3.1)$$

Since infinite series are not of practical use e.g. for a simple optimization of the vane tip geometry, an approximation can be performed which leads to the so called Two-Term potential function (equation 3.2). This function consists of one term that describes the focusing quadrupole field (s=0), and a second term that describes the acceleration (s=1 and n=0).

$$V(r,\theta,z) = A_0 r^2 \cos\left(2\theta\right) + A_{10} I_0\left(kr\right) \cos\left(kz\right) \quad (3.2)$$

The recent computer codes employed for designing RFQ accelerators, such as Parmteq [35] or RFQGen (a further development of Parmteq developed and distributed by Lloyd Young) employ a potential function that comprises eight terms, but this will not be further discussed in the framework of this thesis.
In a further step, the constants of the series approximation need to be determined. Adjacent vanes always are oppositely charged such that the potential on the vertical vane is $-\frac{V_0}{2}$ and on the horizontal $\frac{V_0}{2}$, whereas V_0 is the so called inter-vane Voltage. Moreover, two boundary conditions can be derived from the geometry. At the beginning of a unit cell ($z = 0$), the vertical vane tip ($\theta = \frac{\pi}{2}$) to beam axis distance is at its maximum ($r = ma$), whereas, at the perpendicular, horizontal vane($\theta = 0$), this distance is at its minimum ($r = a$). The modified Bessel function can be approximated employing $I_0(x \cong 1 + \frac{x^2}{4})$[36]. This leads to the following two equations for the

horizontal and vertical vane pair.

$$-\frac{V_0}{2} = -A_0 \left(ma\right)^2 + A_{10} I_0 \left(ka\right) \tag{3.3}$$

$$\frac{V_0}{2} = A_0 a^2 + A_{10} I_0 \left(kma\right) \tag{3.4}$$

This equation system can be solved to determine the constants A_0 and A_{10} as follows

$$A_0 = \frac{V_0}{2a^2} \frac{I_0(ka) + I_0(kma)}{m^2 I_0(ka) + I_0(kma)} = X \frac{V_0}{2a^2} \tag{3.5}$$

$$A_{10} = \frac{V_0}{2} \frac{m^2 - 1}{m^2 I_0(ka) + I_0(kma)} = A \frac{V_0}{2} \tag{3.6}$$

introducing the acceleration efficiency A and the focusing efficiency X

$$A = \frac{m^2 - 1}{m^2 I_0(ka) + I_0(kma)} \tag{3.7}$$

$$X = \frac{I_0(ka) + I_0(kma)}{m^2 I_0(ka) + I_0(kma)} \tag{3.8}$$

Obviously, when there is no modulation depth ($m = 1$), there is no acceleration. Furthermore, increasing the acceleration efficiency compromises on a reduced focusing efficiency. The two term potential in Cartesian coordinates con now be defined as

$$V(x, y, z) = \frac{V_0}{2} \left[\frac{X}{a^2} \left((x^2 - y^2) \right) + A I_0 \left(k \sqrt{x^2 + y^2} \right) \cos kz \right] \tag{3.9}$$

We defined the voltages at the vertical and horizontal vane-tips to be $-\frac{V_0}{2}$ and $\frac{V_0}{2}$ respectively. Furthermore, the vane tips are the reference points for mapping the equipotential surface. Taking into account that $y = 0$ for the horizontal and $x = 0$ for the vertical vane tips, the functions $x(z)$ and $y(z)$ which describe the modulation profile along the beam axis can be derived from the two-term potential as follows

$$x(z) = \pm \sqrt{\frac{1 - A \cos kz}{\frac{X}{a^2} + A \frac{k^2}{4} \cos kz}} \tag{3.10}$$

$$y(z) = \pm \sqrt{\frac{-1 - A \cos kz}{\frac{Ak^2}{4} \cos kz - \frac{X}{a^2}}} \tag{3.11}$$

It has to be taken into account that X, A and a are also functions of the longitudinal coordinate z. For further derivation of the electric field components, the time-dependent

scalar potential $U(x,y,z,t) = V(x,y,z) * \sin\omega t + \phi$, whereas $\frac{\omega}{2\pi}$ is the resonance frequency of the RFQ structure and ϕ is its phase. Employing $E = -\nabla U$ the electric field components can be calculated to be

$$E_x = \left[-\frac{XV_0}{a^2}x + \frac{kAV_0}{2} I_1(k\sqrt{x^2+y^2}) \frac{x}{\sqrt{x^2+y^2}} \cos kz \right] \sin\omega t + \phi \tag{3.12}$$

$$E_y = \left[\frac{XV_0}{a^2}y - \frac{kAV_0}{2} I_1(k\sqrt{x^2+y^2} \frac{y}{\sqrt{x^2+y^2}} \cos kz \right] \sin\omega t + \phi \tag{3.13}$$

$$E_z = \left[\frac{kAV_0}{2} I_0(k\sqrt{x^2+y^2}) \sin kz \right] \sin\omega t + \phi \tag{3.14}$$

The first term of the transversal field components can be identified with a regular quadrupole field. Moreover, the longitudinal component only depends, as expected, on the acceleration efficiency. The longitudinal electric field can be employed to determine the energy gain of a particle with velocity β' in a unit cell, integrating it over the entire length. The time-dependence in the longitudinal component of the electric field can be converted to distance traveled by a particle along the beam axis via $\omega t = \frac{2\pi z}{\beta' \lambda}$. Thus, the energy gain can be determined by

$$\Delta W = \frac{qkAV_0 I_0(k\sqrt{x^2+y^2})}{2} \int_0^l \sin kz \sin(k'z + \phi)\, \mathrm{d}z \tag{3.15}$$

To obtain a simple solution of the integral, only the synchronous case of $\beta' = \beta_s$ is analyzed. Here, $k' = k = \frac{2\pi}{\beta_s \lambda}$ and $l = \frac{\beta_s \lambda}{2}$. Substituting the solution of the definite integral

$$\int_0^l \sin kz \sin(kz + \phi)\, \mathrm{d}z = \frac{-\sin(2kl + \phi) + 2kl\cos\phi + \sin\phi}{4k} \tag{3.16}$$

the energy gain of a unit cell can be written as

$$\Delta W = \frac{q\pi AV_0 I_0(k\sqrt{x^2+y^2})\cos\phi}{4} \tag{3.17}$$

Thus, the maximum acceleration can be reached if the phase shift to the synchronous phase is 0°. Moreover, the particles will be decelerated, if the phase is between $\frac{\pi}{2}$ and $\frac{3\pi}{2}$. The acceleration can be increased only by increasing the voltage or increasing the modulation depth m.

3.1.2 Characterization of a particle beam using Emittance and Twiss-Parameters

Since, for many applications, it is not necessary to mathematically describe the movement of all individual particles of a beam, a different approach was developed to describe and quantify the shape of an entire particle beam employing the beam envelope. The physical value of the emittance ϵ as well as the so called Twiss-Parameters β, α and γ (also known as Courant-Snyder-Parameters, named after the inventors of the strong focusing) were introduced. The emittance describes an area (2-dimensional, transversal or longitudinal) in 6-dimensional phase-space that is filled by particles of the beam. Thus, it can be interpreted as the product of the beam diameter and its angular spread. Typically, transversal and longitudinal planes are decoupled in the emittance analysis. The unit for transversal emittance is $length \times angle$, whereas $phase \div energy$ is its longitudinal equivalent. The general equation for an ellipse in phase space $x - x'$ [31] is thus:

$$\epsilon = \gamma x^2 + 2\alpha x x' + \beta x'^2 \tag{3.18}$$

Figure 3.7 shows a typical plot of a transversal phase space ellipse. The surface area

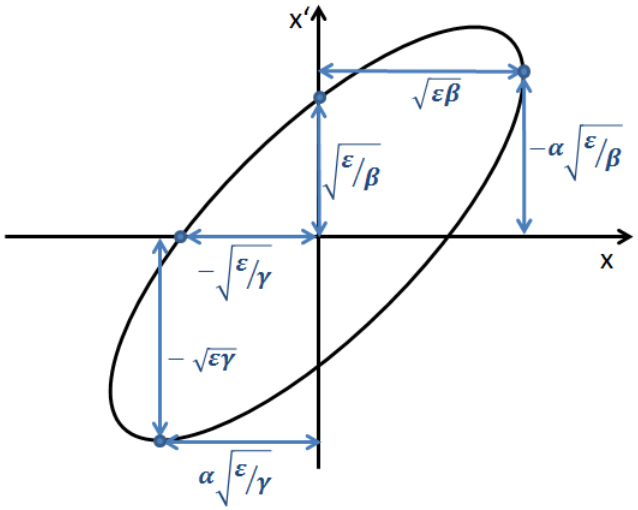

Figure 3.7: Arbitrary plot of a transversal phase space ellipse

of the ellipse corresponds to the emittance. The prominent points of the ellipse such as peaks or axis intercepts are described employing the Twiss-Parameters α, β and γ (not to be confused with the Lorentz factor γ or the relativistic velocity factor β) [37], which represent a variety of beam characteristics. The beam diameter σ can be

distinguished employing β

$$\sigma = \sqrt{\beta\epsilon} \tag{3.19}$$

whereas γ is correlated to the beam divergence σ'

$$\sigma' = \sqrt{\gamma\epsilon} \tag{3.20}$$

Here, the parameter α describes the correlation between position x and momentum x'. For a beam waist it holds that $\alpha = 0$. Since

$$\beta\gamma - \alpha^2 = 1 \tag{3.21}$$

only two Twiss parameters are necessary to describe the entire ellipse. Employing Liouville's theorem, emittance is conserved, provided external forces to the applied RF-field (e.g. space charge) can be neglected. Focusing of a particle beam decreases the diameter, but its divergence is increased. As figure 3.8 illustrates, the orientation of the phase space ellipse indicates whether the beam is focused or defocused. Since single outliers can have a huge influence on the emittance value, it is customary to quote the emittance of a bulk fraction of the beam (typically 90% of the total intensity), to characterize the particle beam.

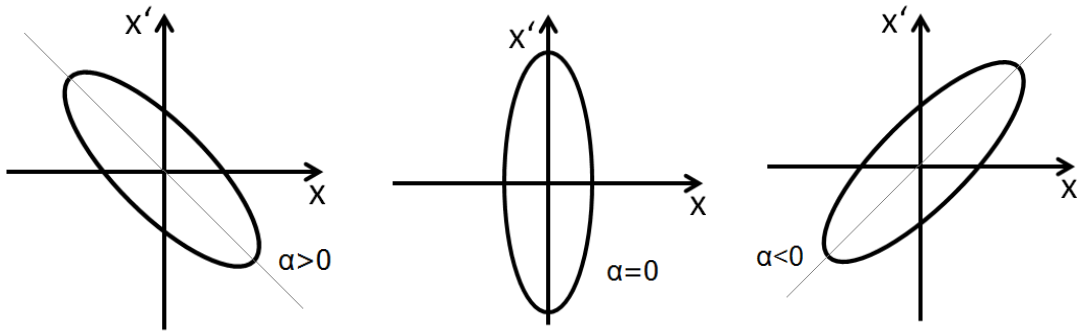

(a) (b) (c)

Figure 3.8: Phase space ellipses of a (a) convergent (b) beam waist and (c) divergent particle beam

3.2 ACCIS-RFQ Design Study

The goal of thesis was to perform a design study of a dedicated ACCIS radiation source based on a RFQ deuteron accelerator, suitable for a future system realization. In the

following, the design criteria and a detailed layout of an RFQ are presented which are considered most suitable for this application. Due to the high beam current and the continuous wave operation, a vane-type RFQ is favored instead of the rod-type (see section 3.1). Although many source parameters are already fixed (compare section 2.3), one main parameter for the RFQ is still free: the resonance frequency. Dependent on the frequency, several other parameters are influenced. The most obvious one is the size of the RFQ structure, since in a vane-type RFQ, the current path from one vane tip through the walls to the perpendicular vane tip define the inductance on the resonance circuit. In other words, a lower frequency requires larger inductance which implies higher vanes and larger diameter of RFQ tank. Furthermore, also the power loss of the RFQ structure is frequency dependent as figure 3.9, the result of TRACE3D [37] simulations indicate.

The resonant frequency also influences the beam dynamics: On one hand, the length

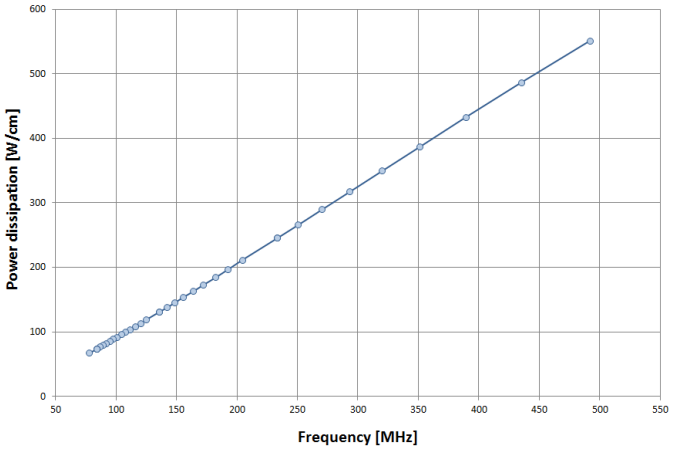

Figure 3.9: Frequency dependence of the power loss per cm RFQ length at a diameter-scaled RFQ cross-section (approximation, not taking into account beam dynamics)

of a unit cell is proportional to the frequency on the other hand, the length of a bucket is limited by the period length of the resonant frequency. Furthermore, the output bunch length is reduced by increasing the resonance frequency, since the typical output phase length of an RFQ is between 20-30° of the full RF period.

Concerning the application, a trade-off between time resolution and compactness on one side against lower input current, simpler LEBT pulsing capabilities and less power consumption on the other side has to be made. As explained in chapter 4, a pulsing system in the LEBT section of the entire accelerator system is necessary to fill only single buckets of the RFQ, to obtain the required pulsing capabilities. The pulse rep-

etition rate of the beam is not determined by the RFQ but by the LEBT. Therefore, for all resonant frequencies, one bucket has to be filled with $200\,pC$. This leads to a lower DC input current at lower resonant frequencies. Since the length of the bucket is inverse proportional to the resonant frequency, the filling can easier be realized at a lower frequency RFQ. The RFQ properties for several resonant frequencies are presented in table 3.1.

RFQ Frequency	/	MHz	**200**	**100**	**80**	**75**
Bunch Length required at RFQ entrance	/	ns	5	10	12.5	13.3
Charge per Bunch	/	pC	200	200	200	200
Required DC Input Current	/	mA	40	20	16	15
Appr. Inner Wall Diameter of RFQ Cavity	/	cm	29	53	65	69
Pulse Length at RFQ exit (30° Phase)	/	ns	0.42	0.83	1.04	1.11

Table 3.1: Overview of RFQ properties at different resonance frequencies for a pulse repetition rate of 3 MHz

A frequency of $100\,MHz$ seems to be a reasonable trade-off: Since a pulse length of $\leq 1\,ns$ is required, lower operation frequencies are not suitable. A higher frequency would lead to higher beam current as well as shorter pulse lengths requirements at the RFQ entrance. Thus, a resonant frequency of $100\,MHz$ was selected for a design study of a dedicated ACCIS-RFQ.
The design study was performed employing the RFQGen software package for beam dynamics calculations as well as Poisson Superfish [38] for the RF and CST Microwave Studio [39] for RF, thermal and mechanical calculations. The detailed RFQ design will presented in the next sections.

3.2.1 Beam Dynamics Design

The first parameter to take into account starting the RFQ beam dynamics design is the acceptable beam loss and RFQ transmission for the application. In the design of ion RFQ accelerators, a trade-off in transmission is usually accepted to reduce length or power consumption. Since the accelerated ions are deuterons which exhibit a significant cross-section for the neutron producing reaction $D(d,n)^3He$ even at deuteron energies of several ten keV, the transmission of the RFQ should be as high as possible. Deuterons lost from beam can get implanted into the wall. Following deuterons from

the beam hitting the wall at the same location can react with implanted deuterons and produce neutron background as well as causing activation. This stray radiation may interfere with the radiography detector system and falsify the results. To reduce neutron yield and taking into account the $D(d,n)^3He$ cross-section, the energy of the lost deuterons should be as low as possible.
To achieve this, a strong quadrupole focusing (B curve in figure 3.10) in the shaping section and in the gentle buncher section are required. At the exit of the gentle buncher a rather low-energy of $380\,keV$ could be realized. As a result of the beam dynamics optimization, particle loss occurs only between 90 and $150\,cm$. The maximum energy of lost deuterons could be determined to be $54.59\,keV$ (the average energy amounts to $37.76\,keV$).

Another main feature of this design is the steep inter-vane-voltage gradient (V/100 curve) of $29.7\,\frac{kV}{m}$, which leads to a compact length of about $7\,m$.

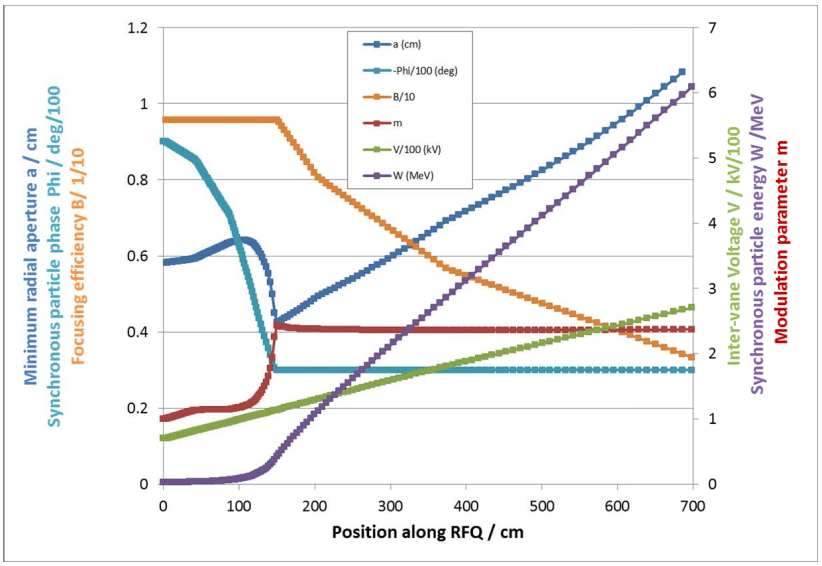

Figure 3.10: Overview of different beam dynamics parameters

In a regular constant voltage RFQ, the choice of the inter-vane voltage is always a trade-off: In the shaper and gentle buncher section, a high voltage is not necessary but typically, the peak electric field occurs in these regions because the vane-to-vane distances increase towards the high- energy end of the RFQ. This also limits the maximum voltage in a constant voltage design.
The voltage gradient enables raising the voltage in the acceleration section by keeping the voltage at a low level in the shaper/buncher section. This leads to an acceleration

gradient of 1 $\frac{MeV}{m}$ (W curve in figure 3.10). Although a shorter RFQ with lower final energy in combination with a drift tube linac (DTL) would be an alternative solution for the ACCIS source, the voltage gradient design makes the DTL obsolete and allows to obtain the full acceleration up to 6 MeV into a single RFQ. This also keeps the complexity of the entire system simple. The peak electric field stays below 1.8 times the Kilpatrick limit (see [40], an empirical guidance level for the maximum peak electric field possible without RF breakdown) over the entire RFQ length, because the radial aperture increases over the length. Such an electric RF field is nowadays achievable due to improvements in manufacturing capabilities like decreased surface roughness employing diamond tools. A modulation profile plot illustrating the vane tip distance to the beam axis can be found in figure 3.11.

In this figure, the vane tip distance at the beginning (valley of the vane modulation)

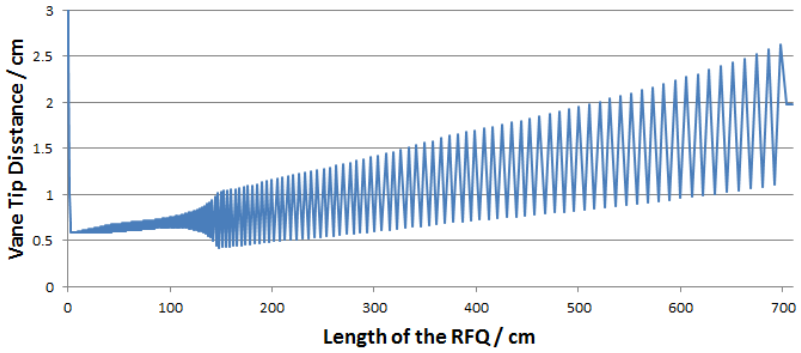

Figure 3.11: Vane tip distance to the beam axis over the RFQ length

and end (peak of the vane modulation) of each unit cell is plotted against the longitudinal position. In this plot, the different sections of the RFQ can nicely be identified. In the first 5 cm (radial matching section) the vane tip distance decreases from 3 cm to the nominal value of $\approx 0.6\,cm$, to catch the injected beam. In the following $\approx 30\,cm$, the modulation parameter m is close to 1 so peak and valley have almost the same distance to the beam axis. This is the shaper section where the beam is transversally shaped. In the following gentle buncher section from 30 to 130 cm the slope of peak and valley is slowly increased such that in the remaining section, the acceleration section, maximum accelerating gradient can be achieved.

Figure 3.12 shows the multi-particle RFQTrace simulation result of the ACCIS RFQ. The figure is separated into four plots: In the first two plots, the transversal and in the third the longitudinal particle position of the beam is depicted along the RFQ. The abscissa in all plots is not given in cm, but in number of unit cell. The red dotted line in the plots indicate the border of the acceptance window. As the first two plots

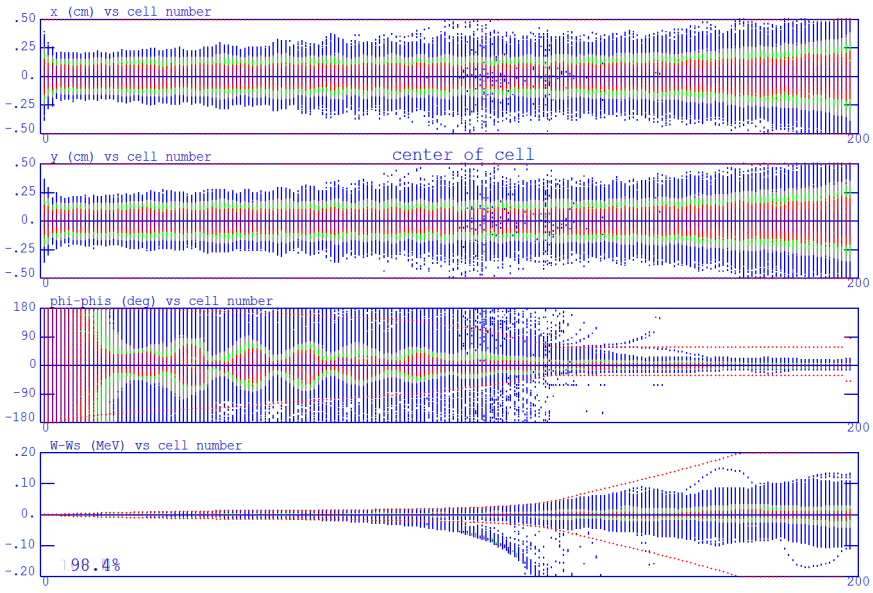

Figure 3.12: RFQGen simulation output (10000 particles) of the ACCIS RFQ

indicate, no particle is lost due to transversal position/transversal focusing. The main reason for particle loss is based on the bunching, since there are particles outside of the longitudinal acceptance window in the third plot. In the fourth plot, the particle energy is plotted over the cell number. Here, the lost particles can be found as not correctly accelerated particles falling out of the acceptance window in the second half of the plot. The transmission of the RFQ was determined to be 98.4 %. An overview of the RFQ design results can be found in table 3.2
The frequency was selected to be 100 Mhz at a design DC input current of 20 mA.

Ion Species	Deuterons
Frequency	100 MHz
DC Input Current	20 mA
Final Energy	6 MeV
Exit Bunch Length	0.83 ns
Inner Wall diameter	66 cm
Length	709.5 m
Transmission	>98%
Dissipated Power	419 kW

Table 3.2: Overview of the ACCIS RFQ design results

To reach 6 MeV which leads to sufficient neutron and gamma yield (see 2.3), a total

RFQ length of 709.5 m is required, which is a compact accelerator. The deuteron bunch length at the exit of the RFQ is 0.83 ns which is well below the specification of up to 1 ns. The total dissipated power of 419 kW is even below the approximated value for this frequency of figure 3.9. The inner wall diameter is slightly larger than approximated in table 3.1. The reason is the inter-vane voltage gradient.

3.2.2 RF-Design

In the first step of the RF design, RFQfish (a module of the Superfish package [38]) was employed to calculate the resonator shape at 50 slices through the RFQ, oriented perpendicular to the beam axis and distributed equally over the entire length. The Entire RFQ can be derived by interpolating between these slices. Here, parameters like the tip-to-tip distance or the specific wall geometry of the inner RFQ volume is varied to achieve the desired local operation frequency and electric field distribution. In this step, the vane tip modulation is considered to be constant ($m = 1$). Due to the increase of radial aperture to the end of the RFQ, the surface path from one tip to a perpendicular one needs to increase dramatically, in order to compensate for the reduced capacitance. Figure 3.13 shows the resonator shapes (only one quadrant of the entire inner RFQ volume) of the low-energy end as well as the high-energy end.
Since the length of each unit cell is determined by $\frac{\beta\lambda}{2}$, a frequency detuning can lead

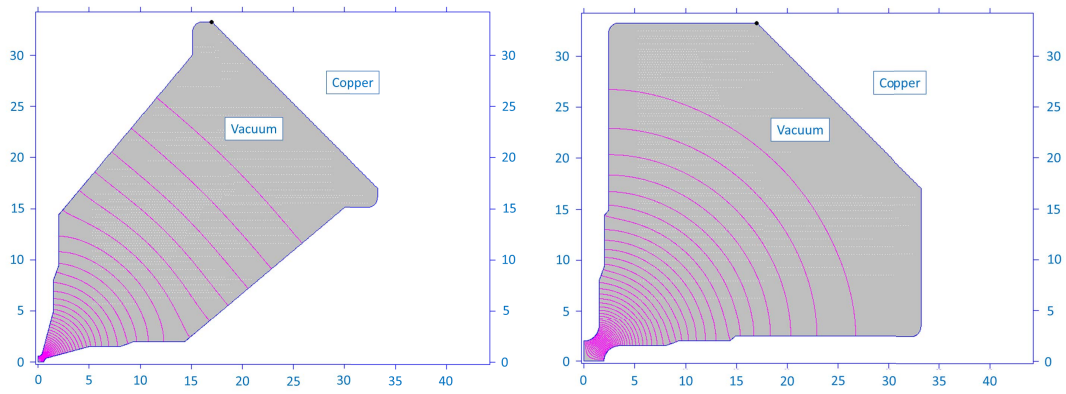

(a) low-energy end (b) high-energy end

Figure 3.13: Cross-sections of the RFQ resonator (grey: one quadrant of the inner volume, pink lines: electric field distribution)

to an incorrect energy gain per unit cell and thereby to the loss of beam particles. Thus, all factors which might cause detuning need to be analyzed in detail to compensate them. Before the sources for detuning can be quantified, the impact of different detuning mechanisms can be determined employing Superfish RF simulations.

There are two major possibilities for a detuning of the RFQ cavity: First, the vane tips or its body can be deformed, which can be interpreted as a local displacement for simulation purpose. To simulate the effect of vane tip deformation, the distance between the beam axis and all vane tips was displaced in parallel. The results of the simulations for the low-energy (LE) end as well as the high-energy (HE) end can be found in figure 3.14. It shows that the detuning is linear with a gradient of 0.18 to 0.48 MHz per 0.1 mm displacement.

Another deformation possible is the deformation of outer walls (body deformation).

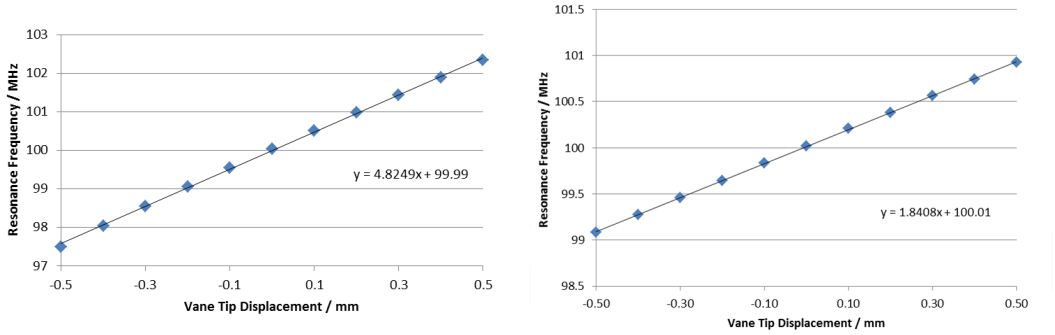

(a) low-energy end (b) high-energy end

Figure 3.14: Simulation results of the vane tip sensitivity calculations

For this purpose, the effect on resonance frequency of the increase in RFQ cavity inner diameter was simulated for both the low-energy and high-energy end. The results of these simulations can be found in figure 3.15. Both results (vane tip and body sensitivity) are e.g. necessary to calculate the position of the cooling channels of the RFQ structure (compare section 3.2.4). Furthermore, these sensitivities limit the required manufacturing tolerances for milling as well as brazing of the RFQ structure. In a final

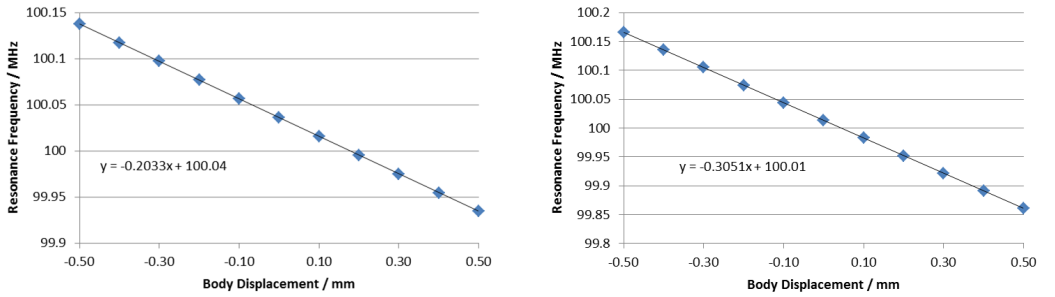

(a) low-energy end (b) high-energy end

Figure 3.15: Simulation results of the body sensitivity calculations

test of the basic RF model, CST Microwave Studio was employed to determine the

quadrupole modes in a three dimensional model of one entire quadrant. To create the model, the output of RFQfish (the 50 two-dimensional slices of the quadrant) were interpolated. The simulation was performed employing adaptive meshing techniques, so the number of tetrahedrons was raised from $5 \cdot 10^5$ to $2 \cdot 10^6$ in four iterations. Since the results seem to be converged, the mesh study was stopped. Figure 3.16 shows on the left side the mesh view of the final mesh. On the right, the first three quadrupole modes can be found. The frequency of the first mode could be determined to be $99.995\,MHz$ in the last iteration. The vacuum model of one quadrant was employed

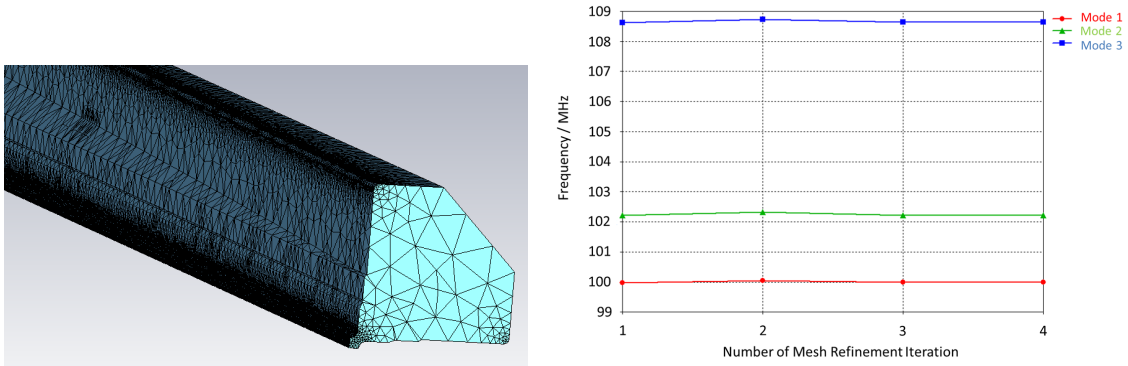

(a) (b)

Figure 3.16: (a) Mesh view of the CST Model (b) simulation results of first 3 quadrupole modes

in the next step, to create a conducting model of the entire RFQ. In this step, the so called undercuts have to be designed. Undercuts are notches in the start and end regions of the vane. The undercuts fulfill two functions: On the one hand, without undercuts, the vanes would be short-circuited to the end plates. Hence, undercuts enable an option for the magnetic flux to flow around the vanes (see figure 3.17). On the other hand, they can be employed for local detuning of the RFQ to induce an electric field gradient. The detuning - and thus the field gradient - is dependent on the depth of the undercuts. The vane potential at the HE end increases with deeper undercuts, whereas at the LE end, the vane potential increases with a deeper LE undercut but decreases with a deeper HE undercut (see figure 3.18).

The ideal depths of the undercuts needed to be determined by employing multiple CST simulations, in which these lengths were varied. Since the CST simulation results are normalized to $1\,J$ stored energy, whereas in the ACCIS RFQ in regular operation $13.64\,J$ would be stored, the results have to be re-scaled. Furthermore, the inter-vane voltage is proportional to the square-root of the stored energy and each vane carries only half of the inter-vane voltage. The required inter-vane voltages are $70\,kV$ at the

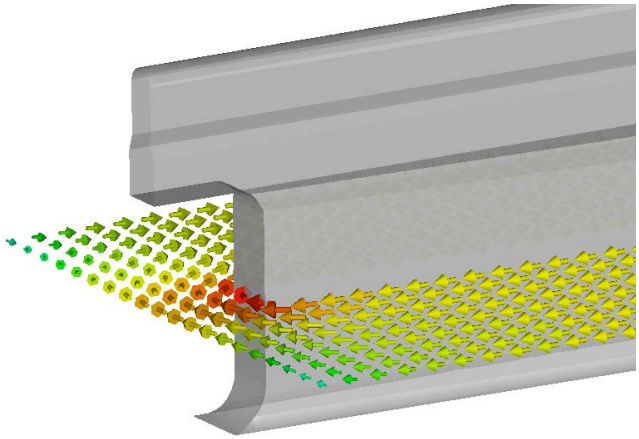

Figure 3.17: Magnetic field in the undercut region

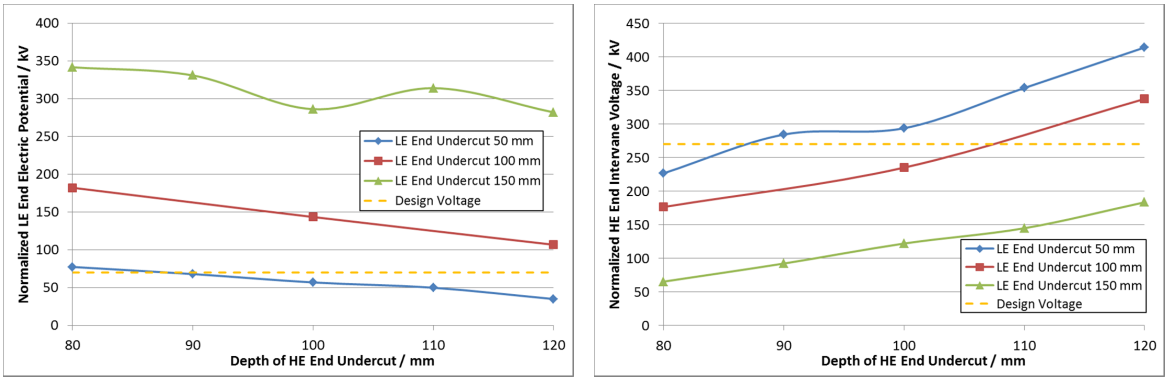

(a) (b)

Figure 3.18: Normalized vane voltages of (a) low-energy end and (b) high-energy end varying the high-energy undercut depths (abscissa) as well as the low-energy undercut depths (different curves)

low-energy and 270 kV at the high-energy end. In further simulations employing improved mesh quality, reasonable undercut depths could be determined: At a depth of 62.5 mm at the LE end and 93 mm at the HE end, an inter-vane voltage ramp starting at 70.7 kV and reaching 270.5 kVcould be realized. The remaining difference to the inter-vane voltage design values can be optimized and achieved during final tuning of the manufactured RFQ structure.

To adjust the distance between the resonant quadrupole mode and the surrounding dipole modes, so called dipole suppressor rods can be installed. These rods are placed perpendicular, on top of the end plates such that in each quadrant one cylindrical rod is placed. Again, these rods act as a dissipater and induce a local detuning which only affects the dipole modes, if the transversal positioning is correct. To find the exact

position, SUPERFISH simulations of both end were performed, in which the distance of a 48 *mm* diameter rod to the beam axis is varied. The results for both ends can be found in figure 3.19. For the low-energy end, a distance of 9.58 *cm* in transverse

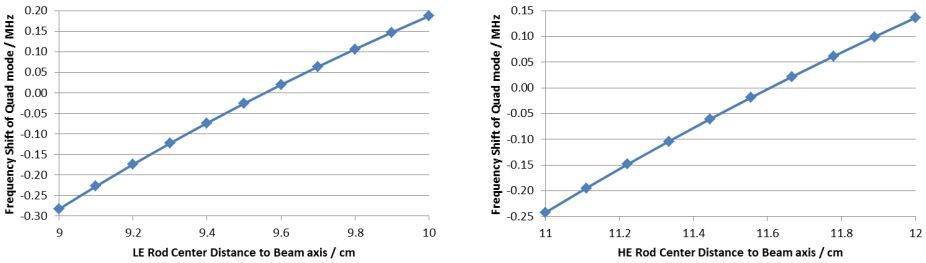

(a) (b)

Figure 3.19: Determination of the transversal dipole rod position for the (a) LE and (b) HE end

direction between beam axis and the center of the rod could be estimated, whereas at the high-energy end this distance yields to be 11.6 *cm*. The result of the SUPERFISH simulations at the calculated distances can be found in figure 3.20. The position of

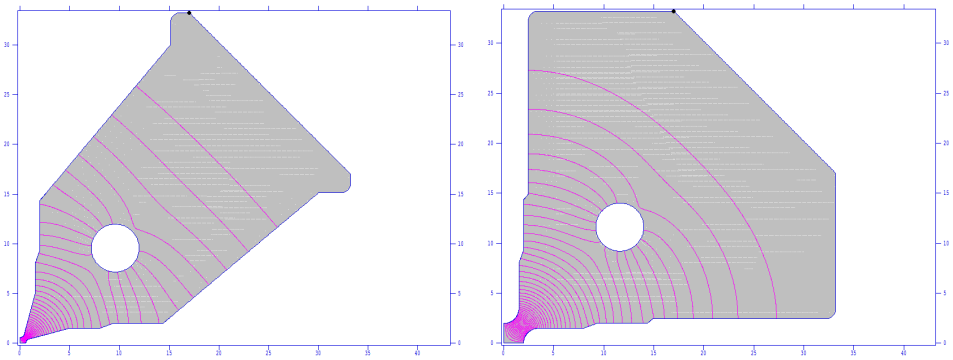

(a) (b)

Figure 3.20: SUPERFISH simulation of determined rod position at (a) LE and (b) HE end

the dipole modes in the frequency spectrum is dependent on the length of the rods. In a CST simulation of the entire three-dimensional RFQ, the length of the rods was varied, in order to determine the optimal conditions. The result of the simulations employing the same length at all rods are shown in figure 3.21. For the optimal operation of the ACCIS RFQ, two options are possible: As the result indicates, either no dipole stabilizer rods or rods longer than 500 *mm* needs to be employed. Since the RF power loss at the rods increases with rod length, the first solution will be implemented.

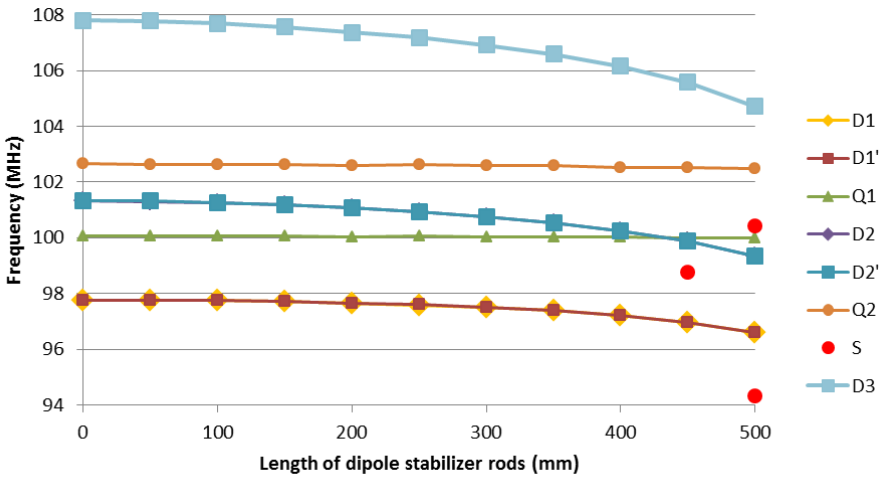

Figure 3.21: Determination of the optimal dipole stabilizer rod length

This leads to a minimal mode separation of 1.28 MHz between the quadrupole ("Q") and the dipole ("D") modes. The "S" modes which appear at rod lengths larger than 400 mm are so called spurious or rod modes. The electric field distribution of such a mode can be found in figure 3.22.

To correct for manufacturing tolerances and tune the RFQ to the correct frequency,

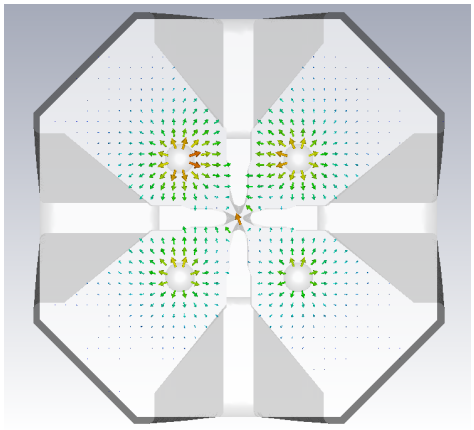

Figure 3.22: Electric field distribution of a rod mode

so called slug tuners are employed. Slug tuners are cylinders made of copper, which are inserted into the RFQ cavity on the diagonal axes of the quadrants. A schematic view of a slug tuner can be found in 3.23. By increasing the penetration depth of the tuner, the inductance of the body is decreased since the magnetic field is suppressed. Thus, by employing slug tuners, the resonance frequency of the RFQ can be slightly increased. Since the slug tuner acts as a local detuning of the fundamental quadrupole mode, not only the frequency but also the electric field gradient is influenced. To de-

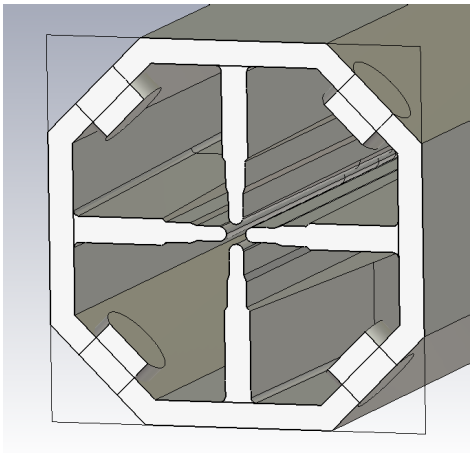

Figure 3.23: Schematic view of slug tuners at HE end

termine the tuning sensitivity as well as the effect on the field gradient, simulations have been performed were the penetration depth of four slug tuners (one located in each quadrant) was varied. The simulation was performed for slug tuners located $100\,mm$ upstream of the low-energy end and repeated for a location $100\,mm$ before the high-energy end.

As figure 3.24 indicates, slug tuners located at the low-energy end exhibit a tuning

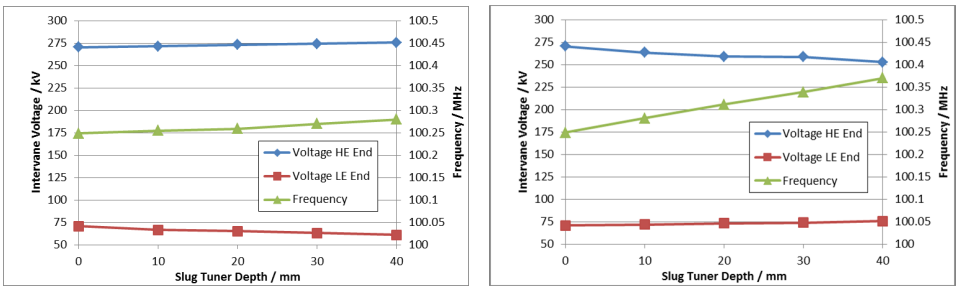

(a) (b)

Figure 3.24: Effect of slug tuners dependent on penetration depth at (a) LE and (b) HE end

sensitivity of $0.78\,\frac{kHz}{mm}$ whereas the tuning sensitivity for the same slug tuners located at the high-energy end is $3.01\,\frac{kHz}{mm}$.

Furthermore, an inverse effect comparable to the depth of the undercut can be found: When the penetration depth of slug tuners located at the high-energy end is increased, the low-energy end voltage is increasing whereas the HE end voltage is decreasing. For slug tuners at the low-energy end, the effect is inverted. Similar to the frequency influence, the influence on field gradient is also higher at the HE end. Thus, at some place along the RFQ, slug tuners principally influence the frequency and barely affecting

the field gradient.

3.2.3 Mechanics Design

To estimate the required thickness of the RFQ-cavity walls, a mechanical deformation simulation of 10 mm thick cross-sections taken both at the low-energy as well as high-energy end was performed employing CST MPhysics Studio. The stability requirement concerning maximum allowed displacement was defined to be 25 μm, since such deformations can be corrected after manufacturing by tuning. This value corresponds to a frequency change of the ACCIS RFQ of 120.6 kHz at the low and 46.0 kHz at the high-energy end. In the mechanical simulation of the ACCIS RFQ, the gravitational force as well as the vacuum pressure was included, while the ground face was fixed. As figure 3.25 indicates, a cavity with a wall thickness of 50 mm fits the requirements over the entire length of the RFQ.

In a further investigation, the stresses as function of wall thickness were analyzed

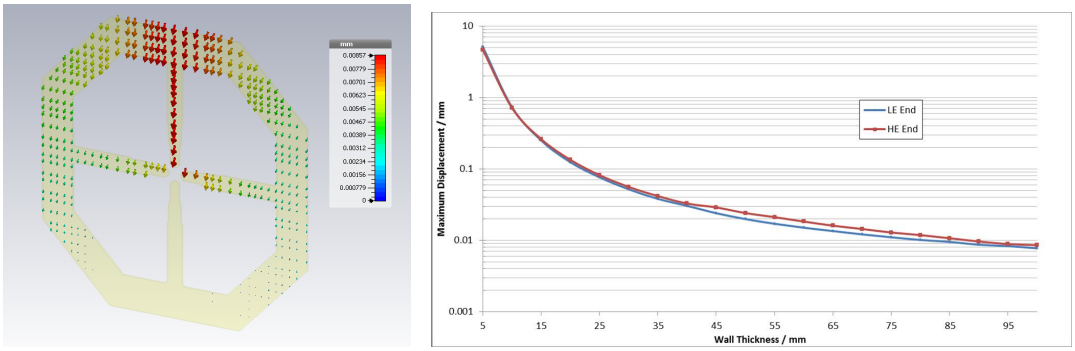

(a) (b)

Figure 3.25: (a) Displacement of the vane at HE end (wall thickness 100 mm) (b) displacements at LE and HE end as function of wall thickness

in the same way as the mechanical displacement. The results are shown in figure 3.26. The stress value necessary for plastic deformation or rupture (the so called yield strength) is dependent on composition, on dimensions and the way the raw material was treated. For oxygen-free electronic copper, a minimal value of 69 MPa is necessary to achieve these deformations [41]. As the results indicate, for a wall strength thicker than 15 mm, the yield strength limit is not reached. So the limiting factor is the displacement.

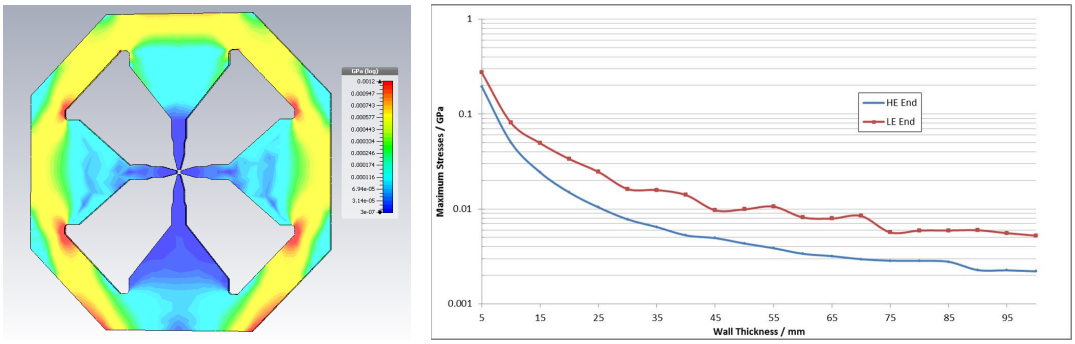

(a) (b)

Figure 3.26: (a) Van Mises stresses at the LE end (wall thickness 100 mm) (b) stresses as function of wall thickness

3.2.4 Thermal Design

The thermal design is based on two different aspects of RF-based thermal heating: the first is the undesirable effect of heating several of the components. The other is the heating-induced tuning, exploited here in the principal RF-tuning concept, which is based on thermal expansion.

As determined in section 3.2.2, two different expansions are possible inside the RFQ which have three effects: On the one hand, expansion of the outer tank diameter leads to a lower resonance frequency, since the inductance of the resonant circuit is increased. Furthermore, the tip-to-tip distance is increased due to the expansion of the body, which leads to an increase of resonance frequency. On the other hand, a heat induced expansion in the vane tip region reduces the tip-to-tip distance what leads to an increase of the capacitance and thus to a reduction of the resonance frequency.

To use these effects for resonance tuning, two separate cooling channel circuits are employed, one is located close to the vane tips, the other is located at several positions at the outer body. Once an optimal position of the vane tip cooling channel is selected, the third effect can be employed to equilibrate the remaining two effects. By once adjusting only the particular coolant flow velocity in each of these two circuits, the same primary coolant can be employed in both. Since heat deposition is proportional to RF power, once adjusted correctly, the coolant flow velocities do not need to be readjusted. Of course, prior to the thermal tuning, the resonant frequency must be fixed once in low power operation employing fixed slug tuners.

In the thermal design process, the correct position as well as dimension of the cooling channels needs to be determined such that the thermal resonance tuning scheme can be applied.

All thermal simulations were performed employing the thermal solver of the CST MPhysics Studio. Since CST does not support flow of coolant media, analytical calculations had to be performed do determine the heat transfer coefficient of a turbulent water flow at the selected cooling channel diameter and coolant flow velocity. The heat transfer coefficient α can be calculated via

$$\alpha = \frac{Nu \cdot \lambda}{d} \tag{3.22}$$

where λ is the heat conductivity of water and d the diameter of the cooling channel. In general, the Nusselt number Nu expresses the ratio between convective to conductive heat transfer. For turbulent flow through tubes it can be determined by means of the McAdams equation [42]

$$Nu = 0.024 \cdot Re^{0.8} \cdot Pr^{\frac{1}{3}} \tag{3.23}$$

Here, Pr is the temperature dependent Prandtl number of the coolant, which is 6.99 for water at 20°C. The Reynolds number Re indicates if the coolant flow is either laminar (low Reynolds number) or favorably turbulent (high Reynolds number) and can be calculated employing

$$Re = \frac{d \cdot v_f}{\nu} \tag{3.24}$$

To satisfy the McAdams equation, the Reynolds number has to be kept within the limits $10^4 < Re < 10^5$. where $\nu = 1 \cdot 10^{-6} \frac{m^2}{s}$ is the viscosity of the coolant and v_f the flow velocity. For reasons of convenience, the flow velocities will be converted into flow rates in the following.

For the thermal design, two alternating optimizations need to be performed: In the first step, a cooling channel layout must be found by varying cooling channel positions and diameters, to be able to conduct the heat out of the RFQ structure. To operate at the RFQ a temperature with acceptable outgassing rate, but with lowest amount of cooling water required, a temperature limit of $343.15K$ was assumed. In a second optimization step, the water flow rates are varied to find the operational point for operating the RFQ in a tuned regime. As shown above, this means that the frequency shift effect of body expansion exactly compensates the frequency shift due to tip-to-tip displacement. Certainly, the position and diameter of the cooling channels has direct influence on tuning performance: If the cooling channel diameter is increased, less flow is required to achieve the same heat dissipation. Furthermore, the distance between both cooling channels has an influence on the gradient of shift dependence and as a function of flow rate.

Of course, the RF-induced heat load to the RFQ structure increases in proportion to the longitudinal dimension of the RFQ. Since these optimizations require lengthy simulations, they were performed only for cross-section slices representing the low-energy end and the high-energy end. The undercut region is not included in the tuning simulations, but they will be equipped with separate, flow-adjustable coolant circuits, to achieve tuning.
The final cooling channel layout after the performed optimization steps includes vane cooling channels with a diameter of $20\,mm$, placed in each vane in a distance of $130\,mm$ to the beam axis. Two body-cooling channels with a diameter of $25\,mm$ are provided for each quadrant. They are located at a transversal distance of $360\,mm$ to the beam axis, $95\,mm$ shifted from the center of the vane. The coolant flow rates over the entire length of the RFQ, at the coolant temperature of $293.15\,K$ could be determined to be $36.8\,\frac{l}{min}$ for the vane tip cooling channels and $46.4\,\frac{l}{min}$ for the body cooling channels. Under RFQ operation, the temperature profile of the vane cross-sections of the low-energy end and the high-energy end can be found in figure 3.27. This cooling channel layout employing the previously stated flow rates leads to tuned

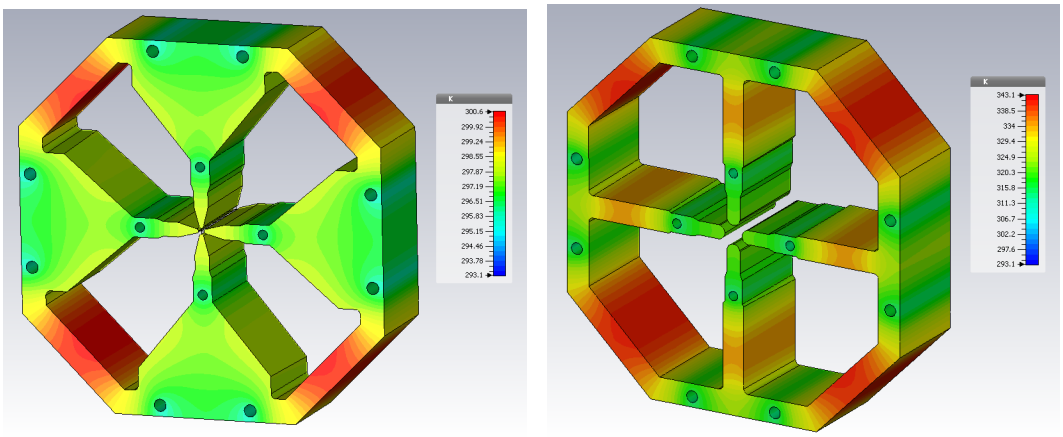

(a) (b)

Figure 3.27: Temperature distribution in K of the operating RFQ (Dissipated heat of entire RFQ $410\,kW$)at the (a) low-energy end (b) high-energy end

operation of the RFQ. To determine the heat induced frequency shift, the temperature distribution result of the thermal solver was taken as an input for the mechanical solver. The hereby achieved mechanical displacements can be transformed to frequency shifts employing the simulation results obtained in the Superfish simulations presented in section 3.2.2. The tuning behavior can be illustrated by plotting the frequency shift against the flow rate variations for one of the cooling channels. Figure 3.28 illustrates the tuning behavior of cross-sections of the low-energy and high-energy end of the

RFQ in dependence of the body channel flow rate. The curve of the low-energy end

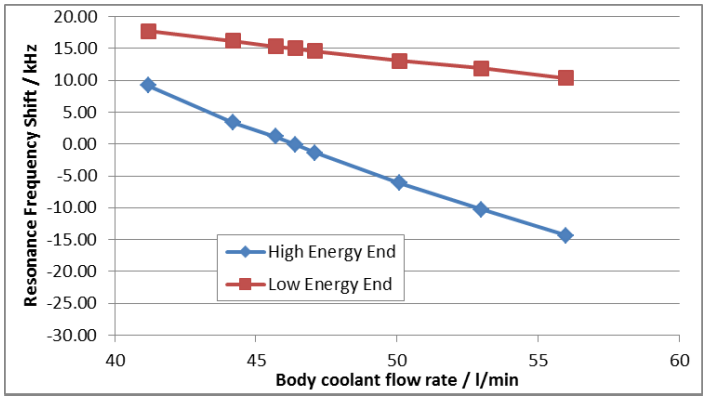

(a)

Figure 3.28: Tuning behavior of in dependence of body coolant flow rate of low-energy and high-energy end (constant flow rate over entire RFQ)

is flatter than the other one. Although no zero-crossing occurs at the desired point of $46.4\frac{l}{min}$ (what would correspond to perfect tune), only a small discrepancy of $15\,kHz$ in the resonance frequency was obtained, which is less than $0.02\,\%$. According to the approximation considering just two extremal values (low-energy and high-energy end), no further coolant flow simulations were deemed necessary. For a more accurate result, the simulation must include the entire RFQ structure instead of only two cross-sections, since each slice of of the RFQ influences the overall resonance frequency. Since the RFQ would be split into different modules for manufacturing issues, the coolant-flow could be optimized for all modules separately to overcome this small detuning. In this case, the coolant flow of the vane tip channel would be reduced in the first module(s), to increase the effect on heat induced vane tip expansion. This is possible, since less power is dissipated at the low energy end. As figure 3.29 indicates, a tuned operation of the low-energy end can be achieved, by reducing the vane tip coolant flow to $22.1\,\frac{l}{min}$.

Another part of the RFQ which needs cooling are the end plates of the low-energy and high-energy end. The end plates will be equipped with eight perpendicularly deep-drilled cooling channels with a diameter of $20\,mm$. To determine the required coolant flow, a parameter study was performed, where the coolant flow was varied and the maximum temperature at the surface of the different end plates was measured. The result can be found in figure 3.30. As the figure indicates, the temperature variation above $26.8\,\frac{l}{min}$ is only minor. Of course, due to the field gradient, the maximum

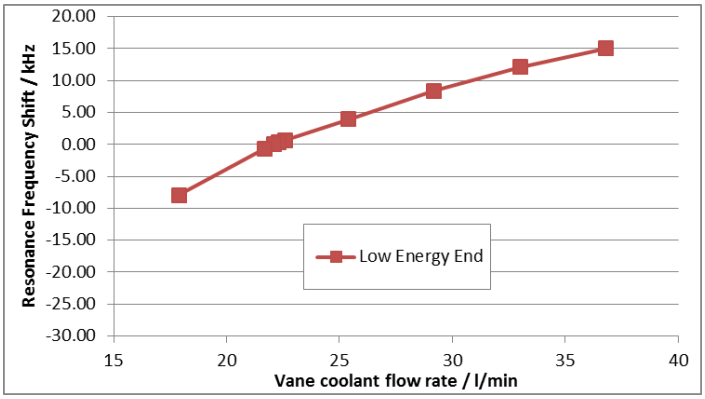

(a)

Figure 3.29: Tuning behavior of LE end as function of vane coolant flow rate (reduced flow rate for LE end)

temperature at the high-energy end is always higher.

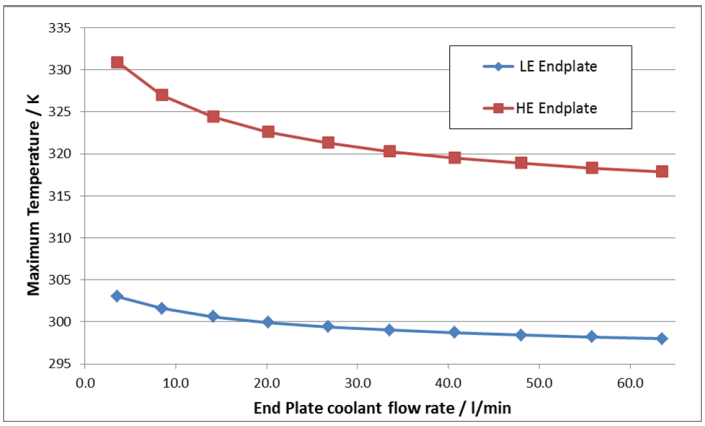

Figure 3.30: Maximum temperatures of end plates a different coolant flows

The layout of the channels can be seen in figure 3.31c. Figures 3.31a and 3.31b show the temperature distribution at the selected coolant flow rate of 26.8 $\frac{l}{min}$.

The last temperature critical element which was examined in this study are the undercuts. Especially at the high-energy end, the high surface currents due to the strong field gradient lead to an intense temperature increase, which has to be cooled separately. Due to limitations in manufacturing, no regular cooling loop for the undercuts can be employed since no brazing edge or drilled and plugged holes is should be present at the high-voltage surfaces. One special approach to introduce undercut cooling is a sloped coaxial cooling lance from the vane base to the undercut. Here, only one deep drilled hole is employed, whereas an inner cooling pipe acts as the water inlet

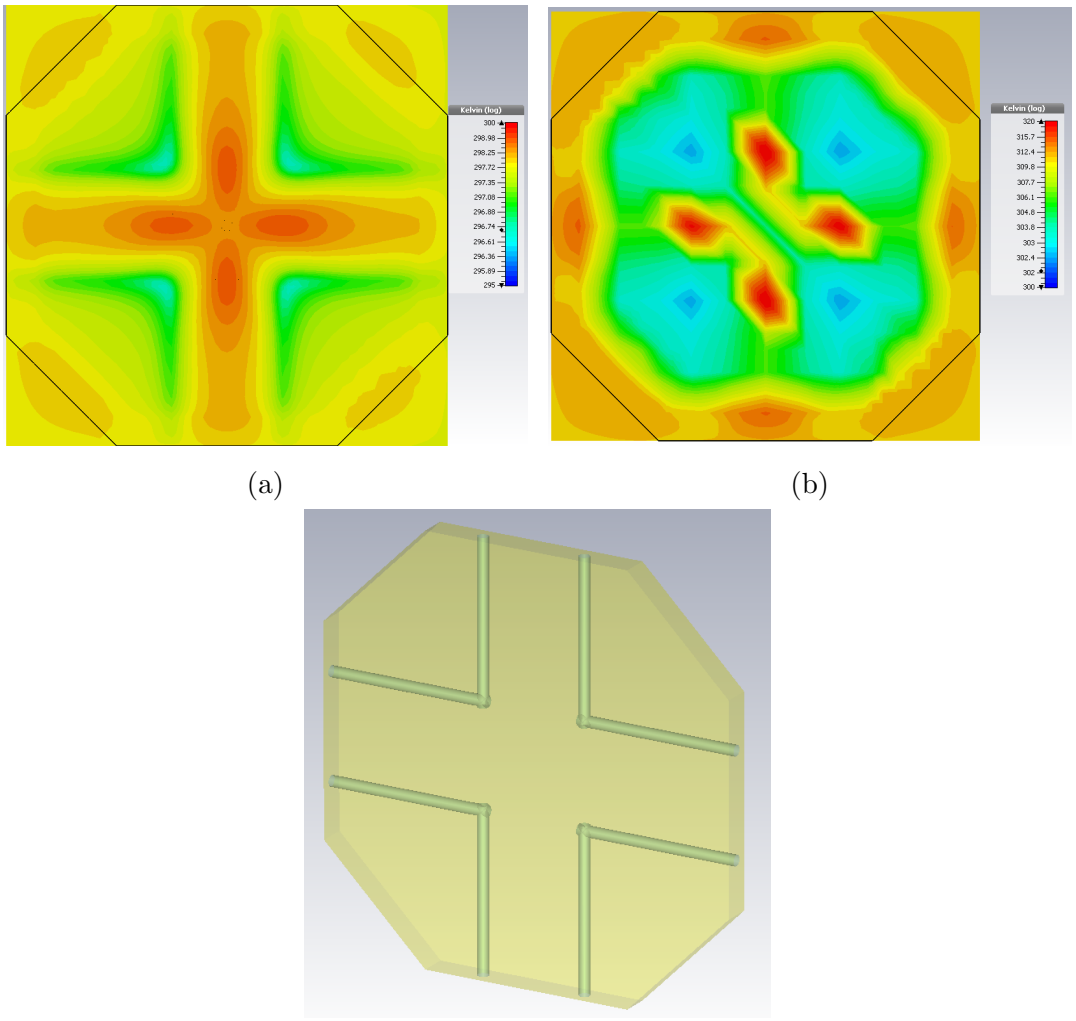

(a) (b)

(c)

Figure 3.31: (a) LE end plate temperature distribution at 26.8 $\frac{l}{min}$ coolant flow; (b) HE end plate temperature distribution at 26.8 $\frac{l}{min}$ coolant flow (c) cooling channel layout;

while the space between the pipe and the copper RFQ structure acts as the outlet. A cooling lance with outer diameter 25 mm and inner diameter 18 mm was selected to have approximately equal cross-section in both channels - in and out. As figure 3.32 indicates,

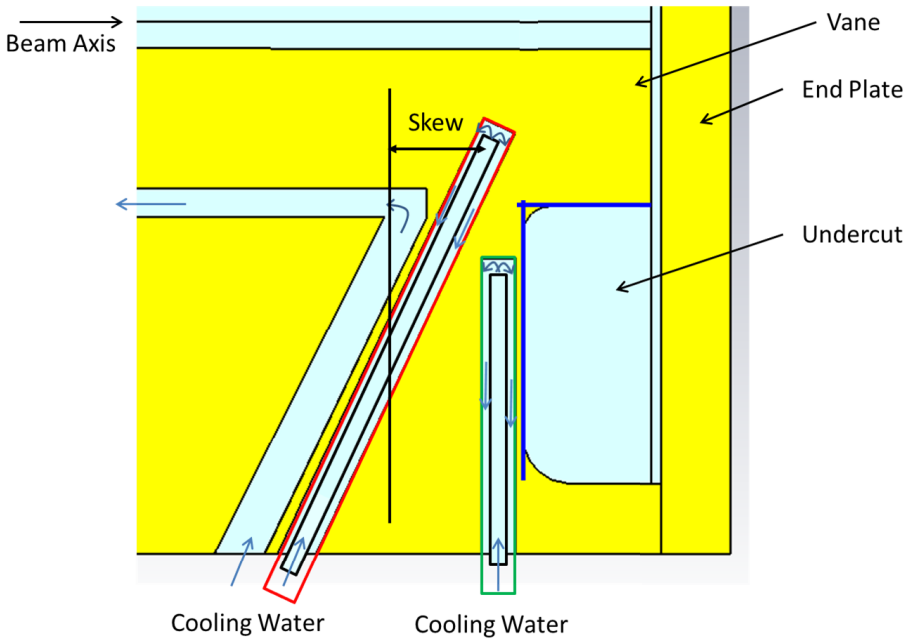

Figure 3.32: Position of the coaxial cooling lance (marked red), additional vertical coaxial cooling channel (marked green) as well as the temperature profile curves (marked blue)

either the residual top part close to the vane or the vertical surface region can be optimally cooled, depending on the angle of the cooling lance. In multiple simulations, the angle of the coaxial lance cooling channel was varied, to determine the optimal slope as a compromise of both effects. A very high coolant flow of 35.1 $\frac{l}{min}$ was employed for the coaxial lance.

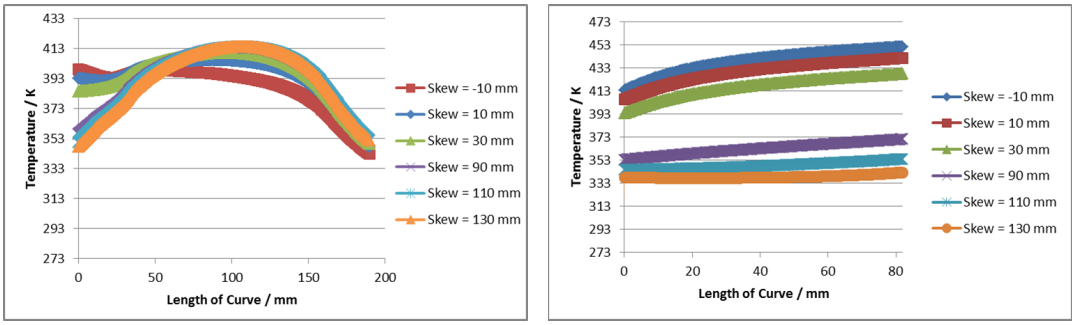

(a) (b)

Figure 3.33: Simulation results of (a) vertical and (b) horizontal temperature profile employing only the skewed cooling lance

Figure 3.33 indicates that no angle can be found to reach temperatures below 343 K with a single coaxial lance. Thus, the simulation was repeated, employing a second but vertical coaxial cooling lance in close proximity to the vertical edge (compare figure 3.34).

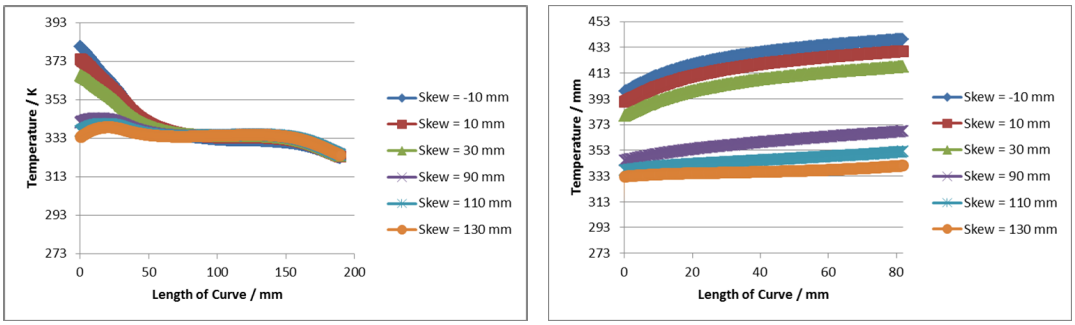

(a) (b)

Figure 3.34: Simulation results of (a) vertical and (b) horizontal temperature profile employing additional vertical cooling lance

Employing a skew of 130 mm and the same coolant flow of 35.1 $\frac{l}{min}$ per coaxial lance, the required maximum temperature of less than 343 K can be achieved. It has to be technically clarified, if such a coolant flow rate can be realized at coaxial lance with outer diameter 25 mm. Otherwise, the outer diameter has to be enlarged. In principle, the dissipated increased heat dissipation due to the field gradient at the high-energy undercuts can be cooled to reasonable temperatures.

The thermal simulations show that cooling of the entire RFQ can be achieved. Thus, the RF design leads to a realistic and operational accelerator cavity. Furthermore, is

was presented, that the determined cooling channel layout leads to tuned RFQ operation employing the correct set of coolant flow values.

3.3 The Necsa RFQ-Accelerator Facility

The manufacturing and commissioning of an entirely new accelerator system was financially unachievable during the ACCIS project, but within the collaboration an RFQ accelerator was available for evaluating the ACCIS radiation source. An existing accelerator which could be used as a demonstrator for an ACCIS radiation source was identified at the South African Nuclear Energy Corporation SOC Limited (Necsa) [43] in Pelindaba, South Africa. It is a 4-rod-type RFQ accelerator originally designed by A. Schempp and the accelerator working group at the Institute of Applied Physics in Frankfurt University [44] and manufactured by NTG Neue Technologien GmbH and Co. KG in Gelnhausen, Germany [45]. It was built for the purpose of detecting diamonds in kimberlite employing dual-energy neutron radiographic methods by the diamond mining and trading company DeBeers [46]. This project called Diamonds WIthin Kimberlite (DWIK) had been discontinued. A schematic drawing of the DWIK accelerator system can be found in figure 3.35[1].

The accelerator system consists of a multi-cusp deuteron source with RF-based plasma heating where a beam current up to $50\,mA$ is extracted with an energy of $35\,keV$ (according to specifications). The ion source is followed by an LEBT section which includes two electrostatic einzel lenses as well as an electrostatic x-y steerer. The main accelerator stage is a almost $4\,m$ long, 4-rod type, $200\,MHz$ RFQ, which accelerates the deuterons up to $4\,MeV$.
In order to rapidly alternate between two different deuteron energies, the RFQ is followed by a post-accelerator section which consists of a $1MeV$ booster (see 3.39a for an overview and [47] for further information), which can be operated either in accelerating or decelerating mode depending on the phase angle relative to the RFQ phase. The three-gap booster consists of two drift tubes mounted on spiral arms surrounded by two drift tubes at ground potential located at the entrance and exit of the tank. Compared to a 4-rod-type RFQ, the resonant system of the spiral booster is constituted by the capacitance of the drift tubes relative to the ground tubes, with the spiral arms acting as the inductance. The booster is RF-driven with $200\,kW$ at the resonance frequency of $200\,MHz$.

[1] Private Communication - C. Franklyn, NECSA

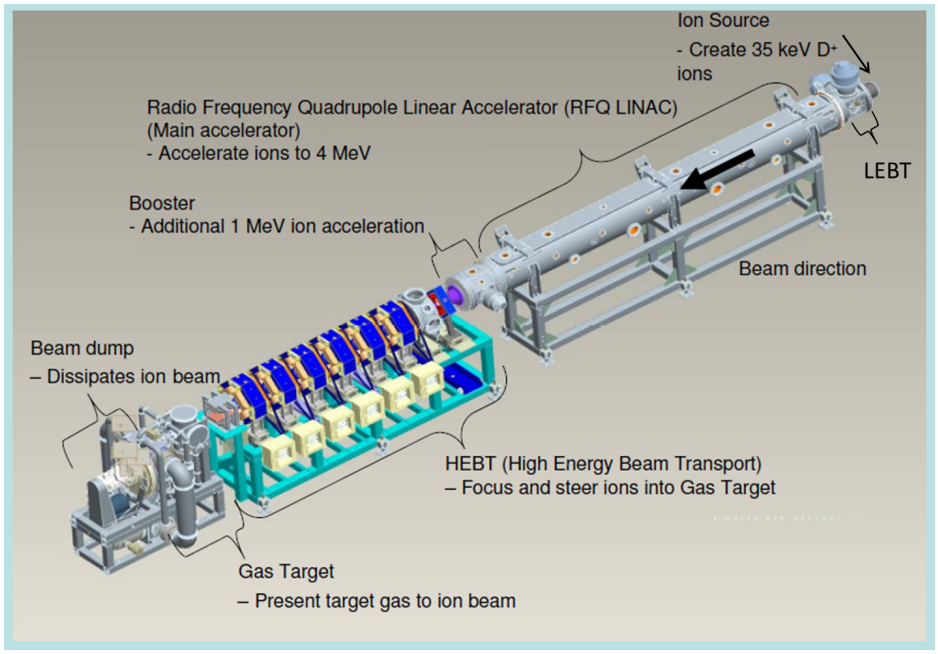

Figure 3.35: Overview of the Necsa DWIK RFQ-Accelerator Facility

A single, small quadrupole magnet is followed by a diagnostics chamber and a HEBT consisting of 6 quadrupoles in a FOFODODOFOFO (F stands for a focusing-, D for a defocussing-magnet and O for a drift) configuration, the beam is focused on a deuteron-gas target for neutron production before the beam is dumped at a water-cooled rotating tungsten-disk beam dump.

There are several reasons, why the accelerator was not operating according to original specifications: When DeBeers stopped the project, only a few of the previous accelerator personnel were taken over by Necsa and so the Necsa group had to familiarize themselves with the machine on their own. Furthermore, the documentation of the system was not handed over in entirety by DeBeers. In addition, the accelerator system was designed to work as a simple turn-key machine, so that necessary beam diagnostic were either not foreseen a-priori (e.g. a quantitative current transformer in the entrance of the RFQ), or were not taken into operation again after the stoppage (e.g. TOF-probes in diagnostics chamber).

By design, the accelerator should be able to operate with a duty cycle of 20 % . But due to tripping problems of the ion source as well as the conditioning state of the RFQ, only a time-averaged beam current of $1\,mA$ at a duty cycle of $0.8 - 1.2\,\%$ could be achieved during the first experiments.

Part of this project comprised the analysis of the machine status, as well as activities to improve the operating status of the machine. Details on the accelerator inspection

and component simulation are given in this chapter.

3.3.1 RFQ Simulation and Evaluation

To obtain a first impression on the operation of the RFQ and to test the ability of the machine to accelerate a single beam-bucket of deuterons without losing too many particles to neighboring buckets, a multi-particle CST simulation was prepared to visualize the behavior of the various sections of the RFQ. In a first electromagnetic simulation, the four rods including the correct modulation were modeled employing a fixed potential distribution of the inter-vane-voltages. The radial matching section was only approximated. This electrostatic field was exported to be employed in particle-in-cell simulations, oscillating at a frequency of $200\,MHz$. In a first particle simulation with enabled particle-to-particle forces (space-charge interaction) a $5\,ns$ long $36\,keV$ deuteron beam-bunch with average beam current of $10\,mA$ was injected and transported through the RFQ. Figure 3.36 shows some important parts of the simulation, such as the injection of the beam to the shaper section (a), during the bunch formation process in the gentle buncher section (b) as well as the extraction of the $4\,MeV$ bunch at the end of the accelerator. Although only a single $5\,ns$ bunch is injected

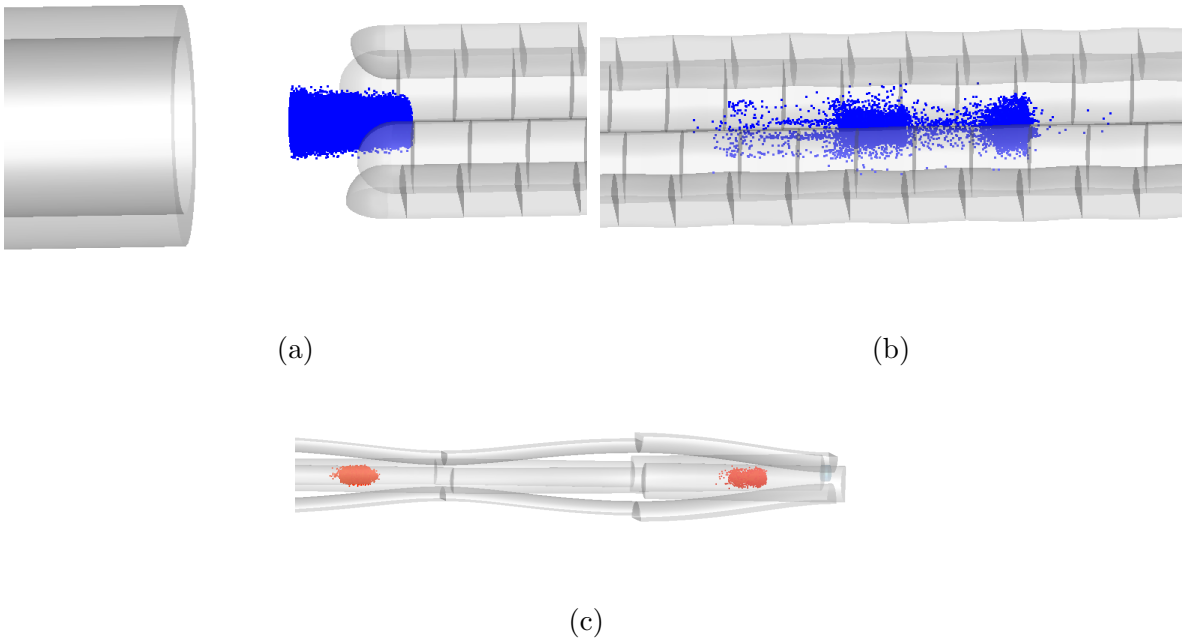

(a) (b)

(c)

Figure 3.36: DWIK RFQ CST PIC Simulation(a) beam injection to the RFQ (b) bunching in gentle buncher (c) accelerated bunch

into the RFQ, two bunches (plus an additional, much smaller one) are found to leave

the RFQ. The reason for this is the space-charge as well as the fact, that the bunching of the RFQ starts only after around $300\,mm$. Indeed, PARMELA simulations (a multi-particle beam dynamics code from LANL [48]) confirm that a space-charge induced longitudinal broadening from $5\,ns$ to around $12.5\,ns$ can be expected at the given injection energy.
The simulation was repeated with disabled space-charge forces. In this second simulation, only two buckets were partly filled due to missing phase-synchronous beam injection. During further phase optimization it could be demonstrated that more than 93% of the accelerated charge is concentrated within a single bucket. Following this, no further phase improvements were attempted.

To measure the beam energy behind the RFQ/booster, two fast-current transformers acting as deuteron time-of-flight probes were brought back into operation. The first is located immediately behind the booster, whereas the second is placed after a distance of $l_d = 480 \pm 2.5\,mm$ inside a diagnostics chamber behind the first (small) quadrupole. Employing the measured drift time of $t_d = 24.55 \pm 0.1\,ns$ and the rest mass of deuterons m_d as well as

$$E[eV] = \frac{m_d \cdot c^2}{e} \left(\sqrt{\frac{1}{1 - \left(\frac{l_d}{t_d \cdot c}\right)^2}} - 1 \right) \tag{3.25}$$

a kinetic deuteron beam energy of $4.002 \pm 0.075\,MeV$ could be determined without booster operation.

Since the current transformer mounted in the exit flange of the LEBT is not capable of quantitatively measuring currents of DC beams (droop of $\frac{\%}{\mu s}$), it is not possible to measure the transmission through the RFQ, in order to review its operational status. However, a measurement that could be performed is the measurement of the beam current after the RFQ as function of the RFQ forward RF-power (at stable ion source operation). In regular operation, starting from a minimum power limit, the measured current should exhibit a strong rising slope before a plateau region is reached at around the nominal RF-power ($425\,kW$). Figure 3.37 shows the measured beam current plot, as well as simulation results[2] of the calculated transmission from the design phase of the accelerator. For this measurement, a spectrum analyzer was employed to measure the intensity of the $200\,MHz$ component of a TOF-probe reading (blue curve). Furthermore, the beam current at the target was measured employing a counter (red

[2]Private Communication - C. Franklyn, NECSA and A. Schempp, IAP Frankfurt

curve). The general behavior of the measured curves is in a good agreement with

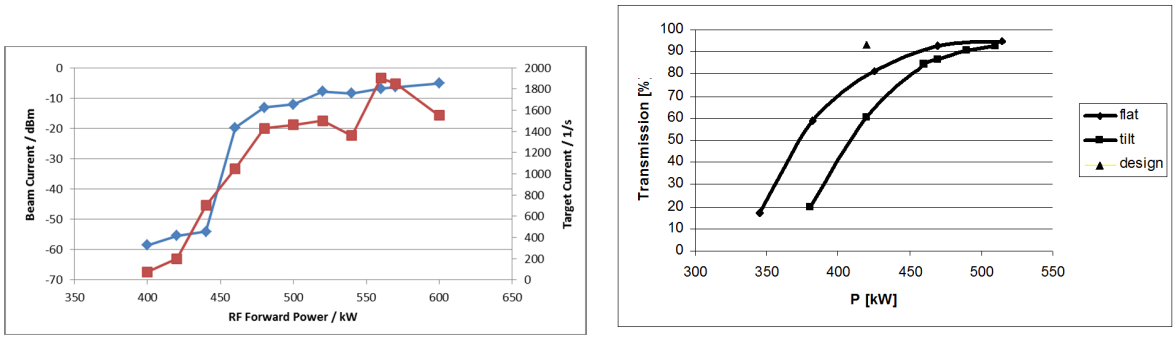

(a) (b)

Figure 3.37: (a) Measurement of the beam current (blue curve: TOF-Probe reading, red curve: target current) and (b) simulation of the transmission as function of RFQ forward RF-power

the simulated data. Nevertheless, the curve appears to be slightly shifted to higher forward power values. This might indicate a deterioration of the surface and thus a decrease in quality factor. Since the main amplifier tube is capable of delivering 1 MW of RF-power, this decrease can be compensated.

3.3.2 Performance Evaluation of spiral Booster

To survey the booster operation, the final deuteron beam energy with enabled booster could be measured employing the TOF probes. In figure 3.38a, the measured energy is plotted against the booster RF-Power. The deviation to the square root shape of the curve can be explained by the measurement accuracy. Figure 3.38b indicates the dependence of the final beam energy on booster RF phase angle shift, relative to the RFQ RF phase at 60 kW input power. It is clearly visible, that the booster is not operating according to specifications, since the maximum energy gain achieved was only 0.57 MeV and not the specified 1 MeV although the energy gain already seems to saturate at 60 kW input power. A possible reason could be the surface quality in the gap regions, since during booster operation, x-ray radiation was found close to the booster. Visual inspection of the surface of the 500 kV peak gap indicated deep scratches (compare figure 3.39) which lead to rather sharp edges. At these edges, electrons can be emitted due to the high local electric field. These electrons are accelerated and when hitting the surface of the positive electrode, they emit Bremsstrahlung. The electron acceleration draws energy from the resonance circuit and thus causes damping. The

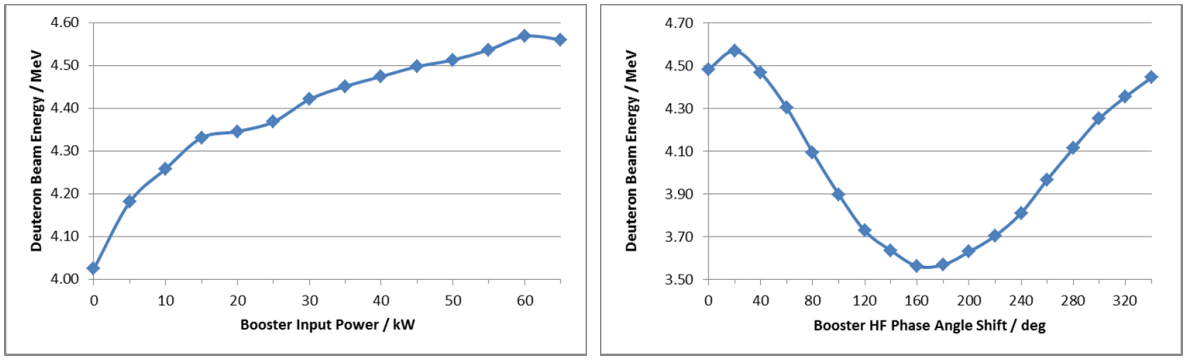

(a) (b)

Figure 3.38: Final deuteron beam energy against (a) booster input power (b) booster phase angle shift

energy and intensity of Bremsstrahlung can be used to estimate the energy dissipated by the resonance circuit.

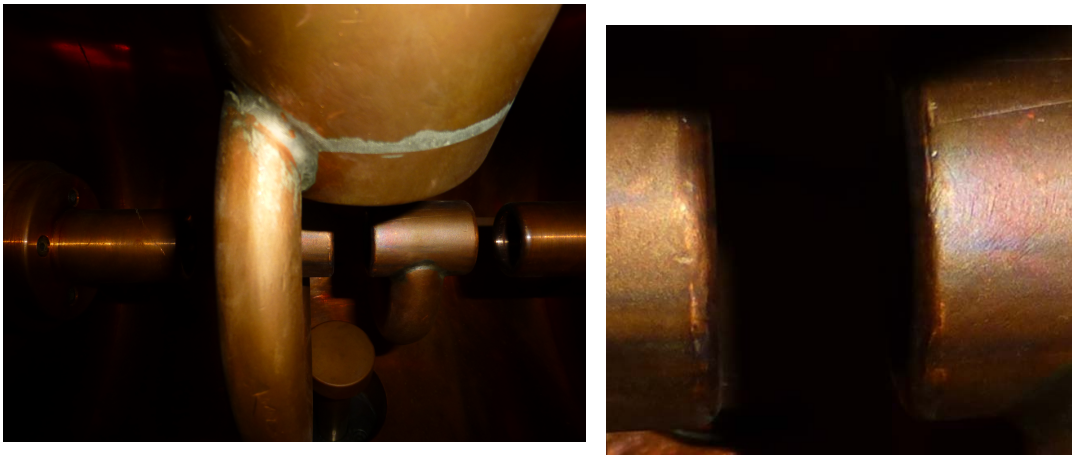

(a) (b)

Figure 3.39: Detailed view of the boosters central, 500 kV gap

3.3.3 HEBT Simulations and Measurements

To evaluate the beam focusing, a TRACE3D [37] model of the HEBT system was set up. The input twiss-parameters for RFQ operation without booster could be extracted from plots of Parmteq simulations performed by A. Schempp during the system design phase and can be found in table 3.3. These parameters as well as the relevant characteristics of the quadrupoles were employed to set up a TRACE3D

	x	y
ϵ / mm·mrad	17.29	19.95
α / -	3.80	9.43
β / mm/mrad	1.08	4.29
γ / mrad/mm	14.36	21.00

Table 3.3: Twiss-parameters of the DWIK accelerator

simulation scenario of the typical operation (see figure 3.40a). Since the vertical beam seems to be slightly over-focused, an optimized setup could be derived by lowering the current on the last two quadrupoles, which can be found in figure 3.40b.
To verify the emittances employed, quadrupole scans could be performed subsequently. In a quadrupole scan, the quadrupole current is ramped through the focal point while the beam width is measured behind the magnet employing a beam-profile-monitor. Afterwards, the emittance can be derived by fitting a parabolic function to the plot of beam width versus quadrupole strength: Approximating the transfer matrix [49] of the quadrupole employing a thin lens of focal length f, the field strength K is calculated to be $K = \frac{-1}{f}$ in combination with the drift length L between quadrupole magnet and monitor the combined matrix can be derived to be

$$\mathbf{R} = \mathbf{R}_{Drift} \cdot \mathbf{R}_{Quad} = \begin{pmatrix} 1 & L \\ 0 & 1 \end{pmatrix} \cdot \begin{pmatrix} 1 & 0 \\ K & 1 \end{pmatrix} = \begin{pmatrix} 1+LK & L \\ K & 1 \end{pmatrix} \tag{3.26}$$

If σ_I is the input beam distribution, the beam after the quadrupole and drift length σ_O can be derived via

$$\sigma_O = \mathbf{R}\sigma_I\mathbf{R}^T \tag{3.27}$$

Using algebra it can be found, that $\sigma_{O,11}$ is a parabolic function of the field strength K so it can be identified with a parabolic fit function $aK^2 - 2abK + ab^2 + c$ of the plotted data, where a, b and c are fit parameters.

$$\sigma_{O,11} = L^2\sigma_{I,11} \cdot K^2 + 2(L\sigma_{I,11} + L^2\sigma_{I,12}) \cdot K + L^2\sigma_{I,22} + \sigma_{I,11} \tag{3.28}$$

$$= aK^2 - 2abK + ab^2 + c \tag{3.29}$$

It can easily be shown that:

$$a = L^2\sigma_{I,11} \tag{3.30}$$

$$-2ab = 2(L\sigma_{I,11} + L^2\sigma_{I,12}) \tag{3.31}$$

$$ab^2 + c = L^2\sigma_{I,22} + \sigma_{I,11} \tag{3.32}$$

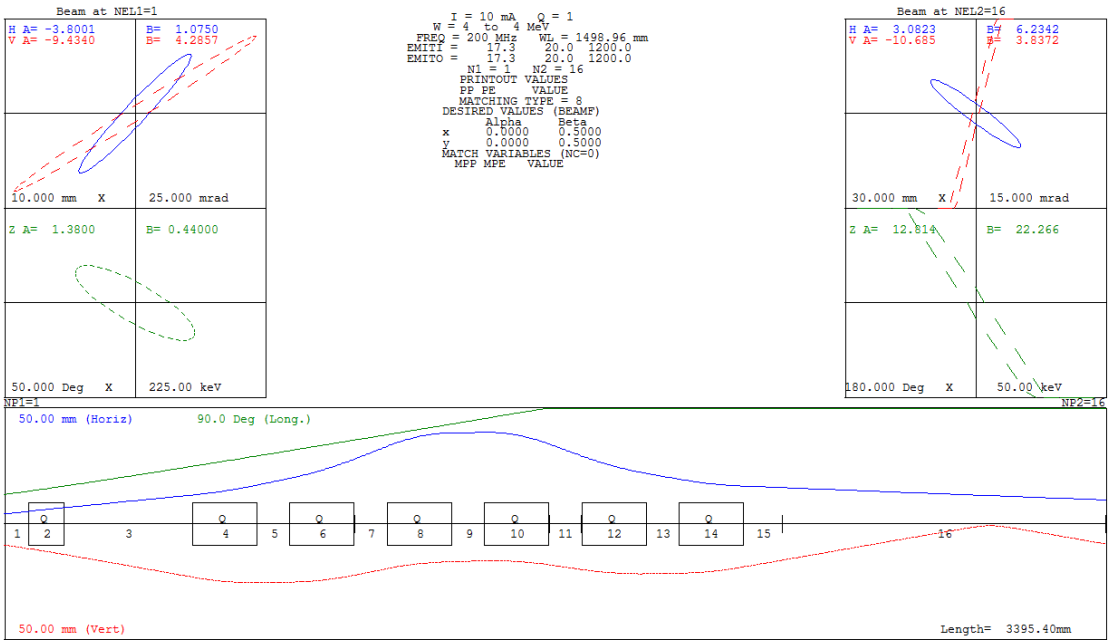

(a)

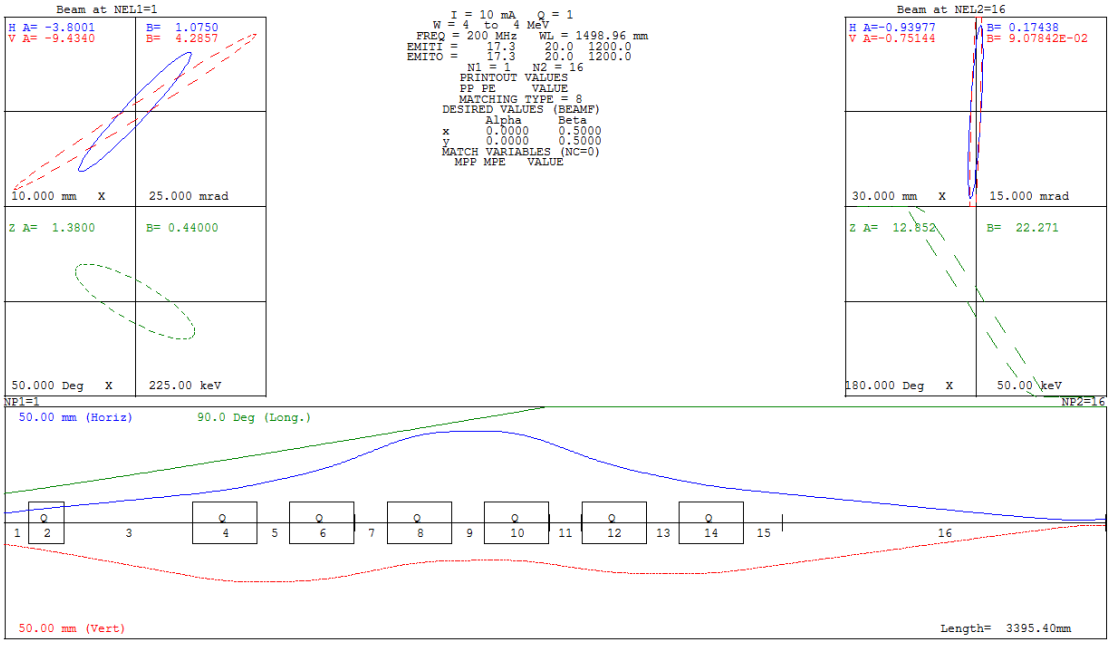

(b)

Figure 3.40: (a) Typical HEBT operation prior to simulations (b) optimized HEBT operation

Solving this equation system leads to the following expressions for the matrix components of σ_I

$$\sigma_{I,11} = \frac{a}{L^2} \tag{3.33}$$

$$\sigma_{I,12} = -\frac{a}{L^2}\left(\frac{1}{L} + b\right) \tag{3.34}$$

$$\sigma_{I,22} = \frac{1}{L^2}\left(ab^2 + c + \frac{2ab}{L} + \frac{a}{L^2}\right) \tag{3.35}$$

The emittance is derived by calculating the determinant of a beam distribution. In other words, the transversal beam emittances can be calculated from the fit parameters and the length of the drift as follows

$$\epsilon = \sqrt{\det \sigma_I} = \sqrt{\sigma_{I,11}\sigma_{I,22} - \sigma_{I,12}^2} = \frac{\sqrt{ac}}{L^2} \tag{3.36}$$

Since this derivation does not take into account space charge effects, beam currents below $1\,mA$ should be employed.
For quadrupole scan measurements at the DWIK accelerator, a deuteron beam current of around $500\,\mu A$ at an energy of $4\,MeV$ was employed. In a first measurement, $\epsilon_x = 15.95\,mm \cdot mrad$ could be determined employing quadrupole 5 while quadrupoles 6 and 7 were set at $I = 0\,A$. At a second measurement $\epsilon_y = 19.15\,mm \cdot mrad$ was determined employing quadrupole 2 with all following quadrupoles were set to $I = 0\,A$. Scans at quadrupole 4 and 6 failed, because their quadrupole strength was not sufficient to achieve a focus, due to the defocusing of the previous magnets. The result of the quadrupole scan is found to correspond to the theoretical data from the design of the RFQ.

Since the shortness of the deuteron pulse at the target (preferably less than $1\,ns$) is essential for reasonable neutron-energy resolution, the space-charge induced longitudinal bunch broadening behind the DWIK RFQ was investigated employing a CST Particle Studio simulation. The bunch length of a single bunch is only determined by the beam dynamics of the RFQ. An additional pulsing system only leads to single bunch injection.
In this Particle-in-Cell simulation, a $15\,ns$ long, $20\,mA$ DC beam was injected to the DWIK RFQ. In addition, the model included $2.5\,m$ of free drift-space. Due to longitudinal space-charge broadening during the path from the source to the beginning of the gentle buncher the duration of the input beam increased to $\sim 30\,ns$, which leads to a sequence of 8 bunches after the RFQ (6 regular bunches + 2 due to improper

phase angle). The duration of four of these bunches was analyzed at multiple distances to the end of the RFQ. The results of the can be found in figure 3.41. The bunch

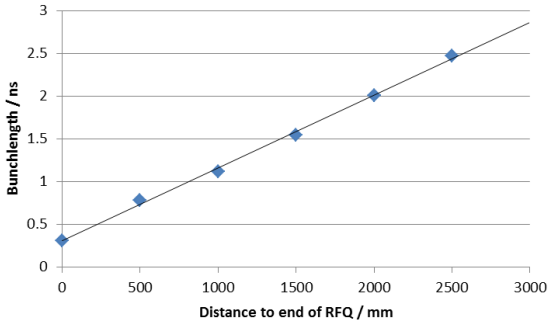

Figure 3.41: Simulation results of space-charge induced bunch broadening behind DWIK RFQ

length at the exit of the DWIK RFQ could be determined to be $0.31\,ns$ what verifies the design value of $0.38\,ns$. Furthermore, this result illustrates the need of a shorter HEBT. The original HEBT section exhibits a length of $3395\,mm$ measured from the end of the booster, whose length adds another $300\,mm$ to the total distance. This leads to a longitudinal pulse spread at the target of around $3.64\,ns$. Since on the one hand such a pulse length would lead to a bad energy resolution and on the other hand the neutron flight path of around $2\,m$ from the target to the detector would be rather short, the HEBT section had to be modified, to enable using the DWIK RFQ as a demonstrator for the ACCIS project.

In a first TRACE3D simulation, a reasonable setup could be determined employing only the small quadrupole as well as two large ones. The simulation result can be found in figure 3.42. In a later experiments it turned out that in addition to the rather large beam spot with an average diameter of $20\,mm$ an intense halo beam is present. Since the magnets were already operated at its maximum current, they had to be exchanged to different ones which permit a focusing gradient of up to $8.7\frac{T}{m}$. First simulations indicate a huge improvement in beam quality (see figure 3.43). The simulations indicate a reduction of beam diameter of approximately $5\,mm$ The modification of the HEBT is still ongoing so definitive experimental results are not yet available.

In the framework of this thesis, the DWIK accelerator could only be employed for target tests. But once required modifications like the upgrade of the HEBT and further improvements to the system to operate according to specifications (e.g. increase of duty cycle to nominal value) are implemented, the commissioning of the pulsed beam injection system (described in the following chapters) could be performed. In this case, the DWIK RFQ would be a perfect system to act as a demonstrator source for

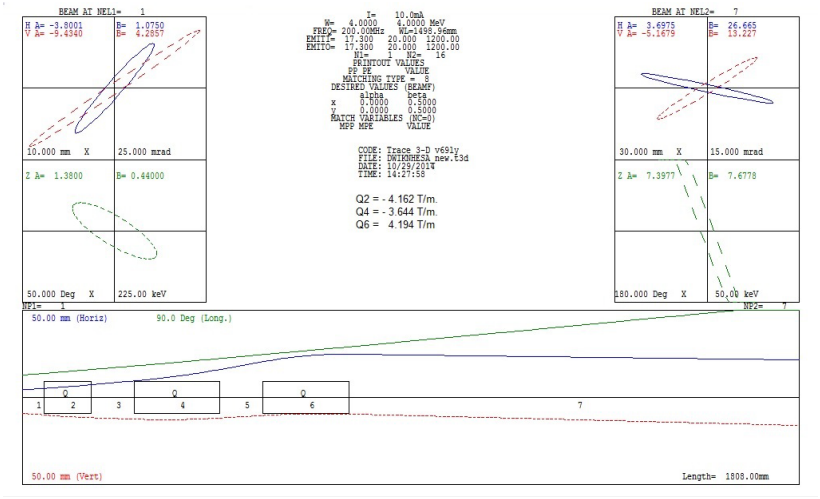

Figure 3.42: TRACE3D simulations of reduced HEBT

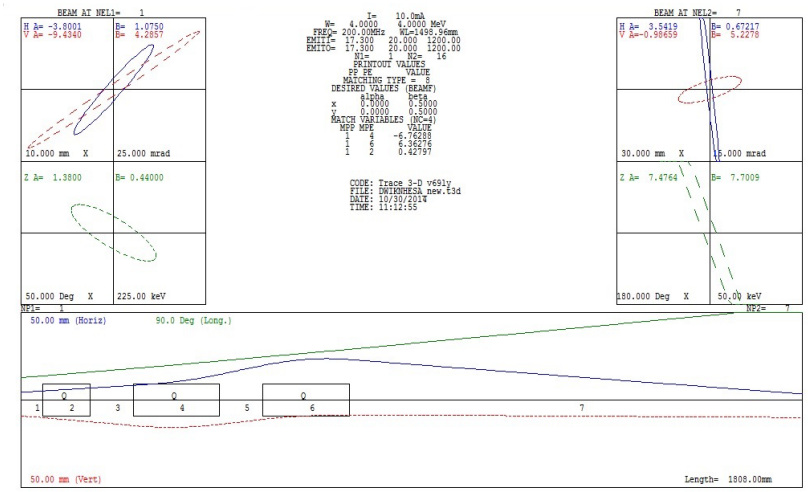

Figure 3.43: TRACE3D simulations of new HEBT employing stronger magnets

the ACCIS project.

4 Pulsing System - Theoretical Considerations

The time-of-flight (TOF) technique employed in the ACCIS detector systems requires a pulsed deuteron beam with a burst duration of around $1\,ns$ at the target and a repetition rate of around 3 MHz. Although an RFQ inherently produces a bunched particle beam, the pulse repetition rate is governed by the operating frequency, which is typically between $80\,MHz$ and $200\,MHz$. These rates are too high (by a factor of $\sim 25- \sim 65$) to permit unambiguous experimental assignments of energy to neutron events in the appropriate energy-interval (see chapter 2.3), since a fast neutron from a later burst can have the same time-of-flight as slower neutrons from an earlier one. The solution to this problem is to impose the desired pulse structure on the beam either before the particles enter the RFQ structure or after the acceleration.

There are several issues in selecting the first option: If the beam is chopped in any way, the dumped fast energy beam induced three orders of magnitude more heat to the structure than a low energy beam. For a deuteron beam in the MeV energy regime, the cross-section for neutron production due to deuteron beam self implantation employing the nuclear reaction $D(d,n)^3He$ is around two orders of magnitude higher than in the keV energy regime. From the technical point of view, due to the velocity difference of the deuterons, a beam impact (e.g. deflection) to a keV energy beam can be achieved in a much more compact and power efficient design compared to an MeV beam. As an example, the beam chopper for the Spallation Neutron Source (SNS) at Oak Ridge National Lab (positioned in the HEBT of the linac), which is able to apply 1-MHz-pulsing to a 2.5 MeV beam, has a length of 35 cm [50].

An other concept of bunching an MeV beam which is due to be employed at the FRANZ accelerator of the University of Frankfurt is the use of a bunch compressor after the acceleration stage. It is planned to match up to eight bunches from the RFQ to one single bunch employing a deflection system and eight different flight paths through a magnet with different path lengths for each flight path. During the design phase simulations indicated that small re-buncher elements are necessary in each flight path [51]. This bunch compressor is not in operation yet.

For the ACCIS project, it was decided to apply the pulsing system in the LEBT to fill only a single bucket of the ACCIS RFQ RF. During this work, a similar approach was published by R. Hamm, who placed deflector plates just in front of the radial matching section inside the RFQ tank to induce single bunch injection making use of the limited acceptance angle of the RFQ [52]. The main difference between these two approaches is the beam current and the duty cycle of both systems. Whereas the system presented here is aiming for continuous wave operation employing a bunch charge of $200\,pC$ at a repetition rate of $3\,MHz$, the system by R.Hamm is intended to act as a injector to a Dielectric Wall Accelerator (DWA). For this application the approach is feasible, since only low bunch charges of 3 to $30\,pC$ at low repetition rates of up to $10\,Hz$ are required. Thus, the main fraction of the input beam is allowed to be dumped into the RFQ entrance region. The low duty cycle is essential for the vacuum to recover.
In the following section, the design considerations for the ACCIS pulsed beam injection system (PBIS) are presented.

4.1 Basic Concepts

There are two different approaches to produce a pulsed beam out of a continuous beam: The continuous beam can be either chopped or bunched. Employing chopping methods, the unwanted parts of the beam are dumped. So the resulting beam exhibits the wanted pulse structure. Although this method is rather simple to utilize (e.g. electrical deflection plates or electromagnets for beam deflection) the unwanted deuteron beam can cause secondary effects like heating of structures or even neutron production, where the deuteron beam is dumped. The magnitude of the neutron background due to the dumped beam depends on the ratio between transmitted and dumped beam.
The second approach to pulse a beam is bunching. In a bunching system, a RF is employed to either accelerate or decelerate particles relative to the phase of the RF. Figure 4.1a illustrates RF-bunching employing a drift tube framed by a ground aperture at both sides. When a pre-bunched (or DC) positively charged ion beam is entering the first gap at the correct phasing, the ions ahead of the bunch center are decelerated, while the subsequent ions are accelerated. The longitudinal focus can be adjusted by the amplitude of the RF input. The process of bunching can be illustrated employing longitudinal phase-space plots energy spread ΔE over phase length Φ (see figure 4.1b): Here, the phase-space ellipse is tilted by the buncher. At the bunching

focus, the energy spread is at maximum, whereas the phase length is at the minimum. The length of the drift tube plus the length of the first gap has to be an odd multiple of exactly half of the period of the buncher RF frequency in terms of the ions average velocity. The disadvantage of a bunching system is the induced energy spread of the bunch which is proportional to the bunching strength. If the phasing of a bunching system is shifted by exactly 180°, the resulting element is called de-buncher. A de-buncher can be used to decrease the energy spread induced by a bunching system since it accelerates the previously decelerated ions and vice versa. The application of a bunching system is limited, since in most of the applications the energy spread has to be small.

To compensate for the disadvantages from both methods, a combined setup is used

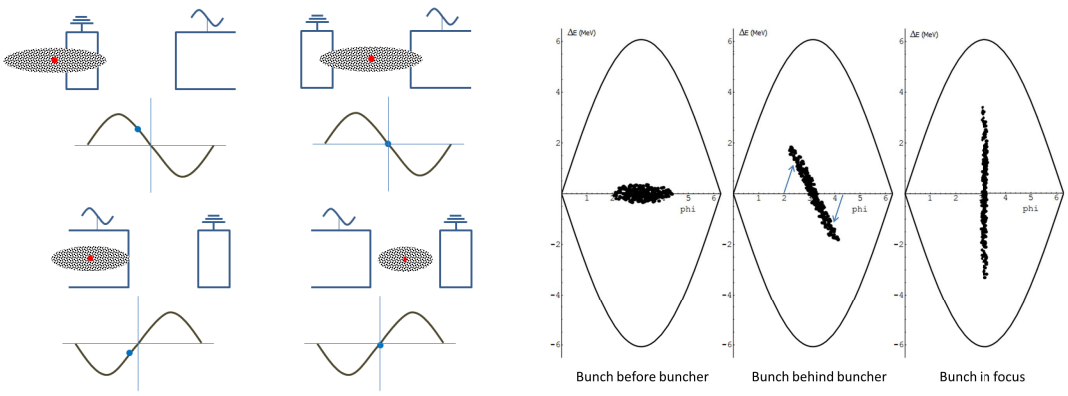

(a) (b)

Figure 4.1: (a) Principle of a two gap, one drift tube bunching system (particles in bunch positively charged) (b) longitudinal phase-space plots of bunching process [53]

in the ACCIS pulsing system: Since the prototype pulsing system was planned to be tested at the DWIK RFQ at Necsa which has a duty factor of up to 20%, a low frequency pre-pulsing can be applied even at the source. This will decrease the thermal and gas load to the following chopper elements. Thereby, up to $2\,ms$ long macro-pulses with a repetition rate of $20-100\,Hz$, respectively are generated. In a second step, the ion beam will be chopped by sweeping it over an aperture at ground potential utilizing an RF driven deflector, to induce a micro-pulsing of $10-20\,ns$ long beam pulses with a repetition rate of $3\,MHz$. In the last step, a buncher will compress the relatively long pulses to fit into a single bucket of the RFQ which is $5\,ns$ long in the case of the DWIK RFQ (or $10\,ns$ in the case of the ACCIS RFQ). Since longitudinal focusing of the ion beam in an RFQ starts only in the beginning of the gentle buncher section, the

focus of the buncher in the pulsing system has to be set at this point (after $\approx 25\,cm$ of ion travel within the DWIK RFQ) to avoid longitudinal broadening of the pulse due to space-charge effects.
For an effective deflection, the beam should constitute a waist between the deflector plates. Thus, an einzel lens is employed in front of the deflector. Since the sweeping induces transversal momentum components to the beam, a collimator is utilized to remove the most divergent parts of the beam. To obtain the transversal beam focus, the collimator also acts as an einzel lens. To enable transversal focusing of the ion bunch into the radial matching section of the RFQ, an other einzel lens is employed at the end of the beam optics chain of the pulsing system. A schematic drawing of the pulsing system can be found in figure 4.2

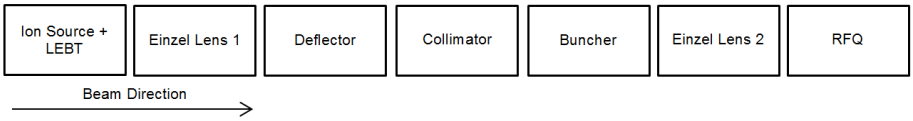

Figure 4.2: Schematic drawing of the pulsing system

4.2 Single Component Design of Pulsing System

In the following section, the detailed simulation and design work of the pulsing system employing CST Particle Studio is presented. Prior to the simulations, the required beam current had to be estimated. As explained in chapter 3.2, the ACCIS RFQ is designed to operate with an input beam current of $20\,mA$ (see table 3.2), since an entirely filled bucket at this DC input beam would lead to the required total bunch charge of $200\,pC$. For the design of the pulser system, another condition had to be taken into account. The pulsing system was planned to be tested at the DWIK RFQ presented in chapter 3.3, which is operated at a frequency of $200\,MHz$. The higher frequency leads to a shorter bucket, what implies that a higher input beam current (in this case $40\,mA$) is necessary to achieve the required bunch charge.
In the pulsing system, aside from the deflector based chopper, a buncher is included. Due to the longitudinal focusing of the buncher, less beam current is required (less than half of the beam current according to simulations in section 4.2.4) to achieve the required bunch charge. Since the pulsing system has to operate at the ACCIS as well as the DWIK RFQ concerning specifications, the decision was made to employ a $30\,mA$ beam (average of both cases) as a basis for the design work. The input beam shape for the simulations was based on the DWIK RFQ input beam shape.

To keep the system compact and thus reduce the impact of space-charge to beam broadening, electrostatic elements instead of magnetic elements are employed. Here, the preferred optics element is an einzel lens. An einzel lens consists of a three-tube or three aperture system, where the first and the last tube/aperture are at ground potential whereas the intermediate tube/aperture is either on positive or negative high potential (typically set to several $10\,kV$). A schematic view of an einzel lens can be found in figure 4.3.

An einzel lens always consists of two gaps with the same average electric field, but one

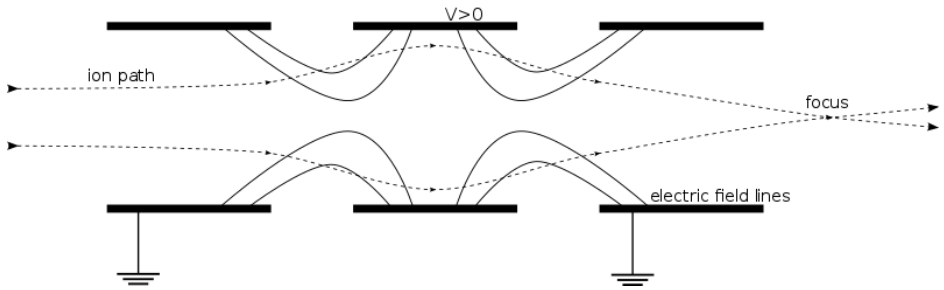

Figure 4.3: Schematic drawing of a decelerating einzel lens [54]

is accelerating the other decelerating. The decelerating field is defocussing whereas the accelerating field has a focussing effect. Since the focussing strength is proportional to the distance to the beam axis, the net effect is always focussing. The change in energy for a particle traversing both gaps is always 0. An einzel lens with a decelerating field in the first gap is called decelerating einzel lens. For a decelerating einzel lens, the applied voltage has to be lower than the beam energy, otherwise the beam is stopped and reflected. As described in the following section, all focusing elements consist of different einzel lenses.

4.2.1 Einzel Lens 1

During this optimization, it was attempted to reasonably focus the beam from the ion source on the end of the deflector plates. However, a strongly focused beam introduces particles with unintentionally-increased transversal velocity components that will be amplified due to the deflection process. Therefore, a parallel beam with a small diameter or at least a focused beam with a far-off focal point are the preferred results for this optimization step. In the first step of the optimization process, a decision was made on an accelerating lens, as it produces a much more parallel beam than a decelerating einzel lens, although the latter requires lower voltages (for a $10\,mA$ deuteron beam, an accelerating lens would require up to $-40\,kV$, while employing a decelerating lens

already at 19 kV would lead to reasonable results). Furthermore, the accelerating lens can easily be scaled up to higher beam currents, as the accelerating voltage is only limited by high-voltage stability compared to the decelerating one, which is limited according to the beam energy.
In a second optimization step, the length of the gaps were varied. Best focusing could be obtained at gap lengths of 9 mm for the first and 8 mm for the second gap. Therefore, the only three parameters left to optimize have been the lens length, diameter and voltage. As the voltage is an easily modifiable parameter, so it was tried to first fix the length and diameter to afterwards fine tune the setup by optimizing the voltage. Moreover, it was attempted to find an optimal setup, which can be operated at each beam current between 10 and 30 mA, just by adjusting the voltage. This optimal setup was found, by starting with a tube of 15 mm in diameter and 20 mm long. Afterwards, the diameter was on both ends iteratively reduced and the voltage iteratively adjusted, such that the beam was almost-touching the inner tube. To achieve the required focused beam diameter, the tube length was reduced and the previous step was repeated. In the final setup, the central tube of the einzel lens has a length of 7.5 mm. The inner part of the tube is cone-shaped, with a decreasing diameter from 10 to 9 mm. The aperture of the first tube is set to be 14 mm in diameter. Furthermore the third tube has a length of 5 mm and an inner diameter of 9 mm. The voltages applied to the central tube are $-60\,kV$ for a 30 mA input beam (see figure 4.4). This leads to a maximum field strength across the gaps of 6.66 $\frac{kV}{mm}$ which is well below the break-down field strength in vacuum of $15 - 40\,\frac{kV}{mm}$ [55]. Thus, these required voltages can be realized.

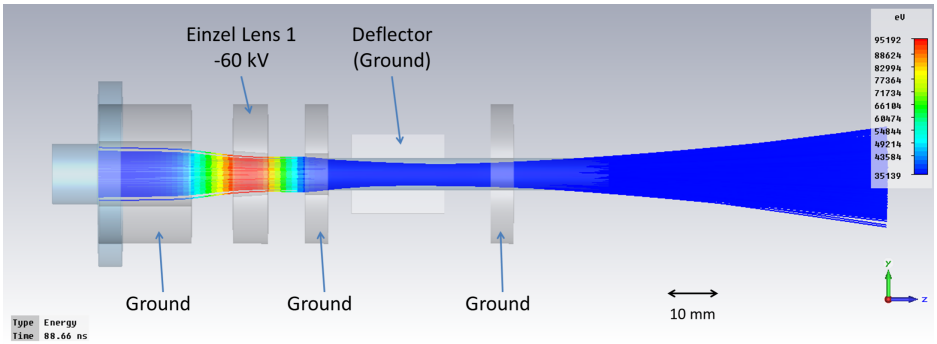

Figure 4.4: Final simulation (CST Particle Studio, tracking solver) of Einzel Lens 1 employing a 30 mA beam

4.2.2 Deflector

In the first design, it was envisaged to apply a continuous, sinusoidal radio-frequency to the deflector. In this case, a narrow phase interval with the zero-crossing of the frequency at its center would correspond to transmission of the ion beam. During the rest of the RF phase, the ion beam would be dumped.
The principal goal of the deflector optimization is to find a trade-off between the shortness of the transmitted particle bunch and the number of particles/amount of charge inside the bunch. The chief parameter connected with this trade-off is the deflection momentum, in other words the transversal momentum applied to the particles during the zero-crossing of the RF applied to the deflector plates. Obviously, this momentum depends on the electric field between the deflector plates, which is related to the plate-to-plate distance and the peak voltage, as well as the effective path length through the plates. As a side aspect, the peak voltage should be kept minimal, due to the fact that a lower voltage is easier to handle with respect to the RF-pulsing electronics. Since peak voltage is the parameter easiest to modify, its geometrical parameters were optimized in the first step. In this context, the distance between the deflector plates should be kept minimal with respect to voltage requirements but also as large as possible concerning vacuum quality deterioration due to dumped beam. As a compromise, a plate distance of $7\,mm$ was selected. Since the expected beam is almost parallel in nature, it does not make sense to orient the deflector plates at an angle to the beam direction. Such an angle might only be helpful if the beam is strongly focused on the exit end of the deflector and thus minimizes the distance between plates and particle beam over the entire effective length. Consequently, the sole selectable geometrical parameter is the effective length of the deflector plates.
As deflection efficiency is proportional to peak voltage as well as to effective length, a reduction of effective length must be compensated by an increase in peak voltage, to keep the resulting bunch as short as required. Therefore, a decrease of the effective length only makes sense if the focal point of the previous einzel lens is too close to the deflector entrance. On the other hand, longer deflector plates will lead to an increase of charge deposition on the plates during the non-transmission phase. This might be an issue of concern, as the effectiveness of the vacuum pumping might be reduced between the deflector plates and thus an accumulation of charge could lead to high-voltage sparks. To reduce this effect -but simultaneously keep the transversal bunch momenta low- an aperture was added behind the deflector plates, where a major fraction of the deflected beam can be deposited.
Employing this aperture, two approaches appear to be possible: The first approach

employs a strong electric field acting as a strong lever with a short deflector-to-aperture distance; the second approach employs a weaker electric field acting as a weak lever with a long deflector-to-aperture distance. However, the main problem with the second approach are defocussing space-charge effects, especially at higher beam currents: To achieve transmission of a reasonable amount of particles, the deflection velocity needs to be quite low. On the other hand, the distance between deflector and aperture has to be quite long, in order to get mainly transmission of particles with low transversal momentum. But at such a long distance, defocussing space-charge effects are no longer negligible. Therefore, the first option was selected for the final pulsing system. The gap between the deflector plates and the aperture was set to be $10\,mm$, which will still assure reasonable pumping efficiency in this section.
In a parameter study, where the deflector length and the applied voltage were varied and the resulting bunch length and integrated bunch current were determined, the optimal setup was determined to be $20\,mm$ in length at $20\,kV$ applied peak-voltage. This setup leads to an ion beam transmission through the aperture during a phase interval of the deflecting RF-cycle in which its voltage is is in the regime of $\pm 3.5\,kV$. To operate the deflector, two different voltage settings are possible: In the symmetric operation mode, the zero potential is always located in the center between the plates and RF-power of same amplitude but 180 deg phase shifted is applied to both plates. The second mode is asymmetric operation which means that one plate is maintained at ground potential, whereas RF-power is applied only to the second plate (see figure 4.5). These two different approaches have been simulated employing CST Microwave

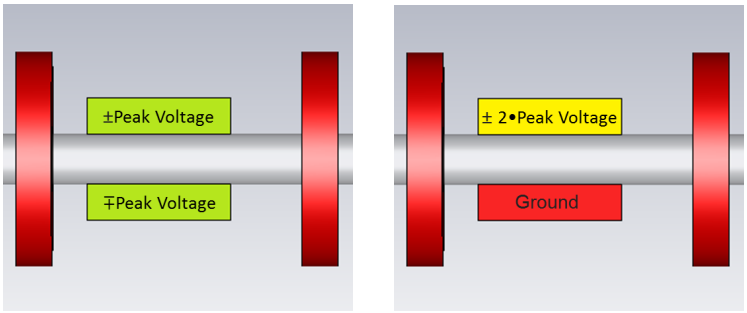

(a) (b)

Figure 4.5: Possible pulsing regimes:(a) Symmetric operation mode: RF to both plates pulsing (b) Asymmetric operation mode: RF to one plate, the other to ground

Studio, with a peak voltage of $10\,kV$. The resulting output pulses after the first aperture are shown in 4.6.

Although the pulse shape in both cases is similar, the average beam energy in the

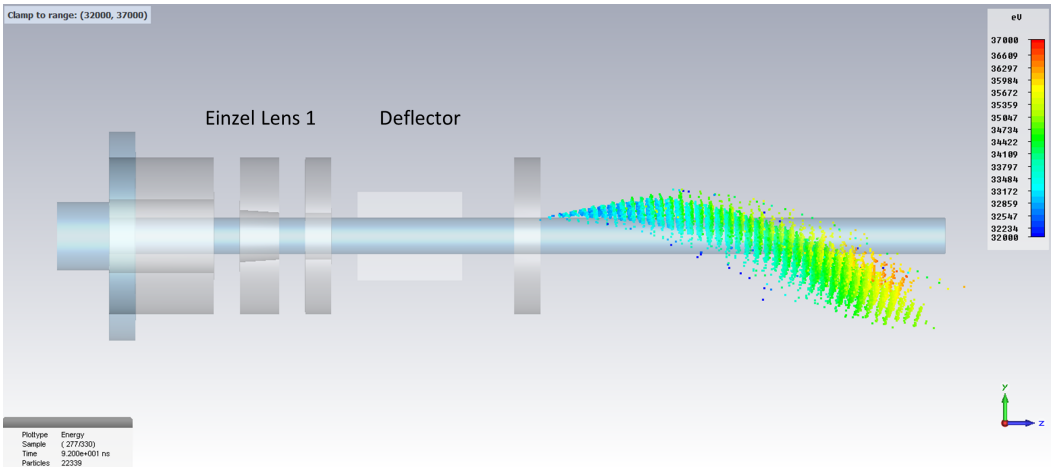

(a)

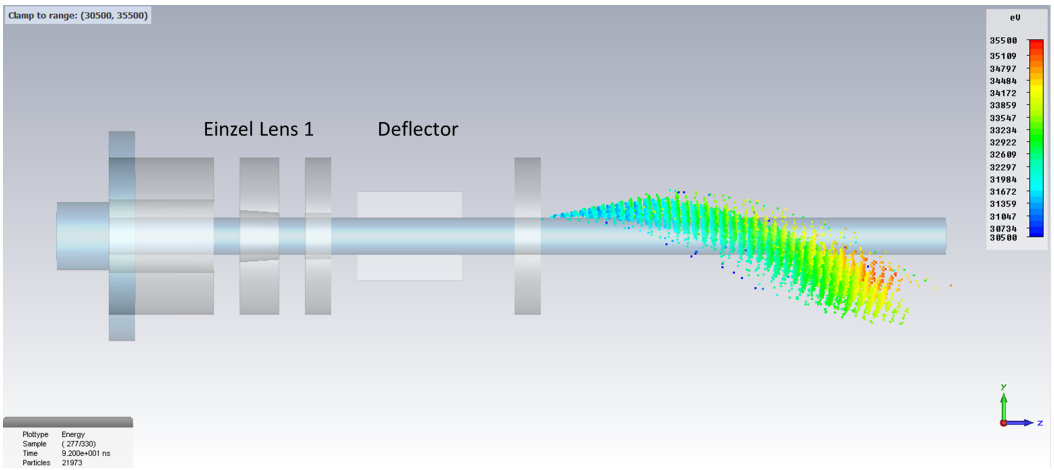

(b)

Figure 4.6: Results of the CST deflector simulations (a) symmetric pulsing (b) asymmetric pulsing

asymmetric case is shifted to a lower energy by approx. $2\,keV$, due to the different longitudinal field distribution in the gaps while the beam is passing by. If required, this shift in average energy could be compensated by a higher injection energy at the beginning of the pulsing system. The energy spread without collimator is stable at about $\pm 2 - 2.5\,keV$ in both cases.

Both electrical configurations can be used with the mechanical design presented. For sinusoidal high-voltage the symmetric approach should be employed whereas for pulsed high-voltage the asymmetric approach is preferred since only a single high-voltage pulser is required. Employing two individual pulsers for both plates would require synchronization between them.

4.2.3 Collimator

As explained in the last section, the deflector imparts transversal momentum to the transmitted particles, which causes a divergence of the beam as well as a spread in energy in the longitudinal direction. Moreover, since the divergence is also not symmetrical with respect to the beam axis, the beam can barely be focused. Nevertheless, the beam intensity is highest in the center and drops to zero towards the edges of the pulse, where the transverse momenta are largest. So it would seem advantageous to suppress these edges of the pulse, as they could cause a spill-over to neighboring RFQ beam-buckets. Both of these issues can be resolved by means of a collimator-type element.

For this collimator design, two different approaches were tested. In the first attempt, a simple block-type collimator (in other words a massive, 50 mm long tube) was employed to absorb particles with large transversal momenta. This setup can be seen in figure 4.7. The color code indicates the particle energy.

Although this collimator gives rise to a reasonable bunch parallel to the beam axis,

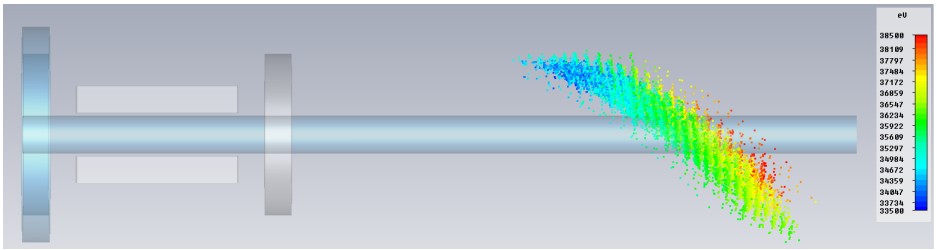

(a)

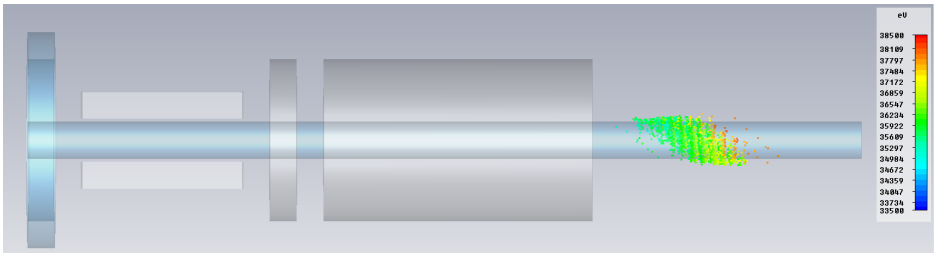

(b)

Figure 4.7: Comparison of a bunch (a) without and (b) with the simple collimator (color code indicates particle energy from blue 33.5 keV to red 38.5 keV)

too many particles are absorbed during the collimation process (in the simulation of figure 4.7, 70 % of the particles were absorbed). In addition, the particles deposited inside the long collimator tube will dramatically deteriorate the local vacuum quality due to the geometry. Thus, the collimator had to be redesigned in such a way, that the beam is less collimated, but in addition, is also focused. So the long tube was replaced

by a shorter lens in combination with an aperture placed after a drift gap, which acts similar to the block-type collimator. The length reduction of the collimator tube will also minimize the vacuum-related issues.
A parameter optimization, similar to the optimization of einzel lens 1 was performed. As an optimization result, a tube-type lens with a length of $10\,mm$ and an inner diameter of $7\,mm$ could be determined, focusing the $30\,mA$ beam into the buncher at an applied voltage of $-65\,kV$. The optimal length of the gaps could be determined to be $9\,mm$. The final design of the collimator is shown in figure 4.8.

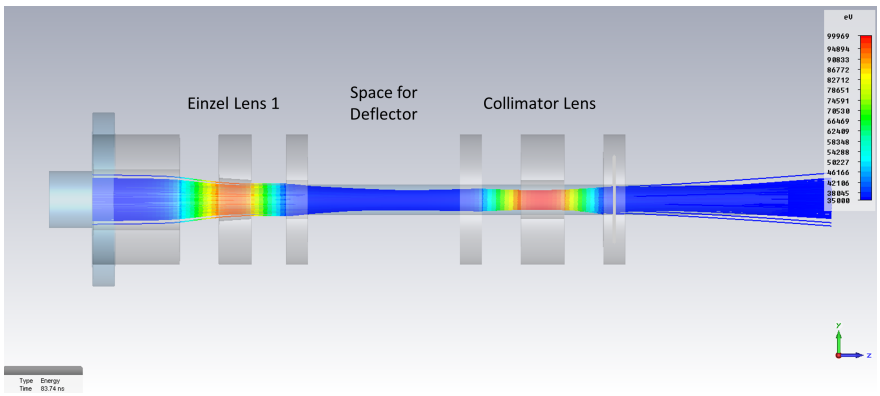

Figure 4.8: Shape of beam after the final optimization of the collimator lens employing Tracking Solver

4.2.4 Buncher

As described in the introduction, a simple beam chopping will not be sufficient to achieve single bunch injection to the RFQ due to the space-charge induced longitudinal bunch broadening. Thus, as simulations exhibit (see figure 4.9), the chopped beam (employed beam had a DC input beam current of $20\,mA$ without energy spread) would have to be shorter than $0.5\,ns$ to fit into a DWIK RFQ bucket (bucket length of $5\,ns$ at operating frequency of $200\,MHz$) or shorter than $1\,ns$ for the case of the ACCIS RFQ (bucket length of $10\,ns$ at operating frequency of $100\,MHz$), to compensate for the space charge induced longitudinal bunch broadening of a factor of 10 at the flight path to the gentile buncher of the RFQ.

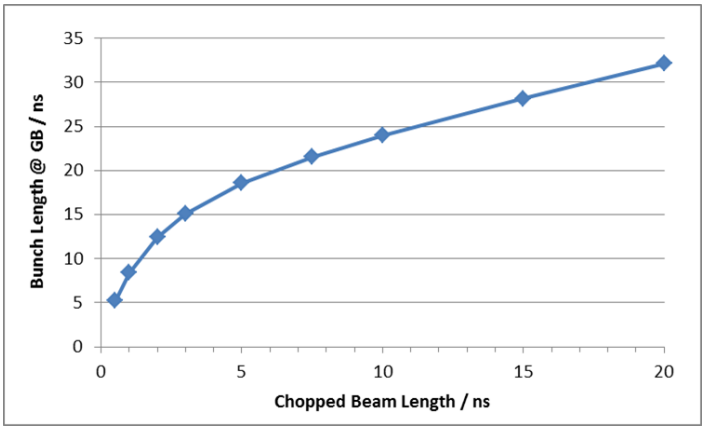

Figure 4.9: Simulation of longitudinal beam broadening from pulsing system to start of gentle buncher

Therefore, a buncher is applied in the pulsing system, which focuses the beam longitudinally at the entrance to the gentle-buncher section of the RFQ and, as mentioned above, this also permits reducing the required current from the ion source as well as permits selecting longer segments of the beam by the beam chopper.
To investigate, if a two-gap, tube-style buncher is sufficient to achieve the desired bunching, PARMELA simulations were performed again employing a $20\,mA$ beam, to determine the operational limits of such a two-gap buncher. Since simple RF-gaps cannot be implemented in a PARMELA simulation, a resonant cavity at the buncher frequency of $20\,MHz$ was modeled in Superfish, in order to obtain electric fields comparable to the acceleration gaps of the buncher. To select the correct phase for the bunching gaps, parameter studies for the phase angles of the two bunching gaps were performed to determine the phase angles that does not induce a change in average particle energy. Previous CST Microwave Studio simulations of the entire pulsing system indicate an energy spread of the chopped and collimated beam of around $\pm 2000\,eV$ ahead of the buncher. For this purpose, three different energy spread distributions were taken into account: in the first case, the situation without any energy spread was analyzed, to permit obtaining the influence of the energy spread. The second case considers a spatially homogeneous energy spread, whereas, in the third case, a more realistic model of longitudinally increasing ΔE is taken into account. Since, for the chopping, the zero-crossing of the RF frequency is employed, the gap between the plates and the ground lens acts either to accelerate or decelerate the ion beam. This introduces a time dependence in the energy spread. Figure 4.10 illustrates the energy spread distributions of cases 2 and 3.

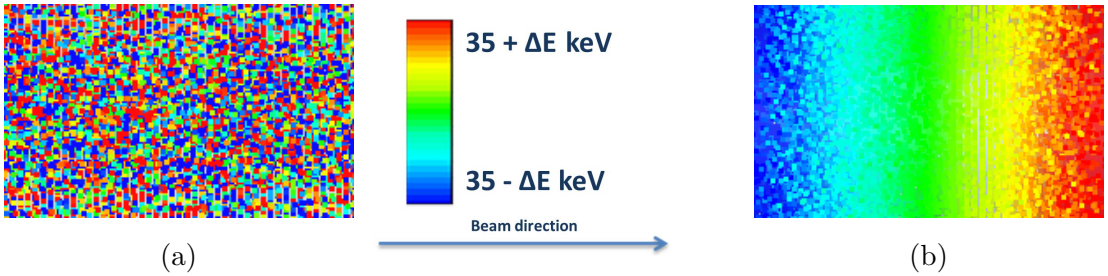

(a) (b)

Figure 4.10: Schematic view of two different energy spread ($\Delta E = 2\,keV$) options: (a) homogeneous energy distribution and (b) a more realistic distribution in which the beam energy increases towards the front end of the beam bunch

In the following parameter study, the applied bunching voltage was varied between 0 and $6\,kV$, to determine the necessary value for an optimal longitudinal focus at a distance of $25\,cm$ behind the buncher at which approximately the gentle buncher section of the DWIK RFQ begins. The optimal focus was obtained to be between $3 - 5\,kV$ peak voltage dependent on the input particle distribution. Figure 4.11a shows the results of the optimal focus determination for a $20\,mA$, $10\,ns$ bunch with an energy spread $\Delta E = 2\,keV$ in the homogeneous distribution. The results of the entire set of simulations for different bunch lengths and energy spread distributions can be found in figure 4.11b.

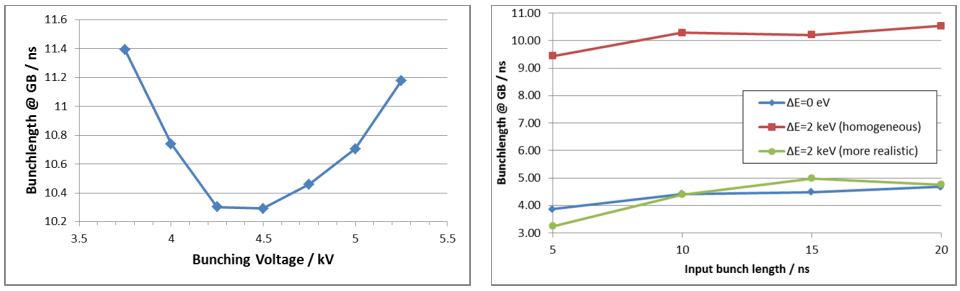

(a) (b)

Figure 4.11: (a) example for bunching focus determination (20 mA, 10 ns bunch with energy spread $\Delta E = 2keV$ for the homogeneous distribution and (b) results of the buncher simulation of all three cases for the energy spread

As the results indicate, a reasonable longitudinal focus (bunch length $< 5\,ns$) at the beginning of the gentle buncher is achievable in the ideal case if there is no energy spread (blue curve). If an energy spread of $\pm 2\,keV$ is homogeneously distributed over the entire bunch (red curve), the desired focus can not be achieved. Fortunately, the deflector introduces a longitudinal energy spread distribution, which supports the

bunching process. Such a distribution is employed in case three (green curve) and leads to a result comparable to an ideal bunch with no energy spread. Obviously, the distribution of case three is still better than what can be expected in the experiment, so the real bunching result is expected to be worse than case 3, but better than case 2. Thus, a single bunch injection is possible employing the ACCIS RFQ, but might be hardly achievable at the DWIK RFQ.

The geometrical parameters of the buncher could be determined as follows during parameter studies employing CST Microwave Studio: The entire structure has an inner diameter of 14 mm, whereas the gap-size is 5 mm each. For the buncher, an operational frequency of 20 MHz was selected, since this frequency can be produced by dividing the RFQ frequency either by the integer 5 (ACCIS RFQ) or by 10 (DWIK RFQ). To calculate the tube length, the particle velocity needs to be taken into account. To achieve the optimal bunching performance, the zero-crossing of the RF must occur when the center of the bunch is in the middle of the two-gap, tube-style buncher. The ion energy of 35 keV deuterons leads to a velocity of around 1.83 $\frac{mm}{ns}$. Employing half of the buncher period of 25 ns (since the second gap exhibits inverse potentials) and taking into account the gap length, a drift tube length of 40.79 mm was determined, to keep the bunch in a field-free region between the two bunching gaps. Behind the second gap, another grounded aperture with a length of 5 mm and an inner diameter of 14 mm was added to separate the high potential of the following lens from the RF voltage of the buncher. The result (optimized beam pulse) of the buncher can be found in figure 4.12

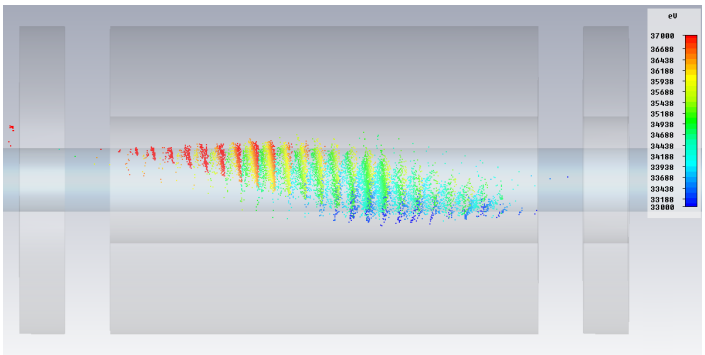

Figure 4.12: Shape of a beam pulse (inside the buncher after first bunching gap) obtained after optimization using PARMELA. The color code indicates the particle energy in keV from blue (low energy) to red (high energy). The visible micro-buckets come from sampling artifacts due to simulation binning.

4.2.5 Einzel Lens 2

Behind the buncher, the transversal focusing deteriorates due to space-charge forces. Furthermore, the RFQ has an entrance section where the beam drifts without any transversal focusing until the actual rod/vane structure is reached and where quadrupole focusing begins. Therefore, another einzel lens in front of the RFQ is necessary to maintain a reasonable transversal focus.
The design process of the second einzel lens is similar to that of the first einzel lens. The main difference is the greater distance of the focal point: whereas the focal point of the first lens was just at the exit of the deflector at 16.75 mm distance to the center of the lens, einzel lens 2 needs to focus the beam into the entrance section of the rod/vane structure at approximately 60 mm distance to the center of this lens.
By varying lens parameters such as gap distances, lens length, diameter and voltage, an optimal setting could be found at 8.5 mm for the first gap length and 6.5 mm for the second. Furthermore, an inner diameter of 23 mm and a tube length of 25 mm were chosen, since this lens could not be designed employing an accelerating lens: a reasonable focus with an accelerating lens could only obtained at voltages higher than $-80\,kV$, which is undesirable due to the danger of high-voltage discharges. An optimized decelerating voltage could be found at 27 kV, as figure 4.13 illustrates.

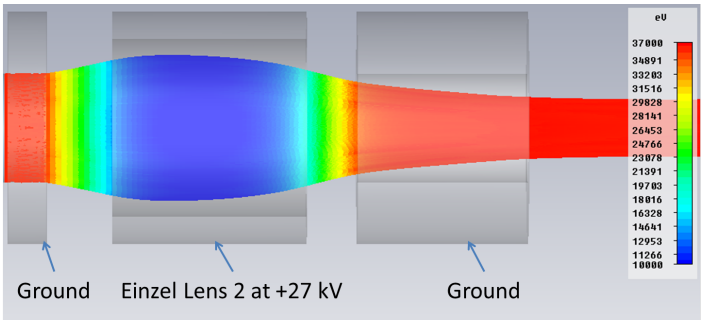

Figure 4.13: Results of beam transport simulations to optimize the second einzel lens. The colored section represents the beam and its energy distribution.

4.3 Final Simulation of Pulsing System

In a final CST Particle Studio simulation employing the Particles-in-cell (PIC) solver, the operation of the full pulsing system based on the final manufacturing design was evaluated. For this purpose, a 30 mA, 35 keV deuteron beam was emitted by a convex surface with a diameter of 10 mm on the beam axis at a distance of 46 mm in front of the first ground lens, simulating a converging input beam (as in figure 4.14), since

the pulsing system will be located between an LEBT employing einzel lenses and the RFQ.

The beam is focused into the deflector employing a focusing voltage of $-60\,kV$ at

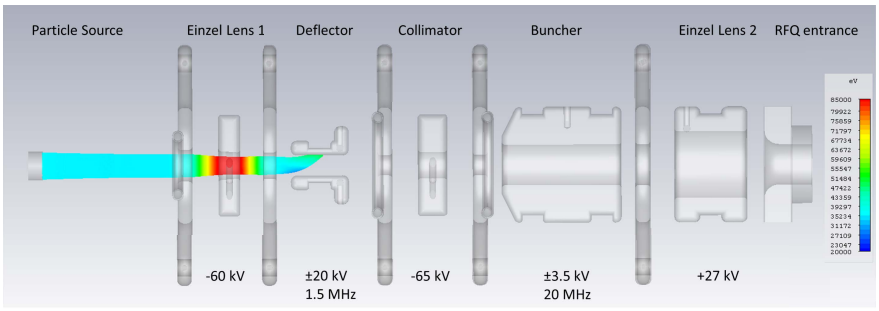

Figure 4.14: Results of simulations of deuteron beam transport in the beam injection region of the pulsing system. The color code indicates deuteron energy from blue ($20\,keV$) to red ($85\,keV$)

the first einzel lens. The deflector is operated with a sinusoidal RF at a peak voltage of $\pm 20\,kV$ at $1.5\,MHz$. During this design stage, operation with sinusoidal voltage instead of a high-voltage square-pulses was preferred. The change of this concept at a later stage due to practical considerations and availability of recent pulser technology will not alter the optimized beam parameters, because it affects only those fractions of the initial beam that are subsequently deflected and dumped.

Figure 4.15 illustrates, how the DC beam is just switching between deflection to transmission mode. The resulting beam bunch (bunch length of $12\,ns$ in front of the

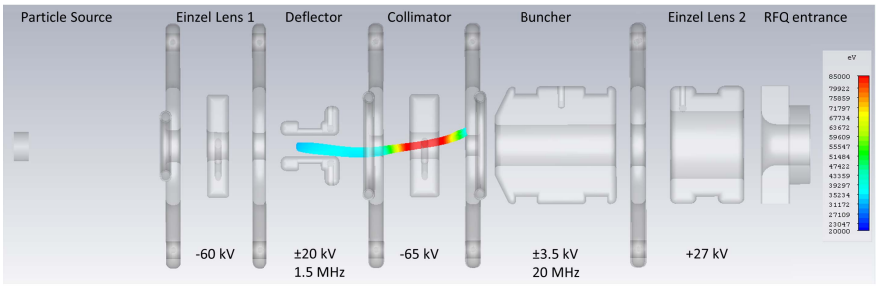

Figure 4.15: Results of simulation of deuteron beam transport in the region of the beam chopper. The color code indicates deuteron energy from blue to red ($20\,keV$ to $85\,keV$)

buncher) is transmitted to the collimator einzel lens which is operated at a voltage of $-65\,kV$. This lens focuses the bunch into the harmonic buncher which is operated at a frequency of $20\,MHz$ at $\pm 3.5\,kV$ peak amplitude voltage. Its phase is adjusted such

that the zero crossing from positive to negative voltage takes place exactly after half of the bunch has crossed the first gap. The peak voltage is still an estimated value. This was planned to be fine tuned during the proof-of-principal experiment. Figure 4.16 shows the energy distribution of the bunch after traversing the first bunching gap.

The last einzel lens (operated at $27\,kV$) finally focuses the bunch through the end

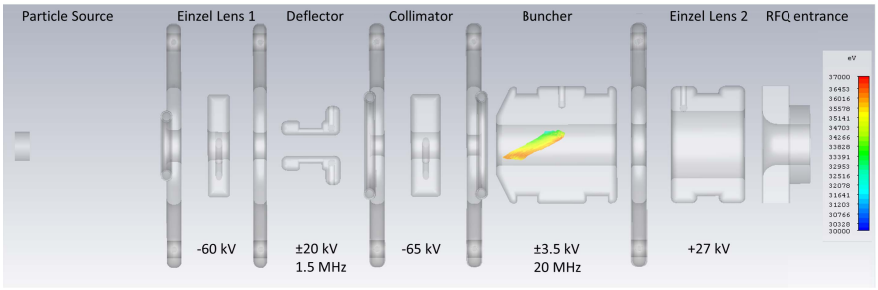

Figure 4.16: Results of simulations of deuteron beam transport in the buncher section of the pulsing system. The color code indicates deuteron energy from blue to red ($30\,keV$ to $37\,keV$)

flange into the DWIK RFQ (as shown in figure 4.17). The accumulated charge of the bunch was determined to be $230\,pC$, which is 13% more than the required value of $200\,pC$. If during the operation nevertheless lower bunch current is transmitted, the input beam current at the ion source can be increased.

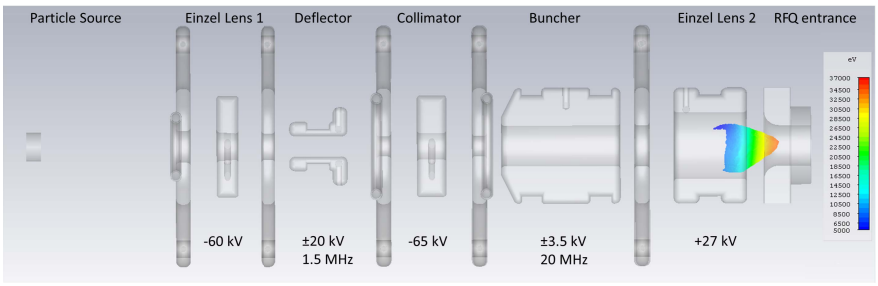

Figure 4.17: Results of simulations of deuteron beam transport in the extraction region of the pulsing system. The color code indicates deuteron energy from blue to red ($5\,keV$ to $37\,keV$)

4.4 Longitudinal Chopping

The fact that a decelerating einzel lens has a limited focusing strength (because its voltage cannot exceed the beam energy), leads to another possible approach for a beam chopper: If the decelerating voltage of the lens exceeds the beam energy, the particles

get decelerated to zero energy and furthermore accelerated in the inverse direction. If the beam energy could be modulated, in other words the energy would be raised in a specific time interval and the lens voltage would be set to a point where the regular beam is barely reflected, the increase in beam energy would lead to a beam transmission. The parts of the beam which are reflected and collected near the reflector have comparably low energy and thus do not lead to unwanted neutron background production.
This approach could be further generalized to two required principal optical elements: One is an energy modulator which can be either pulsed or sinusoidal to mark the beam interval that have to be either removed or transmitted. The second device is an energy filter, which could (apart from an einzel lens) also be a dipole magnet. Of course, additional beam optics will be required to recover acceptable beam parameters after the chopping process.
To validate these longitudinal chopping options, a CST Particle Studio simulation was prepared. In it, a DC deuteron beam from a $36\,keV$ ion source was focused by means of an accelerating einzel lens injecting into an energy modulator and finally a decelerating einzel lens. The energy modulator was operated at a $20\,MHz$ sinusoidal high frequency with $20\,kV$ peak voltage. With this frequency, a particle-bunch was accelerated to around $76\,keV$ in two accelerating gaps. The decelerating einzel lens consists of a decelerating gap with a voltage of $70\,kV$. This implies that only particles with kinetic energies above $70\,keV$ can be transmitted through this gap. This results in a bunched particle beam with a frequency of 20 MHz as figure 4.18 demonstrates.
The same figure also illustrates a major problem of this longitudinal chopping ap-

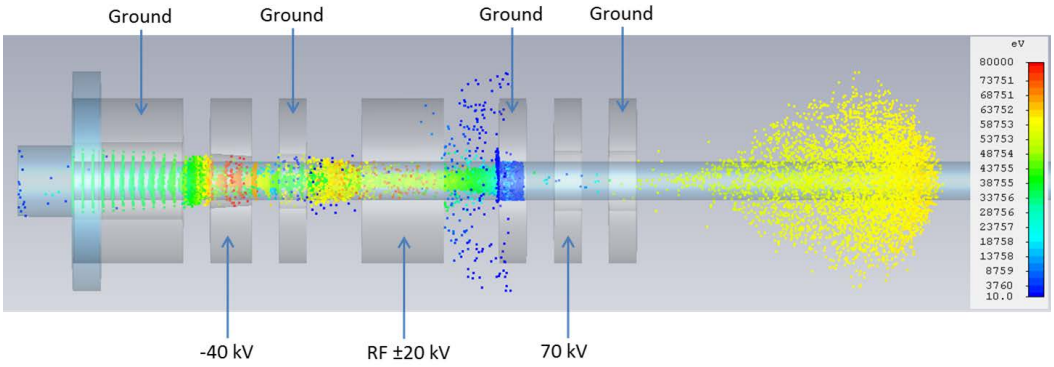

Figure 4.18: Simulation results of a first longitudinal chopping approach

proach: A large percentage of the incoming deuteron beam is reflected backwards and later accelerated in the direction of the ground electrode (cathode) of the ions source. To reduce the reflected beam current, grounded deflecting rods were placed in the mid-

dle of the deceleration gap. Particles unable to pass the latter exhibit very low kinetic energy and can thus be easily accelerated or deflected transversally, out of the beam direction. Since the beam energy during deceleration in the forward direction is high, the transverse momentum induced by the rods is negligible. Only after deceleration and re-acceleration will they affect the inverse deuteron beam as figure 4.19 indicates.

Another difference between the simulations presented in figures 4.18 and 4.19 is the

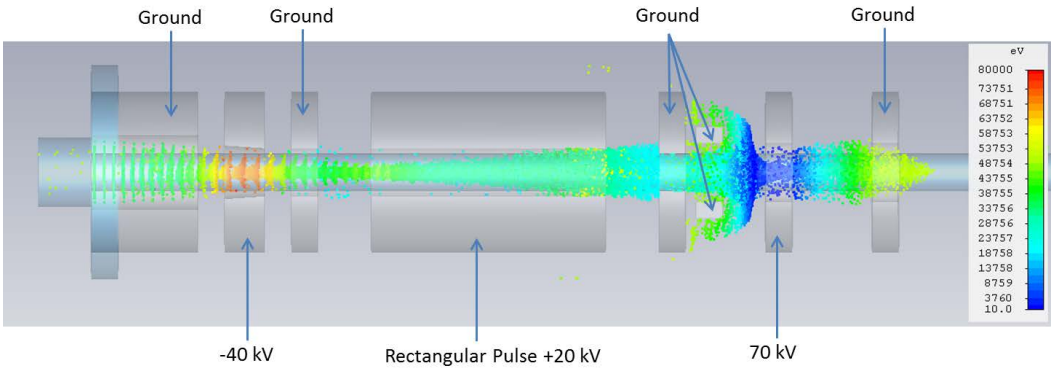

Figure 4.19: Simulation of longitudinal chopping employing deflecting rods

time modulation of the voltage applied to the energy modulator. Whereas, in the first case, leading to results from the figure 4.18 configuration, a sinusoidal voltage employing both gaps for resonant acceleration was used, in the second set of simulations a rectangular voltage function was applied to the energy modulator. The advantage of a rectangular pulse is a steeper gradient between accelerated (transmitted) and not accelerated (reflected) particles. However, just a single gap is employed for acceleration, but the drift tube needs to be prolonged, to prevent deceleration of earlier particles in the second gap. In addition, the application of rectangular pulses shortens the required length of the drift tube dramatically: Employing a sinusoidal pulse, the bunch has to be amplified using well matched phase correlations of the RF electric fields in both gaps. Thus, the length of the drift tube needs to be of the order of half the period. At $3\,MHz$ and a beam energy of $36\,keV$ this would lead to a required length of around $300\,mm$. Employing a rectangular pulse enables reserving the first gap exclusively for acceleration. This reduces the length of the drift tube to $40\,mm$, since it only needs to cover the bunch itself (and not half of the period).

In deploying such a chopping scheme, the beam energy difference between transmission and reflection should be kept small, since MHz pulsing in the regime of several kilovolts and bunch lengths below $20\,ns$ is not yet state-of-the-art. Like all cylinder symmetrical, beam optical elements, electrostatic lenses exhibit a focusing field gradient dependent on the radius from the beam axis. To keep the required energy

filter voltage low, a tube with a small diameter of 24 mm was selected. To increase the fraction of the longitudinal component of the electric field, the lens tube and gap lengths have to be set to 25 mm and 10 mm respectively. In later optimization stages, the gap lengths (instead of the tube length) have been enlarged, since this improves the high-voltage and vacuum stability. This geometry leads to a voltage of 37.4 kV at the decelerating einzel lens, which enables switching between reflection and 90% transmission employing a beam energy increase of 700 eV. Full transmission can be achieved by a beam energy boost of 1.2 keV. Figure 4.20 shows simulation results of the optimized setup. Here, a 60 mm long energy modulator tube is located in front of the energy filter lens without an additional ground aperture, so pulses as short as 30 ns can be chopped out of a DC beam. Since rectangular HV-pulse are ultimately to be applied, the energy modulator is already grounded again, by the time the accelerated bunch exits the tube. All particles which exit the tube during the pulse see a stronger reflecting potential.

Since a suitable rectangular high voltage pulse generator at operational frequencies at

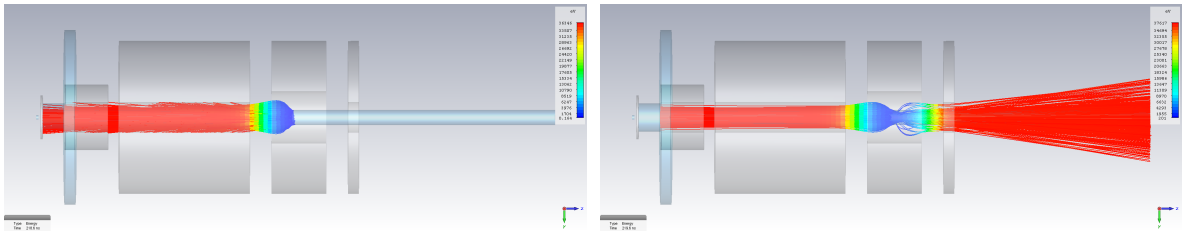

(a) (b)

Figure 4.20: Optimized longitudinal chopper setup: (a) blocking of a 36 keV beam, (b) full transmission of a 37.2 keV beam. The color code indicates the beam energy from blue (0 eV) to red (37 keV)

the MHz regime was not available at the design phase of the pulsing system, transversal chopping was selected. Nevertheless, simultaneously with this thesis, a comparable longitudinal einzel lens chopper was developed and tested at KEK research center in Japan [56]. There, no energy modulator is employed, but the voltage of the einzel lens itself is pulsed.

5 Pulsing System - Experimental Aspects

After the physical design of the pulsing system was frozen, an engineering design had to be developed in order to build and test the entire pulsing system. The design as well as the manufacturing took place in close collaboration with RI Research Instruments GmbH and is described in section 5.1, whereas the setup and commissioning of the entire pulsed beam injector system (PBIS) prototype was performed at PTB.
Originally, the evaluation of the pulsed high intensity neutron source had been planned in two steps: In the first work package, a Pulsed Beam Injector System (PBIS) had to be designed and set up. It consisted of an ion source, an LEBT section as well as several beam diagnostic elements. After successful commissioning of the PBIS, the entire equipment was envisaged to be be implemented on the existing RFQ accelerator facility at NECSA (described in section 3.3), so as to measure the resulting pulse structure after RFQ acceleration.
During the work on commissioning the PBIS it turned out, that the Necsa facility would not be ready in time to achieve the beam quality required for performing the final experiments there. Furthermore, the experimental verification and optimization of the PBIS system turned out to be much more complex than initially planned. For this reason, the implementation and testing of the PBIS system at the DWIK RFQ could not been included in this work.
Instead, a test bench was set up at PTB consisting of an ion source, an LEBT as well as beam diagnostic elements to be able to commission and perform proof-of-principle experiments of the PBIS.
The setup of the PTB test bench can be found in section 5.2 and those following. The final proof-of-principle experiments to evaluate the pulsing system are described in section 5.5

5.1 Manufacture and Commissioning of a pulsed beam injector system

As the first step in the manufacturing process, an engineering design of the PBIS was worked out. Already at a preliminary design stage, it turned out that the entire pulsing system would have to be divided into two major parts: the entire lens system would have to be designed as an insert to a vacuum chamber, so that it can be separately mounted, aligned and maintained. The vacuum chamber including several ports forms the second major component.
Concerning the insert/lens system, several requirements had to be considered: The pulsing system is designed for a DC input beam with a current of $30\,mA$ of which a small fraction of about $1-3\,\%$ is transmitted after pulsing. The remaining beam will be dumped either at the deflector plates, the deflectors aperture or at other lenses. As a consequence, most of the beam power, which is about $1\,kW$, is converted to heat at the lenses and electrodes of the PBIS and must be extracted from the system. However, all lenses operate at different high-voltages, so a cooling assembly that is electrically isolating, thermally conductive, readily machinable and meets strict mechanical tolerances had to be found. Furthermore, everything ultimately needs to be mounted in such fashion that sufficient pumping can be provided to keep the vacuum good enough ($< 10^{-5}\,mbar$), to prevent high voltage discharges.
This vacuum chamber will need to be capable of incorporating all necessary feedthroughs for the high-voltages, the RF-powers as well as for the cooling water supply. Furthermore, it has to provide pumping ports to accommodate high vacuum turbo molecular pumps. To be able to operate the PBIS system at the DWIK RFQ accelerator facility, the beam input and exit ports will have to connect the entrance side of the LEBT exit flange with the exit of the RFQ entrance flange. A preliminary sketch of a rectangular vacuum chamber with CF150 ports to be equipped with turbo molecular pumps can be found in figure 5.1.

In this design the lenses, in circular shape and made of copper, are mounted inside ceramic holders that are continuously adjustable over the entire span of three threaded bars. This preliminary sketch did not address the problem of cooling for the high-voltage lenses. An updated concept that provides the necessary cooling assembly consists of a two stage approach: employing regular deionized cooling water, a first isolated element made of ceramics would have to be cooled. This element is in good thermal contact with the electrode. The main task with this idea is the low thermal conductivity of most available ceramics. Only aluminum oxide ($\sim 30\,\frac{W}{m\cdot K}$)

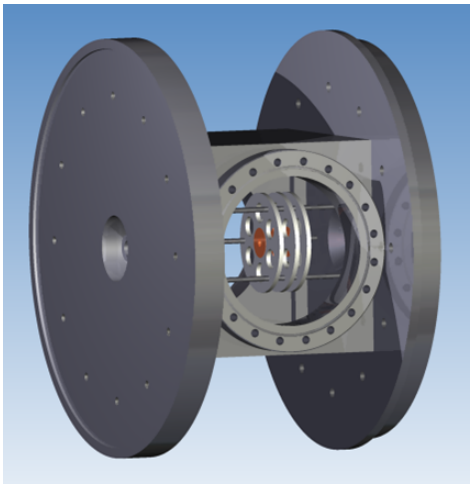

Figure 5.1: Preliminary schematic of the chamber and inlay design

and aluminum nitride ($\sim 180\,\frac{W}{m\cdot K}$) exhibit thermal conductivity that is not too far from that of copper ($400\,\frac{W}{m\cdot K}$). And yet, both of these ceramics are machined into the required shape either by sintering or need to be annealed afterwards. However, after these thermal processes, the strict mechanical tolerances that determine the overall alignment can hardly be met. To overcome these issues, a ceramic material was identified, which combines all required specifications: Shapal Hi-M Soft [57] is a machinable ceramic (like Macor) that is extremely resistant to voltage-breakdowns and also has a high thermal conductivity (see table 5.1). It is based on aluminum nitride, but several percent of boron nitride is added to improve the machinability.

With this material, the cooling scheme could be realized as follows: the central ele-

	Aluminum Oxide	Aluminium Nitride	Shapal Hi-M Soft
Density / $\frac{g}{cm^3}$	3.7 - 3.98	3.24 - 3.34	2.88
Therm. Conductivity / $\frac{W}{m\cdot K}$	25 - 30	86 - 184	92
Therm. Exp. Coefficient / $\frac{10^{-6}}{K}$	7.5	4.8	5.2
Withstand Voltage / $\frac{kV}{mm}$	30 - 35	18.7 - 36.7	56
Bending Strength / MPa	150 - 500	356 - 511	300

Table 5.1: Properties of thermally conductive ceramics [57][58]

ment is a block of copper, which functions as the actual electrode. To this block, on two sides, a holder made of Shapal ceramics is brazed. It featured a deep bore hole, to which a copper cooling pipe is brazed. Other bore holes provide the mount for aligning the lenses to a stack (the inlay) by means of threaded bolts (compare figure 5.2). The deflector is realized in the same way, but it employs only a single ceramic.

The two deflector plates are made of tungsten, which are (after copper plating) brazed to the ceramic. Since the buncher lens constitutes a longer drift tube, a total number of four ceramic plates was brazed to it. Figure 5.2 shows the final CAD model of the first einzel lens as well as the deflector.

Brazing joints between copper and ceramics are state-of-the-art technology, but

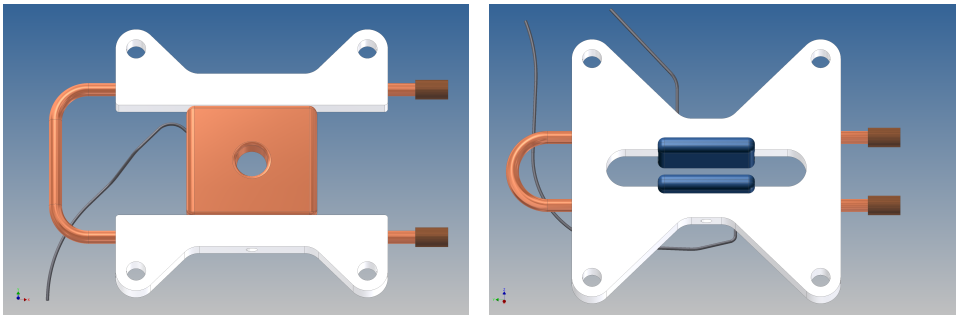

(a) (b)

Figure 5.2: Final CAD models of (a) the first einzel lens and (b) the deflector; white material: Shapal machinable ceramics, blue: tungsten, brown/orange: copper

usually, the ceramics is copper-plated prior to the brazing process. However, no manufacturer could be found for copper plating the Shapal ceramics, especially not inside the deep bore hole of the cooling pipe. Nevertheless, another approach was found to realize the joint: Aluminum nitride or oxide ceramics are typically brazed employing so called active metal brazes. These brazes consist of two components. Whereas one component such as e.g. titanium takes over the oxide or nitride atoms in a chemical reaction, the principal component of the braze can produce the joint with pure aluminum at the surface of the ceramic, via the reaction:

$$AlN + Ti \Leftrightarrow Al + TiN$$

However, according to the manufacturer of the Shapal ceramic, a brazing joint of Shapal and a metal employing an active metal braze has never been done yet. Thus, test brazes were performed employing a regular aluminum nitride ceramic as well as a piece of Shapal to braze them on top a copper-slab and a copper pipe through them. For the joint, the braze Cusil-ABA by MTC Wesgo Metals [59] was employed, which is a 63% silver, 35.25% copper and 1.75% titanium braze. To perform the brazing process, the vacuum brazing furnace of the University of Bonn was employed. A picture of the brazing samples can be found in figure 5.3. Since micro-graphic examination of the

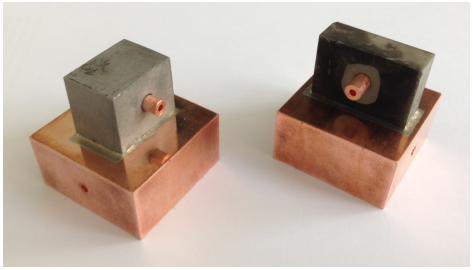

Figure 5.3: Brazing samples (left: Shapal, right: AlN)

brazing results were not possible due to the ceramics, pressure tests were performed to qualify the brazing result. A pressure of more than 13 *bar* to the ceramic block (applied perpendicular to the brazing) did not lead to destruction of the joint, which is more than the joint has to sustain during the application. Furthermore, the cooling tube sustained a pressure of 1.5 *bar*. In the application, the tube does not have to sustain forces at all, only thermal contact is required. Thus, the brazing tests were successful and all lenses could be manufactured in this fashion.
For the ground apertures, the X-shape of the high-voltage lenses was adopted, but the entire lenses were manufactured employing either copper or tungsten, in order to reduce the effect of sputtering for all lenses that undergo intense beam loads. To cool the ground apertures, a copper pipe was also brazed on top of each.
Another main concern during the design phase was the alignment procedure. Since the pulsing system was planned to be tested at the DWIK RFQ, the alignment procedure of the pulsing system was based on the alignment of the LEBT to the RFQ: Here, a dowel pin was employed to align and mount the LEBT to the RFQ. For the pulsing system the following procedure was developed: to ensure optimal alignment on the beam axis, the chamber of the pulsing system is first aligned and mounted to the RFQ employing a dowel pin. When this pin is removed, the inlay can be inserted. The inlay itself is aligned during the assembly by means of a special alignment tool based on a single dowel pin with multiple diameters and spacers (see figure 5.4).

At both sides of the inlay-stack, a disk with precisely machined outer diameter is placed. Using a notch fit at the entrance and exit flange of the chamber, the inlay can be aligned to the previously-aligned chamber. To connect the original LEBT to the pulsing system, the same procedure and dowel pin can be employed, since the geometrical dimensions of the entrance flange of the pulsing system are identical to those of the RFQ entrance flange. To test the PBIS system at PTB, adapter flanges were designed to mount standard CF150 flanges on the beam entrance and exit port of the chamber, whereby the ion source and LEBT can be fitted to the input side and

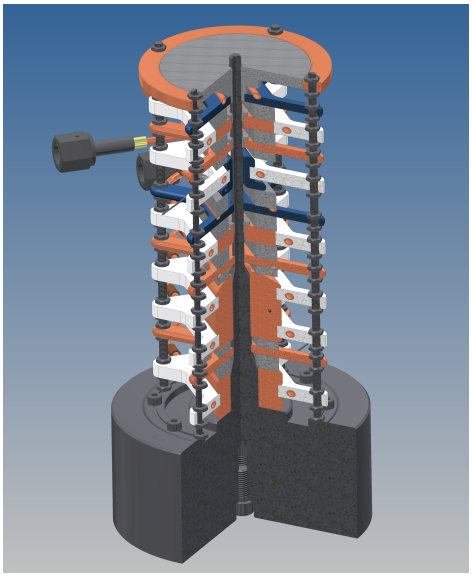

Figure 5.4: Lenses, beam deflector and buncher,mounted on a dowel pin for precise alignment

a target chamber equipped with beam diagnostic elements to the output side. The final design of the chamber including the inlay can be found in figure 5.5.

Apart from one ceramic element of the collimator lens which broke during assembly

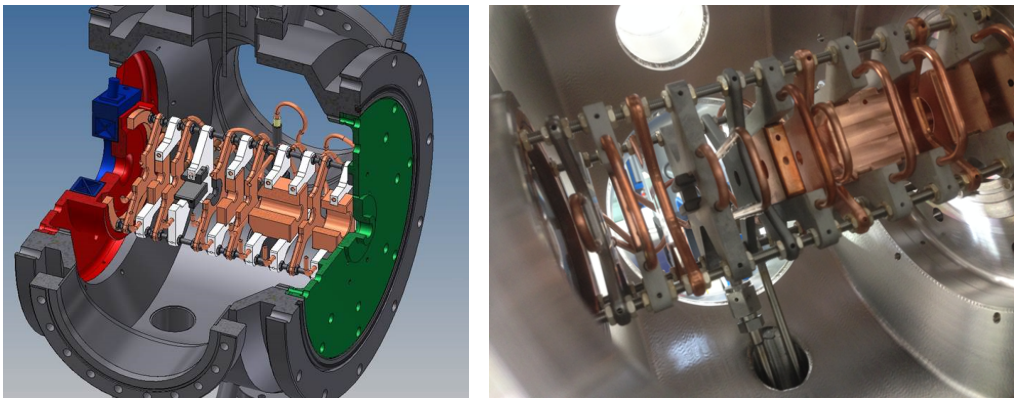

(a) (b)

Figure 5.5: Overall view of the (a) CAD model as well as (b) photograph of the chamber and inlay

(after successful brazing) but could be fixed employing a glue suitable for application in vacuum (so called Stycast [60]), manufacturing and assembly of all lenses and electrodes as well as vacuum leak testing and cooling water pressure testing were completed successfully. A photograph of the broken and successfully repaired collimator lens can be found in figure 5.6.

The next step was a performance test of the high voltage insulating between the

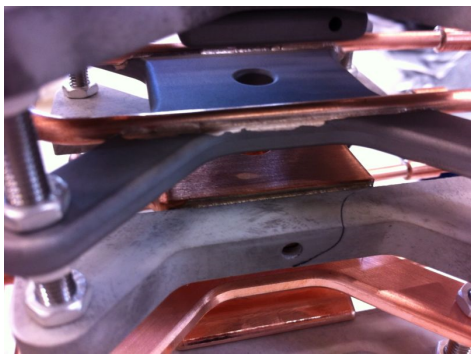

Figure 5.6: Broken and glued ceramic at the collimator lens

electrodes and to ground in a high vacuum environment. Here, several problems were encountered: on one hand, after a short period of HV-conditioning, only a low voltage of less than $1\,kV$ could be applied to the collimator lens. Furthermore, the other lenses also exhibited problems in sustaining voltages in excess of $20\,kV$. Applying such voltages lead to spontaneous discharges to ground. Moreover, HV-conditioning did not diminish the frequency of discharges. The dielectric properties of the ceramic and its surfaces even deteriorated during this process. Initially, we attributed this to out-gassing of small air inclusions which might have been produced during the brazing process. An attempt to solve this problem by baking the lenses and electrodes in vacuum at about $80\,°C$ employing the cooling system did not solve the problem. To visualize the discharges and localize their paths, a glass window was mounted to one of the turbo pump ports. Thereby, an unexpected phenomenon was observed. At high-voltages, a glow-discharge had ignited on the surface of the ceramics in all lenses (see figure 5.7).

The color of the glow-discharge indicated the presence of nitrogen on top of the sur-

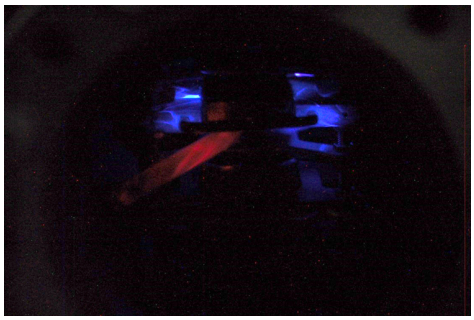

Figure 5.7: Glow discharge on the surface of the Shapal ceramics

face. Consultation with the Shapal supplier ruled out nitrogen out-gassing from the

Shapal ceramics. Ultimately, only dismantling of the PBIS electrode stack revealed that the reason for this discharge is surface contamination of the ceramic insulators. As figure 5.8a indicates (compare ceramic surface left and right of the copper electrode), the ceramics surface must have been contaminated with copper or carbon during the brazing process. Due to this contamination, a small amount of surface conductivity might ensue when HV is applied, and the resulting current flow could cause out-gassing. Such a process trigger a self-sustaining glow-discharge promoting further out-gassing.

To overcome these problems, the entire lens stack had to be disassembled and the

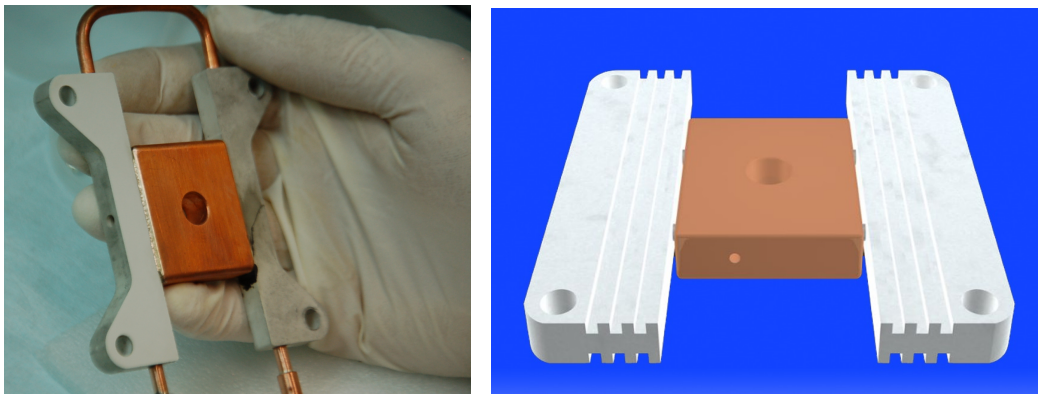

(a) (b)

Figure 5.8: (a) Ceramics during polishing process (b) new collimator lens without cooling

welded cooling pipes cut. For lack of time, a re-brazing of the cooling system was abandoned. However, a new collimator lens could be manufactured employing a much simpler design (see figure 5.8b): dowel pins were employed to clamp the lens to the insulators. Since no cooling is foreseen in this design, Macor could be employed instead of Shapal. Furthermore all other Shapal ceramics had to be polished employing a diamond polishing paste and the surfaces carefully cleaned again before reassembly. After this refurbishing process, all lenses were capable of holding voltages of up to $50\,kV$ which should be sufficient for the first experiments.

5.2 Overview of Test-Bench

As indicated above, the experimental work of this thesis focused on setting up a dedicated test bench to perform proof of principle measurements of the pulsing system

and to verify the simulation results. A photo of the test bench can be found in figure 5.9. The final version of the test bench consists of an ion source (see section 5.2.1) that

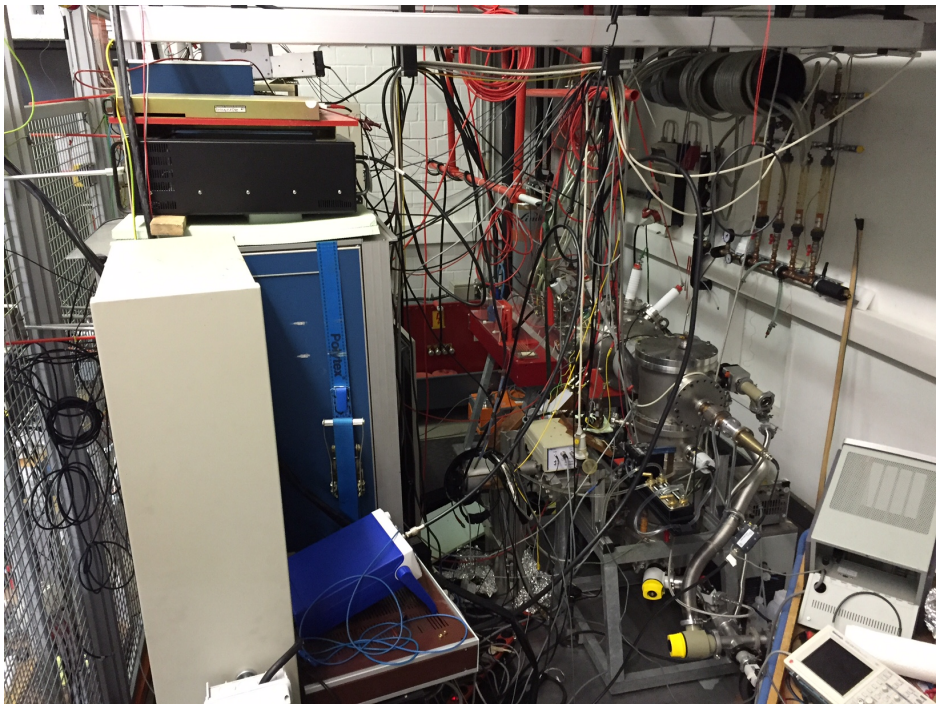

Figure 5.9: Photo of the test bench for the PBIS system at PTB

delivers an ion beam, which is then transferred to the LEBT. During the experiments helium ions were employed instead of deuterons, to avoid radiation protection issues by neutron production in the experimental setup. The beam is focused by a low energy beam transport system (see section 5.2.2) to the chamber of the pulsing system. Instead of the RFQ, the pulsing system is followed up by a diagnostics chamber which is able to characterize the beam at the point where typically the longitudinal beam shaping of the gentle buncher would be located. The description of the employed beam diagnostics can be found in section 5.2.3.

5.2.1 Ion Source

To be able to determine the properties of the pulsing system, a stable, well focused ion beam at an energy of $35\,keV$ had to be supplied. For this, a Cold or HOt Reflex Discharge Ion Source (CHORDIS) developed at GSI Darmstadt [61][62] and manufactured by Danfysik[63] is employed. A schematic view of the source can be found in figure 5.10. This ion source is a filament-based so called multi-cusp source. The ion source consists of a vacuum chamber filled with low pressure gas at approximately $10^{-3}\,mbar$. In our case Helium is used, but it can also be hydrogen, deuterium or other

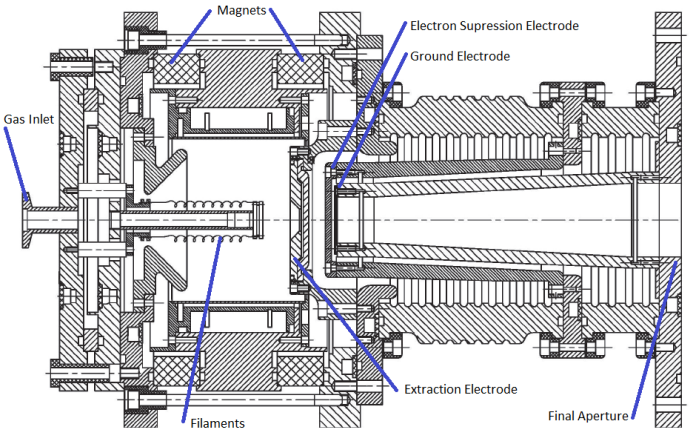

Figure 5.10: Schematic view of the CHORDIS ion source [63]

gases. Free electrons are generated by thermal emission from an electrically heated, coiled tungsten wire. The electrons are then accelerated towards the wall of the plasma chamber, where a discharge voltage of around $80\,V$ to $100\,V$ is applied. The plasma is formed by electron collisions with the gas atoms or molecules in the source. To prolong the electron path, thus increasing the collision probability of the confined electrons, water cooled permanent magnets are attached to the walls of the plasma chamber. If the entire source including the extraction electrode (first electrode) is ramped to up to $+50\,kV$, a predominantly single-charged [62], positive ion beam can be extracted. A small amount of multiply-charged ions can be generated by applying a discharge voltage of several hundred volts. The extraction system consists of only three electrodes: as mentioned above, the first electrode is at source-ground potential, operated at most of the experiments at $+35\,kV$. The second electrode, called electron suppression electrode, is set at negative potential (typically operated at $-3.5\,kV$). The third electrode is set to beamline ground potential, in order to keep the following beamline also at ground potential. This so called accel-decel system is used to focus the extracted beam and also to prevent secondary electrons from the upper beamline being accelerated backwards into the plasma chamber by the electron suppression potential. In addition, the ion source can be equipped with a filament-driven oven to vaporize solid materials such as metals or sulfur. Furthermore, a sputter electrode can be introduced into the plasma chamber to produce ion beams from electrically conductive materials with a very high melting point. Since CHORDIS is a multi-purpose source, the electrode system needs to be optimized for the required operating conditions.
Operating the ion source in DC-beam mode, beam currents of up to $45\,mA$ of a helium beam could be produced in early operation tests employing DC beam current probes

outside the beam-line. In further experiments it turned out that the beam quality needed to be significantly improved in order to operate the pulsing system. Further details on multiple ion source optimization can be found in section 5.3.

5.2.2 Low Energy Beam Transport (LEBT)

To be able to focus the beam in the region between the exit of the ion source and the chamber of the pulsing system, a first LEBT module was designed with just a single einzel lens. The high-voltage and first grounded electrodes were built of two tungsten disks of thickness $2\,mm$ and diameter $100\,mm$. These were equipped with aperture holes of diameter $50\,mm$ on the beam axis and maintained at a distance of $6\,mm$ from each other by means of three ceramic spacers (see figure 5.11).

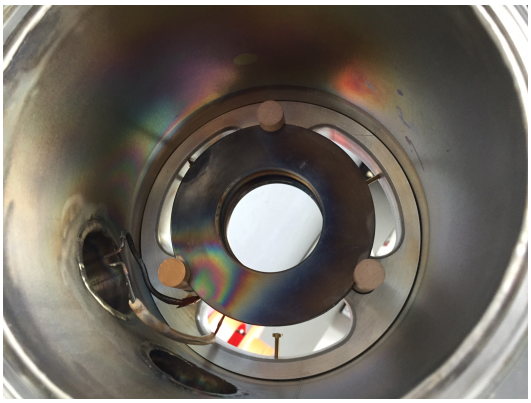

Figure 5.11: Photo of first LEBT module consisting of a single aperture-based einzel lens

These spacers were mounted on a stainless-steel base aperture, which acts as the second ground lens and maintains the same $6\,mm$ distance between central (high-voltage) disk and stainless steel aperture. The stainless steel base has an outer diameter that fits into a standard CF150 beam pipe.
Figure 5.12 shows the result of measurements taken at different focusing voltages at the einzel lens. The beam current was measured at different positions of the movable target (compare section 5.2.3).

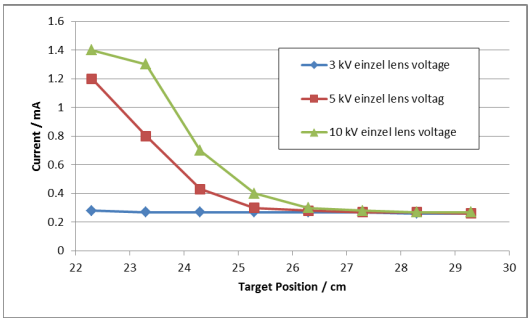

Figure 5.12: Beam current measurement results employing first LEBT

The target diameter ($50\,mm$) was much larger then the anticipated beam size. The plots indicate an improvement in beam focus when the focusing voltage is increased. On the other hand, if the focusing would form a pencil beam, calculations predict a plateau region (parallel beam) or peak (converging beam) would be expected when the target is moved closer to the source. The measurement employing $10\,kV$ on the einzel lens shows the first indication of such a plateau. Thus, stronger focusing appears to be required. However, due to the low thickness of the disks and the resulting field-peaking at their edges, no stable operation above a voltage of $10\,kV$ could be achieved.
Furthermore, it became apparent that a steering element was required in the LEBT. In its redesign, two einzel lenses with an x-y steerer between them were employed to achieve stronger focusing and incorporate steering capabilities. In addition, the aperture-based design was replaced by a tube-based design. A schematic view of the modified system is shown in 5.13a with an overview of the individual components in figure 5.13b.

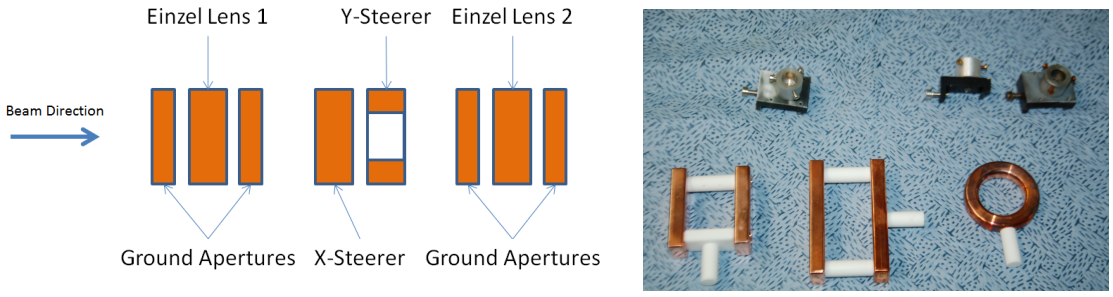

(a) (b)

Figure 5.13: (a) Overview of the LEBT section (b) rail system based lens holder (see text below)

To maximize the flexibility of the beam optic elements, all lenses were placed on a rail system. The lenses are mounted on an insulating stand, which allows for variations in

height of up to 10 mm. The insulator is made of Makor-ceramics, to permit applying high voltages to the lenses. The inner diameter of the lenses was chosen to be 30 mm (with an outer diameter of 50 mm). These values are a compromise, since a larger lens would exhibit a more homogeneous electric field and less aberration effects, but it would also require higher focusing voltages. The steerers are similarly designed: in the vertical direction, the lower steerer plate is connected to a comparable insulating stand. Two Makor rods act as insulating spacers to maintain the upper steering plate in place. At the horizontal steerer, the stand is connected to one of the spacer rods rather than to a plate. For the steerers, the distances of the plates to each other is also 30 mm. To align all lenses and the steerers on the beam axis, a dowel pin of diameter 30 mm and length 250 mm was manufactured; it acts as an alignment aid for the ion-optics elements (see figure 5.14).

The rail is welded into a CF150 beam tube of length 180 mm. Furthermore, the beam

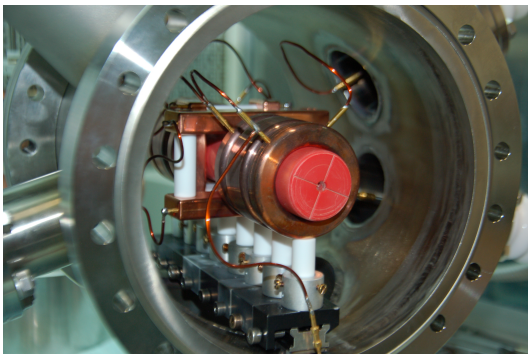

Figure 5.14: Alignment of LEBT elements

tube is equipped with two ports for the einzel lenses high-voltage feed-throughs (up to 20 kV) as well as a 4-port feed-through (up to 6 kV) for the steerer plates. In addition, a turbo pump is located at a third CF150 port just below the rail system, to meet the high-vacuum requirements (approximately $5 \cdot 10^{-3}\, mbar$ within the ion source and $5 \cdot 10^{-5}\, mbar$ within the LEBT). A fourth port incorporated a vacuum gauge which (apart from the standard usage) can be used to detect high-voltage arcing (sudden and short-term increases in vacuum pressure due to evaporation of surface materials in the discharge region), as well as beam loss (long-term increase of vacuum pressure inside the LEBT-section.

To evaluate LEBT performance and to determine an optimal working point for subsequent pulsing experiments, a helium beam of 35 keV energy was focused onto a fast faraday cup and the beam current was measured in arbitrary units (amplification of pre-amplifier was not calibrated). In this experiment, the pulsing system was not yet implemented, only macro-pulsing at ions source level (see 5.3) was employed. By

varying the high-voltage on the einzel lenses and employing the steerers to correct for a small misalignment of the lenses, the focusing voltages were optimized by measuring the achievable beam current behind the LEBT. The results can be found in figure 5.15. The x- and y- axes display einzel lense voltages, while the z-axis visualizes the

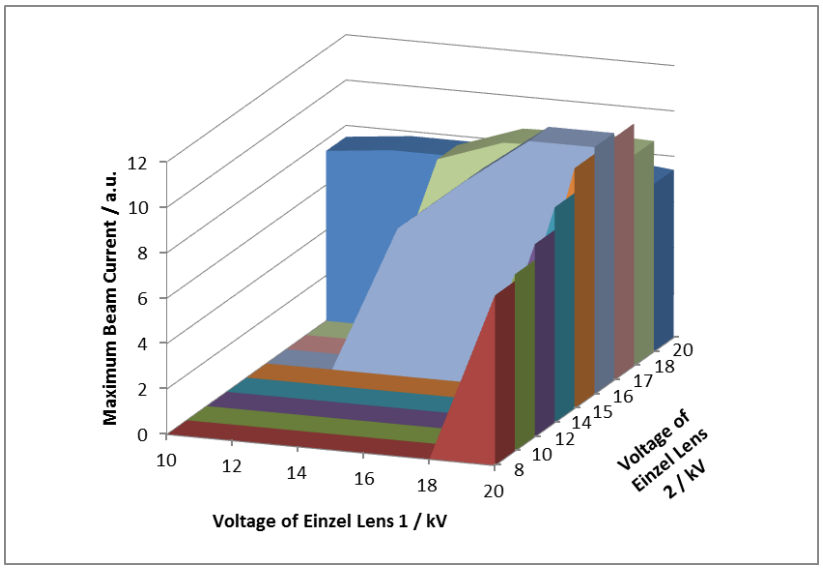

Figure 5.15: Results of the LEBT parameter optimization measurements

measured beam current. The maximum current was obtained at voltages of $18-20\,kV$ at einzel lens 1 and $16\,kV$ at einzel lens 2.

5.2.3 Beam diagnostics

To be able to analyze the transversal and longitudinal beam characteristics, beam diagnostic elements are required. Since the LEBT has to be as compact as possible to keep space-charge induced beam broadening low, there is no space for diagnostic elements in the ion source, LEBT or the pulsing system, but a beam diagnostics chamber is placed behind the PBIS.

The diagnostics chamber consists of a vertically mounted CF200 tube, which exhibits two horizontal CF150 ports for the beam axis. At the bottom side, a turbo pump is installed, to provide the required vacuum conditions. Also several ports for vacuum diagnostics, high-voltage feedthroughs or signal connections are available.

Information on beam properties such as axial position, lateral beam size and shape as well as beam current, were obtained by various beam diagnostic elements downstream from the LEBT.

To obtain first qualitative information about the lateral beam size, a transparent acrylic glass plate was mounted inside the diagnostics chamber, to act as a target.

Beam heating of the latter due to the impinging ion beam produced a color change in the material, which represent the lateral beam shape. Figure 5.16 shows the result of such an experiment. Utilizing this method, a misalignment of the ion source extraction-optics could be determined. This resulted in a severe deviation of the real beam position from the nominal beam axis. Consequently, this motivated the introduction of an x-y steerer as part of the LEBT section. The earliest online diagnostic

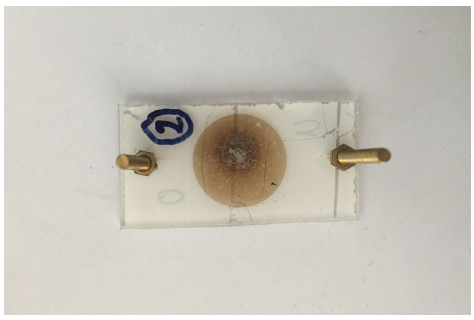

Figure 5.16: Beam spot imaging employing acrylic glass

element for measuring beam current and getting rough information on beam shape was a tungsten disk mounted on a feed-through, movable in beam direction (see figure 5.17). Furthermore, this target was equipped with a tungsten ring above the disk, to apply secondary-electron suppressing potential. The beam current was determined by measuring the voltage drop on a dedicated resistor between disk and ground (of typically $2k\,\Omega$). By axially moving the target position and monitoring the current ratio (beam on the electron suppression ring compared to beam on the disk) as function of distance, the beam divergence could be analyzed and optimized.

The beam position was also validated at the same location employing a commercial,

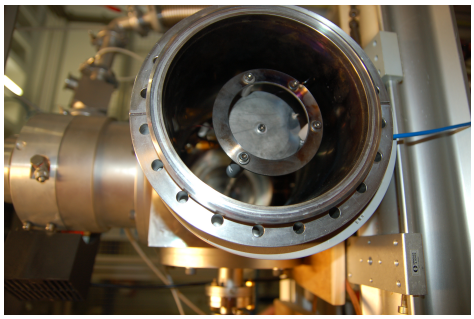

Figure 5.17: On-beam-axis movable target equipped with electron suppression ring

rotating-wire beam-profile monitor, but at a later stage this device was eliminated due to a lack of space inside the chamber. Furthermore, the beam profile monitor is unable to measure longitudinal beam shape parameters such as e.g. pulse length during PBIS

operation.
Also, the movable tungsten target was replaced when the experiments for evaluating the high-speed pulsing properties began. For these, the first tungsten target was replaced by a $50\,\Omega$ impedance-matched, fast Faraday cup (FFC) with a measurement bandwidth of $\approx 10\,GHz$ which is high enough to measure beam pulses in the ns-range. In these measurements the beam position was optimized by maximizing the beam current on the small entrance hole of the FFC, using the X-Y steerer of the LEBT. Furthermore, since the impedance of $50\,\Omega$ is significantly smaller than in the DC measurement, the voltages are much lower, so that an additional pulse amplifier was employed. Special shielding and grounding precaution measures also needed to be taken, in order to reduce problems of electromagnetic compatibility (EMC), such as pick up signals from the fast high voltage ramps of the RF components in the PBIS system (see chapter 5.4).

5.3 Optimization of the Ion source

As described above, the extracted ion beam of the CHORDIS source was shown to have a beam diameter that is too large to be effectively focused by the first LEBT. On the other hand, to operate the PBIS system at the DWIK RFQ, macro-pulsing was required. Furthermore, pulsed beam operation could solve thermal issues arising from the dismantlement of the PBIS lens stack. For this purpose, two major modifications were applied to the ion source, to improve the operation: the extraction optics was modified and ion source pulsing was applied by pulsing the discharge voltage.
Moreover, the intrinsic distance between ion source extraction optics and the LEBT system is rather high. As indicated in figure 5.10, the three-lens system is located approximately in the middle of the ion source. A final, grounded aperture is placed after a field free flight path of $20\,cm$. This distance is required to separate the respective electric potentials by a vespel insulator. Since the ion beam leaves the three-lens system characteristically divergent (by approximately $22\,mrad$ [64]), the final aperture acts as a collimator on the divergent beam. This leads to a high secondary electron background by ion impact on the collimator walls in the end region of the source. Furthermore, such a large-diameter beam cannot be easily focused back on the beam axis without recourse to major additions such as solenoid or quadrupole magnets. This is due to the required electric field strength of the einzel lenses. An economical solution was found by collimating better the expanding beam from the source and reducing the final aperture diameter from 40 to $20\,mm$ by means of a tantalum disk. The dis-

advantage of this solution is beam loss, since the latter is again only collimated but not focused.
In the second step, the extraction optics was optimized for the transport of light ions. As explained above, the CHORDIS ion source is capable of accelerating a broad range of ions species from light ions such as hydrogen up to heavy ions such as bismuth or gold. Thus, in the standard setting, the original extraction optics is optimized for medium weight ions. To achieve a smaller beam diameter at source exit with less beam halo, the apertures of the ion source extraction system needed to be modified: Whereas the original apertures exhibit a pinhole of around $9\,mm$ and a distance between extraction lens and electron suppression lens of $9\,mm$, the dimensions of both measures were reduced to $4\,mm$, to maintain the aspect ratio (ratio between gap radius and lens diameter) close to the optimal value of 0.5([65]). A smaller aperture diameter (down to $3.05\,mm$ per pinhole at a seven-aperture extraction electrode) for light-ion beams such as helium is indicated in [62]. Since a single aperture is preferable, and an extraction energy of $35\,keV$ (requiring a minimum gap distance of $3.5\,mm$) needs to be applied, an aperture diameter value of $4\,mm$ was selected, as a compromise. These dimensions were suggested by R. Keller and Danfysik A/S in discussions. Thereby, the emittance of the CHORDIS source could be reduced from 40.5 to $18\,\pi \cdot mm \cdot mrad$ employing the approximation

$$\epsilon(\pi \cdot mm \cdot mrad) \approx 4.5 \cdot d(mm)$$

where d is the diameter of the aperture diameter [64]. Of course, due to the smaller aperture, the maximum achievable beam current is correspondingly reduced.
In this context, a second modification was the introduction of beam macro pulsing at ion source level: since it was originally planned to employ the pulsing system at the DWIK RFQ of NECSA - not a CW machine but one that is pulsed in $2\,ms$ long cycles at a rate of $100\,Hz$ - the heat load to the pulsing system and RFQ by the dumped beam is reduced significantly, if the ion source is also switched off during the pause period of the RFQ.
Since a pulsed extraction voltage power supply operating at $35\,kV$ is expensive and causes EMC problems, a much simpler solution was found in gating the discharge voltage of the ion source: with respect to the time constants of the RFQ macro-pulsing system, the formation of the plasma inside the plasma chamber is a fast process (in the order of $100\,ns$). Pulsing can be realized by switching the discharge voltage ($80-100\,V$) on and off. To perform this task, two different pulsing systems were used: during the first tests to determine the macro pulsing capabilities, a fast MOSFET based switch capable of working even on a nanoseconds time scale, was used. A schematic electric

circuit is shown in figure 5.18a. Its disadvantage was that the current load had to be dissipated by a 94 Ω power resistor, causing excessive heating. Furthermore, it could only be operated up to discharge currents of 0.85 A.

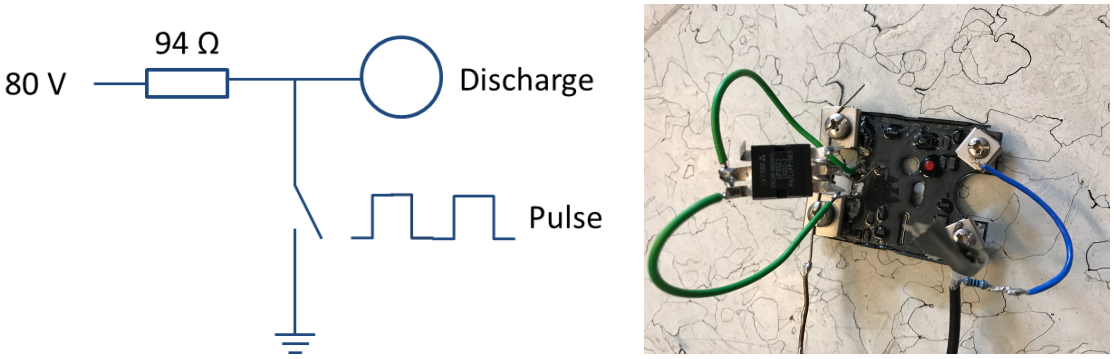

(a) (b)

Figure 5.18: (a) fast switch circuit (b) modified slow relay

To get rid of the required load, the fast switch was exchanged by a high-current solid-state relay HFS33 D-200D400M-L, capable of directly switching 200 V, 40 A of discharge current at pulse durations of down to the few-millisecond level. Due to high-voltage sparks, the built-in, solid-state relay MOSFET was destroyed several times. In order to combine the advantages of the above mentioned switches, the MOSFET of the relay was replaced by an IXYS DE150-501N04A (capable of switching 500 V at 4.5 A) without changing the other relay electronics. This modified switch enables stable operation in the milisecond pulsing regime. A picture of it is presented in figure 5.18b.
During a beam test employing the optimized ion source, the shortest possible pulse duration of the ion source pulsing needed to be quantitatively determined: employing a stable helium ion beam of 35 keV, the pulse duration was varied, in 10 steps, from 10.45 ms down to 10.2 μs. The resulting pulse length was measured employing the fast faraday cup located inside the diagnostics chamber. The results of this experiment are shown in figure 5.19.

To quantify the results and eliminate long-term beam current drifts - e.g. pressure drifts in gas injection, or oscillations of the measured signals due to e.g. RF-background noise - the length of the plateau region (rather than the height of the pulse region) compared to the input pulse length was studied. This plot is shown in 5.19. For a closer look on the resulting pulse shapes, the measured pulses of varying pulse length are plotted in figure 5.20 As these plots indicate, the rising slope is always steeper than the falling slope. The reason for this is as follows: the rapid discharge

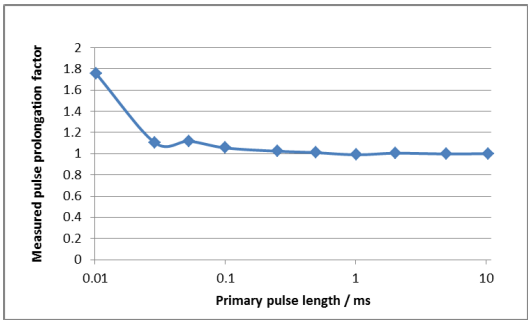

Figure 5.19: ion source pulsing experiments: quantitative analysis of the results

leads to a fast rise of ion concentration in the source. In contrast, at the end of pulse, the ion source is only gradually emptied of already existing ions. Furthermore, the length of the falling slope dominant over the plateau region at the short pulses such that the minimum pulse duration is mainly defined by this. For pulse durations down to $30\,\mu s$, the plateau region is still visibly reached. Thus, pulses down the latter duration can be realized by simply pulsing the ion source. This pulse duration corresponds to a pulsing frequency of $16.6\,kHz$ at a duty cycle of 50%, so the required macro-pulsing of the DWIK RFQ could be applied to the CHORDIS ion source. However, this pulsing is still around two to three orders of magnitude too slow to constitute a viable alternative for the PBIS system. However, it can substantially reduce the thermal load due to dumped beam.

The time dependence of the formation of the ion beam as presented in figure 5.20 can be interpreted as follows: The voltage pulse applied to the ion source triggers a discharge and causes the formation of a plasma. Free ions produced in this plasma are extracted and formed into a beam. To determine which process limits a faster pulsing of the ion source, a further experiment was performed. The time dependence of plasma formation was monitored by recording the light emission from the ion source. For this purpose, a photo-multiplier tube (PMT) was mounted, viewing the beam exit of the ion source through a quartz view port. Prior to plasma ignition, the tungsten filament used for initial electron production emits an orange light while under current. At the moment of plasma ignition, the plasma itself starts to emit light, the color of which depends of the gas inside. The photo multiplier, being sensitive enough to detect the change in light output due to the burning plasma, could be used to approximate the plasma ignition time scale. Like figure 5.21 indicates, the ignition time of the plasma is at least one order of magnitude faster than the fastest beam pulse that can be generated by ion source pulsing. The measured delay between filament light and plasma light is approximately $1\mu s$, but this includes also the time required for the discharge

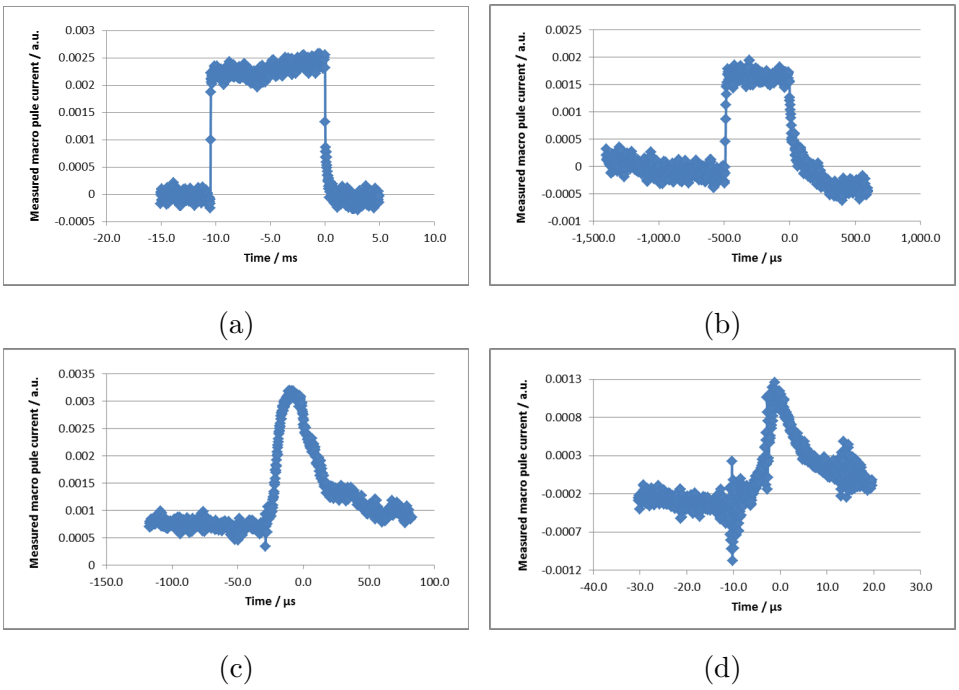

Figure 5.20: measured pulses at different input pulse lengths: (a) 10 ms, (b) 500 μs, (c) 30 μs, (d) 10 μs

power supply to ensure that its current limitation is functioning properly. The true plasma ignition time might be even shorter.

The reason for the much slower pulsing limits of the ion source relates to the mass difference between electrons and ions. Whereas plasma ignition is solely an electron-based process, for ion beam formation the ions have to be extracted out of the plasma in the direction of the extraction electrode - typically, a metal disk with a small hole bored through it. This process is realized (in case of the PBIS system) by applying an extraction voltage of 35 keV to the ion source. The potential of the entire chamber is raised to this value, to ensure there is no electric field inside. Indeed, it is the electric field from the plasma chamber, which leaks in via the extraction electrode that accelerates the ions in the beam direction. Inside the plasma, the ions exhibit a random movement at kinetic energies in the eV range [66]. Thus, only ions in the vicinity of the leaking field are gradually accelerated in the beam direction, to form the so-called plasma meniscus around the extraction electrode, from which they are extracted to the vacuum outside.

To determine the time it takes for a plasma ion with up to 1 eV energy to be extracted and then be accelerated to form the 35 keV ion beam, a simulation was performed employing the Tracking Solver of CST Particle Studio: simplified extraction lenses, together with the optimized CHORDIS source geometry and a surface source

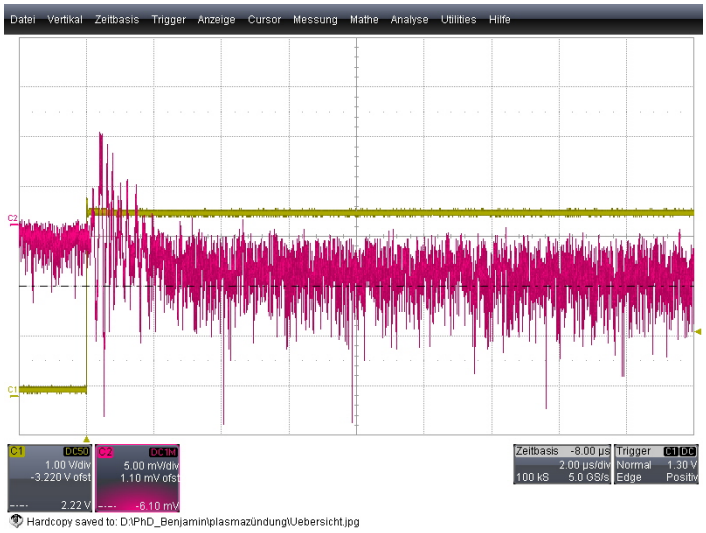

Figure 5.21: Measurement of emitted light from the ion source during plasma ignition. yellow curve: trigger signal, red curve: measured PMT signal

of beam-oriented $1\,eV$ helium ions located at the minimum distance between plasma and extraction aperture (the end of the gas inlet tube has been used as a reference) were employed. This is a best-case analysis. In reality, the plasma will be a volume surrounding the glowing part of the filament. Moreover, the plasma ions are not mono-energetic or collimated: thus, particularly in the periphery of the plasma meniscus, their motion is essentially random-oriented. The result can be found in figure 5.22

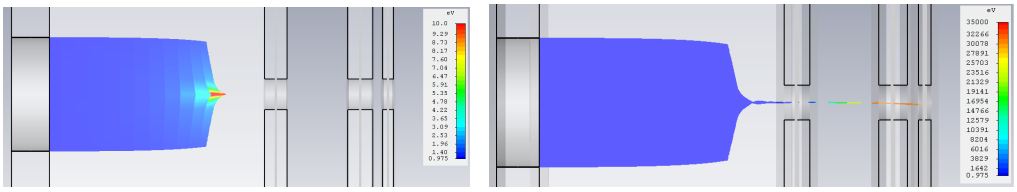

(a) (b)

Figure 5.22: Simulation of CHORDIS extraction: (a) formation of meniscus at $2.85\,\mu s$ (b) first extracted macro particle at $2.97\,\mu s$. The color code indicates particle energy. The color scales are different in the two pictures.

As the simulation indicates, for the first macro-particle (fraction of total beam charge, since not all single ions are modeled independently) it takes $2.97\,\mu s$ to be extracted from the plasma. The simulation was repeated for a lower but also realistic initial proton energy of $0.1\,eV$. In this case, the extraction time increases to $6.06\,\mu s$. Hence, the low helium ion energy inside the plasma (as well as the helium ion mass) is the limiting factor for fast ion source pulsing by means of the discharge voltage. This

effect can not even be improved by pulsing the extraction voltage.

5.4 RF Development

To operate the pulsing system, two sources of RF-power are required: first, an RF-signal must be imparted to the deflector plates to deflect the beam during the pause periods and only transmit a short beam pulse during the deflection voltage zero-crossing time-interval. Second, the buncher requires an RF-signal to compress the selected beam pulse. In an early design phase, a sinusoidal RF-signal was planned to be employed for both elements. By means of simulations, a voltage of 3.5 kV was found to be required for deflecting a 30 mA, 35 keV deuteron beam, such that it is no longer transmitted to the RFQ. In the PBIS system the period around zero-crossing is relevant for the formation of the beam pulse (more specifically the period in which the RF voltage changes from $\pm 3.5\,kV$ to $\mp 3.5\,kV$). This period should equal 30 ns (or less) to compress this beam pulse by the buncher to less than 5 ns inside of the RFQ. In conjunction with the desired repetition rate of the pulse of 3 MHz (i.e. $3 \cdot 10^6$ zero crossings corresponding to 1.5 MHz RF frequency) this leads to a required RF amplitude of approximately 20 kV. Without any resonant circuit and employing just a 50 Ω transmission line, a 10 MW amplifier would be necessary to provide these voltages. Thus, an appropriate resonant circuit is required. The resonance frequency of a serial resonance circuit can be determined via:

$$f_0 = \frac{1}{2 \cdot \pi \cdot \sqrt{L \cdot C}}$$

where L is its inductance and C its capacitance. In such a circuit, the voltage at the capacitor is increased depending on the Q-factor of the circuit, which depends on both the inductance and capacitance of the electric elements via the relation:

$$Q = \frac{1}{R} \cdot \sqrt{\frac{L}{C}}$$

In other words, a low capacitance leads to a high voltage increase. So, as a first attempt, a resonant circuit can be realized by simply adding an inductance to the inherent capacitance of the deflector. This capacitance was determined in a CST simulation to be 3.4 pF. This leads to a required inductance of around 3.3 mH at a frequency of 1.5 MHz. The voltage drop at the inductor is approximately equal to that at the capacitor , i.e. 20 kV on the deflector. This imposes certain limitations on the design of the coil and its size. A simple approach is an air-core coil whose inductance

L can be approximated via the equation:

$$L \approx \frac{\mu_0 N^2 A}{l}$$

where μ_0 is the vacuum permeability, N the number of windings, A is the area cover by a single coil loop and l its length. Since L depends on N^2 in this equation, it makes sense to keep N high to achieve as high a value as possible for the inductance L. Employing a coil with 100 windings, and a distance of $5\,mm$ per winding (for insulation and possible cooling), the coil would be 500 mm long and 400 mm in diameter. Since such a coil is not applicable, a high-voltage capacitor (made by COMET) with a variable capacitance between $75 - 250\,pF$ (set at $150\,pF$) was intended to be employed in parallel to the deflector plates such that two air-core coils with an inductance of $36\,\mu H$ could be used to set up the resonance circuit. In this setup, the deflector itself acts as a negligible stray capacitance, but achieves the same high-voltage as the main capacitor. Figure 5.23 shows an electrical diagram of the setup. The capacitor and coils are also shown. In experiments employing the described setup, the required voltage increase

(a) (b) (c)

Figure 5.23: (a) electrical diagram of resonant network (b) water cooled air-core coils (c) variable HV-capacitor

could not be realized, due to the low inductance/high capacitance. Moreover, the resonance is very sharp, ao that any perturbation of the resonance circuit (e.g. cables in the proximity of the coils, interfering RF signals) would lead to a drift in resonance frequency or a drop in voltage. To increase the q-factor of the circuit, the size of the coils would need to be increased, but this would also heighten the sensitivity to such perturbations.

A further argument against a resonant circuit for the deflector is the deflection concept itself: the ion-beam load on the deflector plates is highest in the case of maximum deflection (and thus maximum deflection voltage). The beam itself leads to damping of

the resonant circuit and thus to a reduction of the q-factor. Thus, the system would be intrinsically instable. To operate an RF-driven deflector employing a resonant circuit, a different setup would be required employing constant magnetic deflection. With such a deflector, the electric deflector plates themselves would be employed to produce the transmitted beam bunch.
Since the use of a resonance circuit for producing the required high voltage RF to the deflector was not possible, an alternative solution for the deflection mechanism had to be found. The solution was to employ a fast RF switch manufactured by Behlke Power Electronics GmbH [67]. Specifically, the fast HV-switch HTS 91-01 is capable of generating rectangular HV pulses of up to $9.6\,kV$ pulse voltage, at durations as short as $50\,ns$ at repetition rates as high as $3\,MHz$. The results employing this pulser for deflector operation can be found in section 5.5.

The second RF-driven device of the pulsing system is the buncher. Although the required peak voltage is much lower compared to those of the deflector above (a possible operating voltage that is selectable in the interval from $0-5\,kV$ was desired, in order to set the correct longitudinal focus, estimated to be around $3.5\,kV$), the operating frequency is much higher. Since the buncher exhibits two drift spaces, the operation frequency has to be selected such that the RF-phase of the buncher changes by 180 degrees (or multiples of the rf-period plus 180 degrees) while a beam bunch travels from the center of the first drift space, traverses the buncher tube to the center of the second drift space, in order to bunch the beam effectively at both gaps of these gaps. For deuterons a frequency of $20\,MHz$ is required in this buncher geometry, while for the helium ions the frequency can be reduced to $14\,MHz$ due to their lower velocity. The capacitance of the buncher was simulated to be $9\,pF$, but a measurement yielded a realistic value (including all stray capacitances like cables, connectors and feed-throughs) of $25\,pF$. With the latter, an inductance of approximately $5.2\,\mu H$ is required to attain the required operation frequency. However, such a low inductance leads to a very low Q of 9.1 for a 50Ω load.
By lowering the load and optimizing the geometry (reducing the capacitance by placing the coil inside the vacuum chamber) as well as employing RF-litz-wire for the coil (see figure 5.24) a much better q-factor of 20 is obtainable. This value is sufficient to reach the required value of $3.5\,kV$ employing a $1\,kW$ RF amplifier. During final high-power tests it turned out that the available $1000\,W$ RF-amplifier was not able to generate the specified power and only achieved 200 W. Thus, due to a lack of time and funding, no further experimental tests on the buncher were performed.

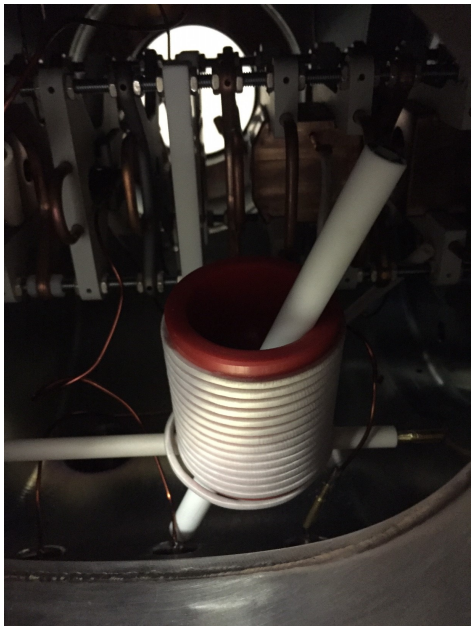

Figure 5.24: Final setup of buncher resonant circuit (the ceramic rod merely holds the coil in place)

5.5 Evaluation of the Pulsing System

Although the PBIS system was developed to produce pulsed deuteron beams, the evaluation was performed with helium ions because of radiation safety issues: At $35\,keV$ deuteron energy, the cross-section of the $D(d,n)^3He$ reaction is sufficiently large to generate fast neutrons which could not be tolerated in our experimental environment. As explained in section 5.1 the water piping in the deflector chamber had to be severed to improve the high-voltage stability of the lenses. Therefore, the pulsing system could only be evaluated during short operation cycles, i.e. producing a single few microsecond pulse (at low repetition rate) from the ion source and selecting from it a several short pulses by means of the deflector being investigated. Due to the current limit of the relay and the modifications to the ion source, only a peak current of $50\,\mu A$ for the un-chopped beam could be achieved. For this reason, these evaluation experiments can only be considered as a preliminary proof-of-principle study. In the last test performed, a $35\,kV$ He-beam was focused into the chamber of the pulsing system employing $15.4\,kV$ and $17.5\,kV$ at the first and second einzel lenses of the LEBT, respectively. The voltage signal at the $50\,\Omega$ output line of the fast-faraday cup was amplified by a Phillips Scientific 300 MHz Bipolar Amplifier (Model 6950). In the experimental set up, the distance between the entrance flange of the diagnostics chamber and the fast-faraday cup was $576\,mm$, slightly more than the flightpath inside the

DWIK RFQ to the start of the gentle buncher section. Due to the low beam current, the einzel lenses of the pulsing system were not required to improve beam quality. In another previous test, the deflecting voltage required for full beam suppression was determined. A significant suppression in beam current could already be achieved with $500\,V$ deflection, although $1.5\,kV$ would be required to stop the entire beam. This is a lower voltage compared than the simulations yielded, however, the experimental beam current was well below $1\,mA$, so that space-charge effects which are capable of increasing the beam diameter considerably, could be neglected.
To achieve beam pulsing, a rectangular pulse of $1.75\,kV$ and duration of approximately $200\,ns$ was applied to one deflector plate, whereas the second plate was connected to a variable DC voltage. Thus, the pulsing system could be operated in three different modes: In the first pulsing mode with no voltage on the second plate, the beam is just deflected away from the beam axis, if a HV-pulse is present. In the second mode with a $2\,kV$ DC voltage at the second plate, the beam is deflected away from beam axis during the pulse pauses, but is swept back on axis, if the HV-pulse is present, yielding a transmitted beam for the relevant pulse duration ($200\,ns$). Since the HV-pulser used (further details are provided in section 5.4) is only able to generate pulses down to $50\,ns$, the third operation mode is relevant to generate the required shorter pulses of approximately $30\,ns$: By deflecting the beam with only $0.75\,kV$ on the DC plate, the beam is swept over the aperture by means of the HV-pulse. Employing this method, a sequence of pulses with the duration shorter than $20\,ns$ (full width half-maximum) with a (peak-to-peak) delay of $200\,ns$ between them, could be generated. The analyzed time spectra of the beam signal in the fast-faraday cup for the three operation modes described above is shown in figure 5.25.

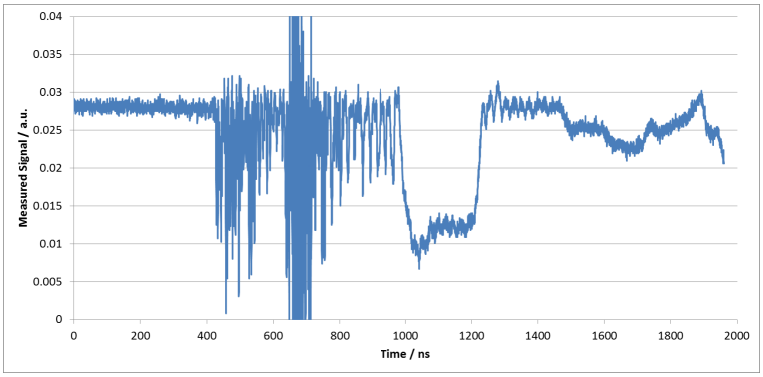

(a)

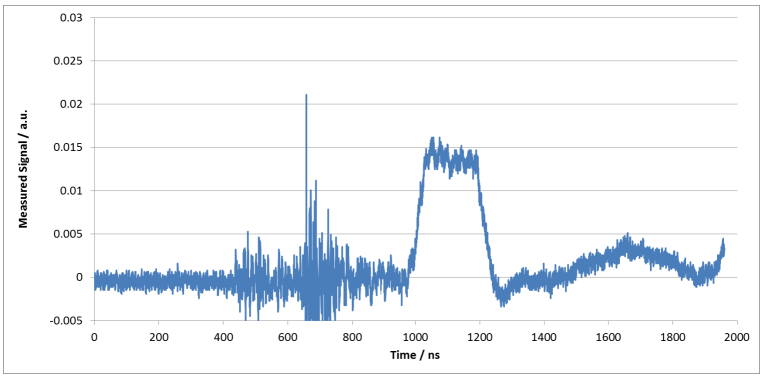

(b)

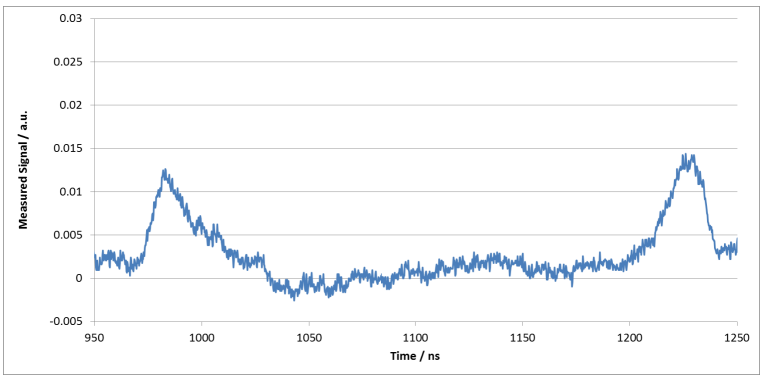

(c)

Figure 5.25: Cleaned time-spectra of the chopped helium beam for three different pulsing modes: (a) Sweeping beam out, (b) sweeping beam in, (c) sweeping beam over the aperture

A major challenge in performing these measurements was the data analysis: the very fast rise times of the HV-pulser (approximately 1 $\frac{kV}{ns}$) induces (singular - generic) intense pick-up signals on the fast-faraday cup signal, that mask the beam-current signal. Fortunately, the pick-up signal of the pulser is reproducible in shape and amplitude when the pulser is operated at the same settings for signal length, voltage and

repetition rate. Since the signal from the fast-faraday cup is measured with a fast digital oscilloscope (or wave form digitizer), the HV-pulser induced pickup signal can be measured separately without beam and subsequently, digitally subtracted from the fast-faraday cup signal taken with beam. This process is visualized in figure 5.26.

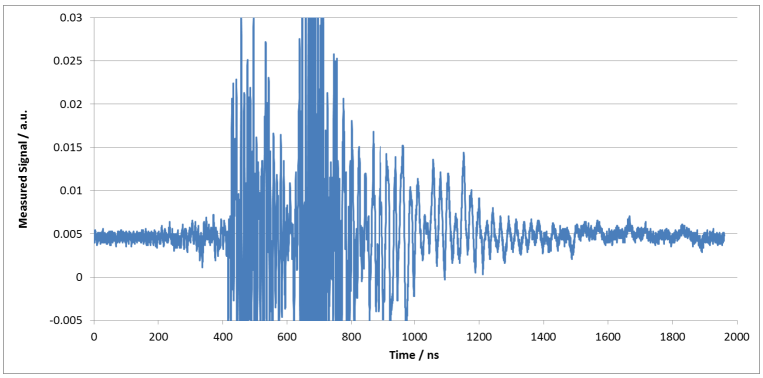

(a)

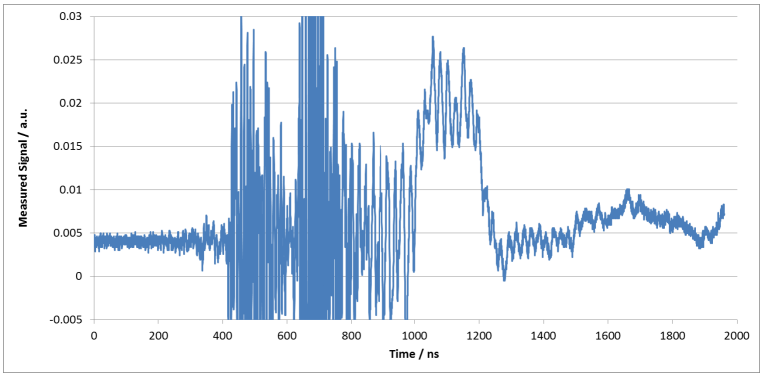

(b)

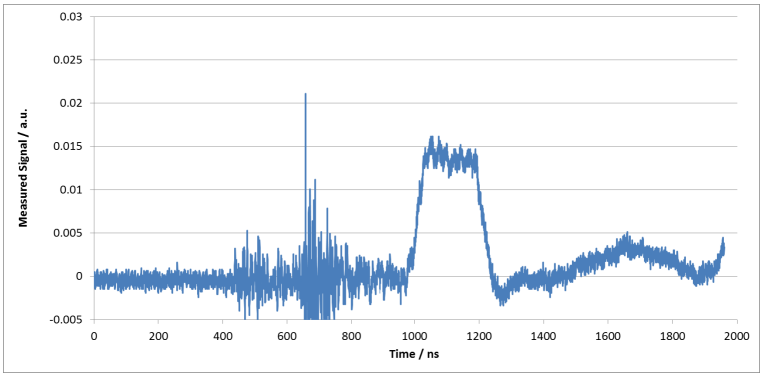

(c)

Figure 5.26: Time-spectra measured at the fast-faraday cup (a) Beam-off: RF-pickup signal from HV-pulser without beam , (b) Beam-on: raw signal from fast-faraday cup with beam, (c) subtracted curve of beam pulses only

To determine the ion species and energy of the beam, the time-of-flight between deflector and fast-faraday cup was measured in the same series of experiments. For this purpose, the HV-pulse to the deflector served as start trigger: its time delay to the fast-faraday cup signal yielded the flight time. No voltage was applied to the collimator, buncher or last einzel lens of the PBIS system, such that the particle energy was at $35\,keV$ over the entire flight path after chopping. As figure 5.27 indicates, the leading edge of the HV-pulser pick-up signal present on the fast-faraday cup signal was used as a start signal for the flight-time measurement. the latter was determined to be approximately $562\,ns$.
Taking into account the mass of the helium ions of $m_{He} = 4.0026\,u$ and the beam energy of $E_{He} = 35\,keV$ as well as the distance between the deflector aperture and the faraday cup of $l_{TOF} = 727\,mm$, via:

$$TOF_{He} = \sqrt{2 \cdot E_{He} \cdot m_{He}} \cdot l_{He}$$

the time-of-flight of the helium beam was calculated to be $TOF_{He} = 560\,ns$. Taking into account the measurement uncertainties (e.g., the flight-path of HV-pulser signal to the fast-faraday cup, which is of the order of several nanoseconds), the result of this measurement is in good agreement with that of the analytical calculation.

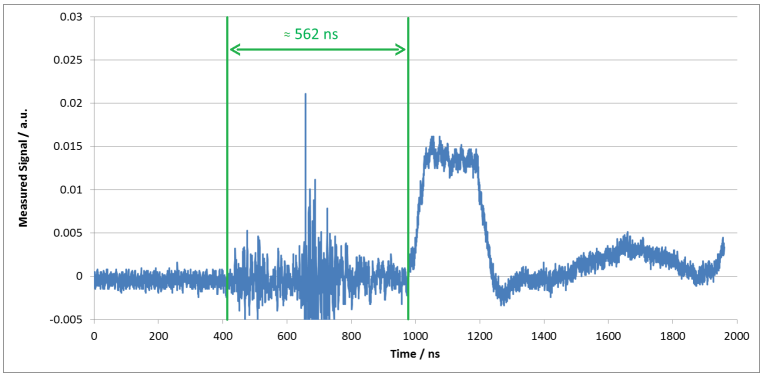

Figure 5.27: Analysis of time-of-flight measurement

6 Target Development

All previous experiments to develop methods and detectors that are presented in this thesis, were performed at low current accelerators with average beam currents of several nA (DC-equivalent) of pulsed beams. With these low current beams, it is reasonable to use a small, solid disk (several centimeter in diameter) of the desired target material. Nevertheless, despite such low beam-power, even this target needed to be wobbled or water cooled.

For an operational ACCIS System producing an average beam current of around $600\,\mu A$, a more sophisticated approach had to be found to withstand the high thermal and charge load ($\sim 3.6\,kW$ in an ACCIS field-system and $\sim 600\,W$ at the DWIK RFQ).

To test the different target designs, the PTB Ion Accelerator Facility (PIAF)[68] was employed. As figure 6.1 indicates, the facility consists of two different particle accelerators, a $3.75\,MV$, single-stage Van-de-Graaff accelerator built by High-Voltage Engineering (HVE) as well as a $19\,MeV$ CV-28 cyclotron built by The Cyclotron Cooperation. Since both machines are unable to produce high-current beams in the

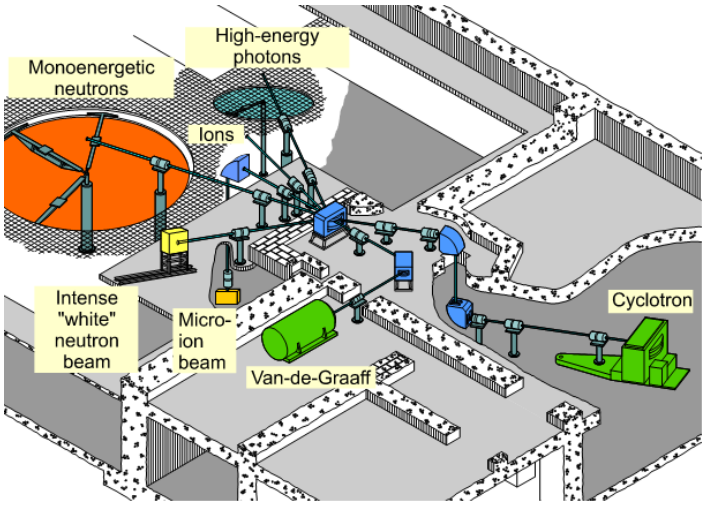

Figure 6.1: Overview of the PTB Ion Accelerator Facility

correct pulsing scheme, all target tests were performed with higher energy, continuous

wave beams, in order to dump the maximum available power on the target and evaluate its behavior concerning thermal, mechanical, vacuum and nuclear reaction based aspects.

6.1 Design of the Target

To generate the desired particle beam (a white neutron spectrum in combination with two, well separated, discrete gamma lines) the nuclear reaction $^{11}B(d, n+\gamma)^{12}C$ was proposed [15]. In a first attempt to produce a high-current ^{11}B target, enriched ^{11}B powder sintered to a disk of $3\,mm$ thickness and $66\,mm$ in diameter and brazed to a water-cooled molybdenum backing employing a silver braze, was selected as a first prototype. The raw material, $> 99\%$ enriched ^{11}B powder (grains $< 22\,\mu m$ in diameter) was supplied by Ceradyne [69]. The sintering process was performed by RHP-Technology [70] with the goal of achieving a density which is $> 85\%$ that of bulk boron.
Prior to a beam test, the high temperature and vacuum performance had to be tested. In the first test, the target was mounted in a sealed sample box and vacuum pumping employing a 300 to $400\,\frac{l}{s}$ turbo-molecular pump and a rotary-piston roughing pump was applied. The time-dependent pressure behavior without and with the boron target for the first $\sim 10000\,s$ of pumping can be found in figure 6.2. With the target, due to out-gassing or virtual leaks (probably gas pockets in the solder joint), two further days of pumping were required to reach the same vacuum base-level ($2 \cdot 10^{-6}\,mbar$) as without the boron target. Since after multiple pumping processes, no cracks could be observed on the target surface, the temperature test could be performed.

To do so, the rear-face of the target was thermally connected to a metal plate which was electrically heated. During the heating and cooling procedure images of the thermal distribution were taken by an infrared CCD camera. The image sequence of the cooling procedure is shown in figure 6.3. As the images indicate, the periphery of the target was always hotter than the inner region. The reason is obvious: not the entire target surface is brazed to the backing. A small ring at its outer edge (approximately $1 - 2\,mm$ wide) is only poorly in contact with the backing material. But, even in the central area, small inhomogeneities are visible. Nevertheless, the inhomogeneity over the central area represents no more than $20\,\%$, so the next step, particle beam tests, could be initiated.

Since the deuteron beam spot size is only $8\,mm$ in diameter an approach had to be found to homogeneously distribute the beam load over the entire area of the boron

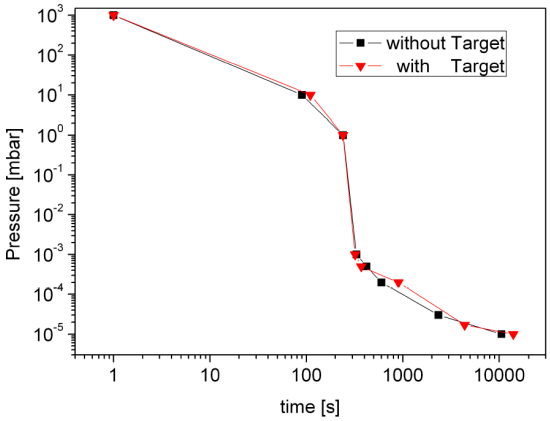

Figure 6.2: Pressure behavior with and without included boron target (first day of vacuum test)

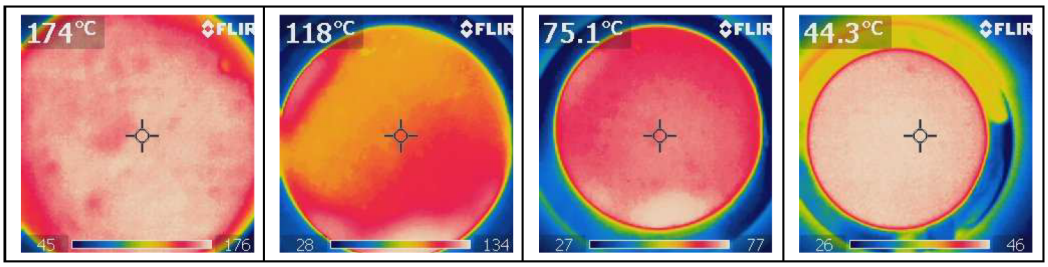

Figure 6.3: Cooling sequence of the sintered boron target (in chronological order but arbitrary time-intervals, target previously heated to 200 $°C$)

layer. Thus, the beam was wobbled over the target area in Lissajous-like figures employing an x-y target scanner, in which the x-y stepper motors are running at different rotation velocities (see figure 6.4).

In a first attempt, the target was irradiated by a 5 μA average beam current, 10 MeV, cyclotron, CW proton beam for 65 minutes. A slight vacuum deterioration from $1{\cdot}10^{-6}$ to $5{\cdot}10^{-5}$ was observed in the first few minutes of bombardment. Due to high activation of the target (probably based on ^{11}C produced by the reaction $^{11}B(p,n)^{11}C$ with a half-life of 20 minutes), an inspection of the target was delayed until the next day. Visual inspection of the irradiated target showed that, except for a crack at one side of the edge, the target disk was not damaged, as figure 6.5 shows. In the next step, the target was irradiated by a 20 μA average beam current, 10 MeV, CW deuteron beam, so the power dissipation was quadrupled to 200 W. The particle type was changed due to the high target activation during the first test. A rapid deterioration in vacuum pressure and a drop in dose rate in the accelerator experimental hall after 2 minutes of irradiation strongly suggested a problem with the target. The irradiation

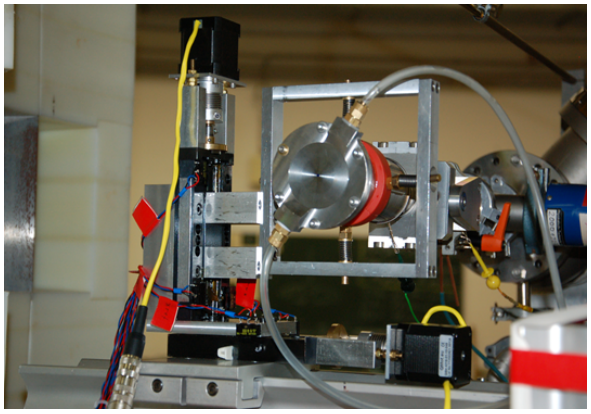

Figure 6.4: x-y target scanner with mounted, enriched ^{11}B target

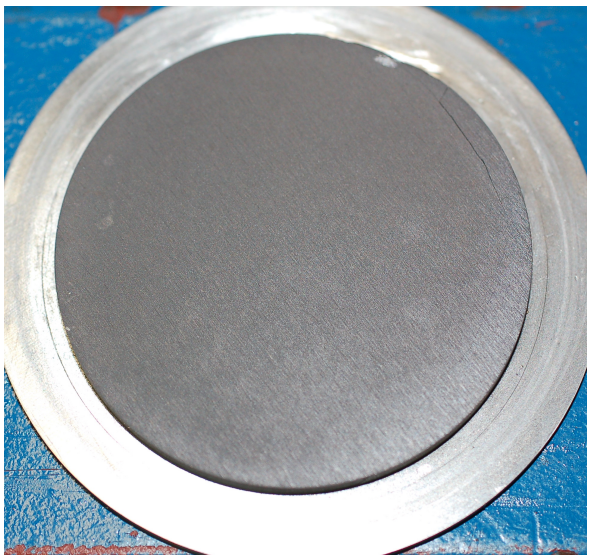

Figure 6.5: Visual inspection after first beam test (65 minutes of 50 W beam load)

was immediately stopped at this point. After a one-day pause to let the accumulated radioactivity cool down, visual inspection of the target indeed revealed that it had been completely destroyed, as figure 6.6 indicates.

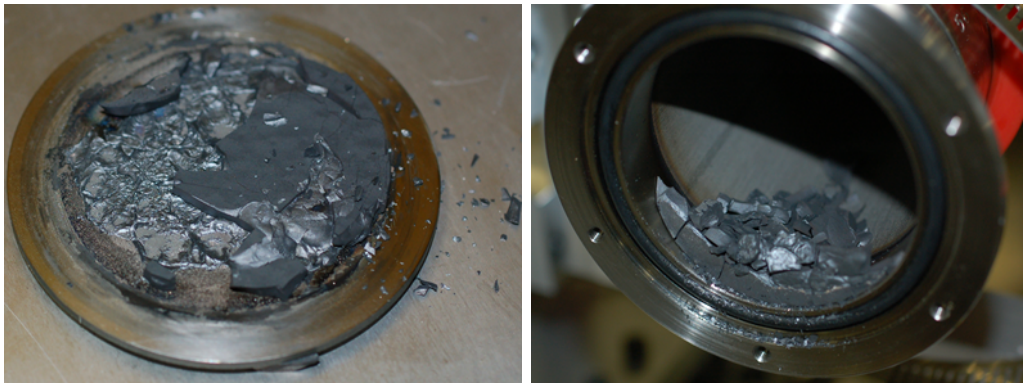

Figure 6.6: Pictures of the fragmented boron disk after 2 minutes of irradiation at a power dissipation of 200 W

A closer examination of the residual surface indicated a non-uniform welding process. Some parts of the surface exhibited a rough structure, which was interpreted such that the boron layer had not been entirely fragmented. Other parts of it exhibit a very smooth surface which could possibly be either the braze or even the blank backing. If the brazing between sintered layer and backing is not uniform, it would lead to corresponding inhomogeneities in heat conductivity and thus to a steep gradients in temperature profile of the boron surface, because the sintered Boron layer is a poor heat conductor. This induces high stresses which finally lead to the observed fragmentation of the target. Moreover, sintered boron is also a very poor electrical conductor. Due to the charged particle beam striking the target, an electric field between the grounded backing and the accumulated charge on the surface of the target might lead to voltage discharges through the boron layer.
Based on these results, the concept of using a thick sintered Boron target and brazing it to a backing was reconsidered: employing the software SRIM2013 [71], the stopping ranges for deuterons in a boron layer at different relevant impinging energies were determined (see table 6.1). As this table indicates, not more than a $300\mu m$ thick layer of boron is required to completely stop the deuteron beam at incident energies of up to $9\,MeV$ on target.
To improve the poor thermal and electrical conductivity of pure boron, a boron compound had to be found, in which the other elements do not have a major impact on the required specific gamma spectrum of pure boron, nor should the elemental dilution appreciably reduce the relevant neutron and gamma yields. Especially, these other elements should not exhibit prominent gamma yield between the two the discrete lines of interest (at $4.5\,MeV$ and above $15.1\,MeV$), when bombarded by deuterons at relevant beam energies (see further above). Furthermore, the compound should still contain

Deuteron Energy / MeV	Stopping Range / μm
4.0	77.5
4.5	94.24
5.0	112.38
6.0	152.79
7.0	198.59
8.0	249.61
9.0	305.82
10.0	367.11

Table 6.1: Simulated deuteron stopping ranges in boron target

as much boron as possible, so that most of the nuclear interactions still occur in the boron. Otherwise the required beam current will increase further.
Boron carbide (B_4C) was found to be an ideal material. Firstly, it provides a high boron content. Secondly, it is well known for its stability under intense ion bombardment, being used as plating material for divertors in plasma fusion experiments. Since literature showed data only up to $4\,MeV$ but not in the required energy regime, an experiment was performed at the PTB cyclotron, employing a higher-energy deuteron beam impinging a ^{12}C target. This test demonstrated that carbon contributes to the gamma spectrum mainly below $4\,MeV$ (as figure 6.7 indicates). The yield of higher-energy gammas is negligible. Moreover, via the nuclear reaction $^{12}C(d,n)^{13}N$, the carbon content even contributes to the neutron spectrum.

In a further experiment at the PTB cyclotron, an electro-sprayed B_4C sample-target of $25\,\mu m$ thickness and $2\,cm^2$ surface area provided by the Institute of Plasma Physics (IPP) in Munich could be tested: the beam spot was about $8\,mm$ in diameter but again the target scanner distributed the load over the entire target. The proton beam energy was $6.7\,MeV$ and the current was increased from $10\,\mu A$ initially up to $55\,\mu A$ (the maximum available current at the cyclotron). The irradiation at maximum beam-power lasted 5 hours. The overall beam-energy loss in the B_4C layer was estimated as $3.5\,MeV$, with the remaining beam power deposited in the molybdenum backing. Thus, the total power dissipated in the B_4C layer was above $192\,W$, whereas the total power deposition on the entire target assembly was $\sim 370\,W$. The total radiation energy density on B_4C could be estimated to be $400\,\frac{kJ}{cm^2}$ Representing a total absorbed dose of approximately $10^{10}\,Gy$. During the experiment, the neutron and gamma spectra were monitored, but no change in the radiation yield or spectrum was observed.

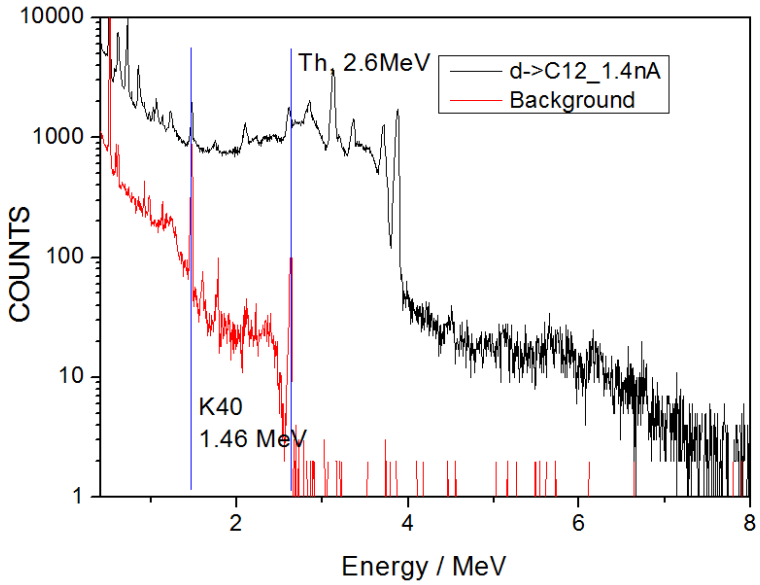

Figure 6.7: Gamma spectrum of the $^{12}C(d,\gamma)^{14}N$ reaction measured with a germanium detector. The red background signal shows the natural gamma lines of thorium and potassium-40

After irradiation, visual inspection of the target did not indicate alterations of the target, except for a color change in the irradiated region (see figure 6.8). For the

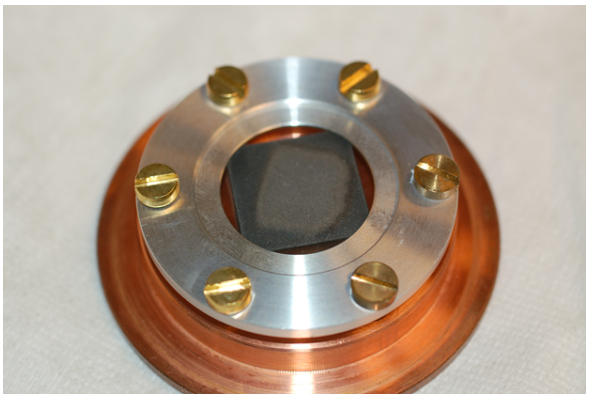

Figure 6.8: Boron carbide target from IPP after 5 hours of irradiation at maximum available beam power

further beam characterizations presented in section 6.2, targets were manufactured at LERMPS [72] employing B_4C powder (made of natural boron) and electro-spraying techniques. For experiments at the PIAF facility at PTB, a $2\,mm$ thick molybdenum disc was coated with a $200-350\,\mu m$ thick layer of B_4C. For an application of the $^{11}B(d,n+\gamma)^{12}C$ reaction at the DWIK accelerator facility, a spare tungsten rotating beam dump was coated with B_4C employing the same technique.

6.2 Characterization of Radiation Field

The neutron and gamma spectra of the $^{11}B(d, n+\gamma)^{12}C$ reaction were already measured earlier with a thick enriched boron target [21]. In this work we characterized the neutron and gamma radiation emission of B_4C at various deuteron energies, both at PIAF facility of PTB and at DWIK RFQ facility of NECSA. The employed detector and measuring techniques, as well as the results are presented and discussed in the next section.

6.2.1 Detector Setup

To characterize a fast neutron beam in terms of fluence and spectrum, scintillators constituted a widely used detection technique for many decades [73]. In a scintillator-based detector, the incident particle interacts with the scintillating material, producing, at the end of a process of several energy conversion steps, a number of photons. The photons-yield is (to a certain extent) proportional to the energy deposited by the incident particle in the scintillator material. This light can be detected by sensitive light detectors such as photo-multiplier-tubes (PMT) (see figure 6.9).

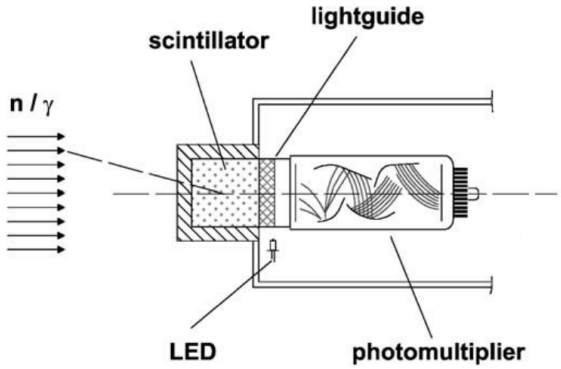

Figure 6.9: Schematic drawing of a photo-multiplier-tube based neutron and gamma detector [74]

At the photo-sensitive entrance window to the PMT (the so called photo-cathode), the incident photons are converted to electrons via the external photoelectric effect. These electrons are then multiplied in a cascade of closely-spaced electrodes(called dynodes) which are set at increasingly positive potentials. At the final electrode (the so called anode), the pulse height (which is proportional to the incident particle energy) as well as the shape of the signal which follows the time development of the incident light pulse can be analyzed.

For fast neutron detection, typically a hydrogen-rich liquid organic compound is employed as a scintillator, which is typically sensitive to neutrons as well as gammas. The mechanism of the light production of the scintillator depends on the incident particle: Whereas incident gammas undergo Compton scattering with the electrons of the scintillating material, neutrons will elastically scatter mainly with the protons. These different secondary particles (electrons/protons) lead to a varying ionization/excitation density in the scintillator, thereby populating other excited atomic or molecular levels and giving rise to different decay times. The difference in pulse shapes of detected neutron- and gamma-induced events of the frequently employed scintillator NE213 (comparable scintillators are EJ301 manufactured by Eljen Technology or BC501A manufactured by Saint-Gobain Crystals, since NE213 is no longer commercially available) are shown in figure 6.10.

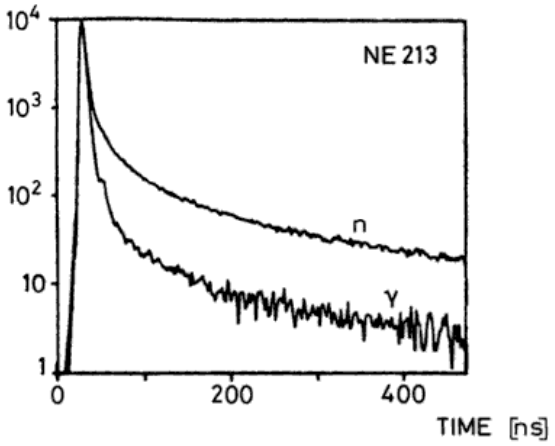

Figure 6.10: Different pulse shapes of neutron and gamma events in an NE213 scintillator [75]

To separate detected neutron events from gamma events, the different decay time (in other words pulse shape of the measured photon flash) can be employed. In Figure 6.11, an example measurement of a pulse height vs. pulse shape spectrum of a combined neutron and gamma source is presented. The spectrum shows a clear separation of two different branches: The region of neutrons is marked in red, whereas the gamma region is marked in green. As explained above, the pulse height signal is proportional to the incident particle energy. To define the energy scale, the pulse height spectrum has to be calibrated by detecting gamma lines of different radioactive sources at well known energies. Employing tabulated factors, these gamma calibrations can be recalculated to be used also for protons or other particles. The factors are called quenching factors. Concerning the determination of real energy spectra employing scintillator

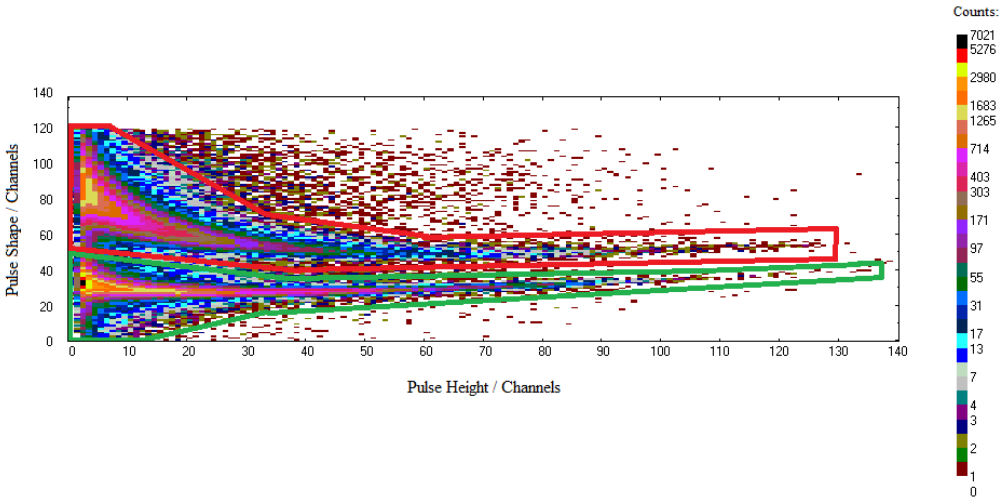

Figure 6.11: Example of a Pulse height vs. pulse shape spectrum. red: neutron events, green: gamma events

based detectors there is one complication: The light output of the scintillator is only a measure for the deposited energy. Moreover, mono-energetic neutrons or gammas do not deposit a single energy but a whole pulse height spectrum. For this reason, the resulting spectrum of a scintillator measurement has to be unfolded employing measurements of mono-energetic reference spectra (to determine the so called response function of the detector).

A second option to determine the neutron energy is employing the time-of-flight technique again (see 2.1.1): if the deuteron beam is pulsed, also a pulsed neutron beam is produced at the target. If the flight path between detector and target is well known, the time difference between the reaction at the accelerator target and the detected event in the scintillator determines the neutron velocity and thence its energy. This technique can also be used to discriminate between gamma and neutron events, since all primary gamma particles arrive at the detector with the speed of light and thus well in advance of any massive particle. [1] The spectrum derived employing this method is called the time-of-flight spectrum

If measurements are performed employing the pulse-height vs. pulse-shape characteristics as well as the time-of-flight method, the latter can be used to calibrate the detector as described above: Employing a broad energy (so called white) neutron

[1] It should be noted that time-of-flight discriminates only between source-produced neutrons and gammas. Indeed, for neutrons that interact in or near the scintillator by a (n, γ)-reaction and induce a signal in the scintillator, the corresponding secondary gamma will be counted as a neutron.

spectrum, the TOF-method can be used to measure multiple neutron transmission spectra in limited energy intervals. From these quasi mono-energetic energy spectra, a response function can then be derived and normalized to the detector efficiency. This response function can then be employed to unfold the measured fast-neutron spectra to determine the true energy spectrum of the analyzed reaction. Since at PTB, time-of-flight measurements were possible and pulse height measurements were also performed, no unfolding of the pulse-height spectra was required. The time-of-flight measurement from PTB was analyzed and pulse height spectra measured at NECSA could be compared to the reference measurements at PTB. For the characterization of the radiation field of the B_4C target an organic scintillation spectrometer consisting of a a cylindrical NE213 scintillator (2 inch long and 2 inch in diameter) was employed in two measurement campaigns: In the first, the spectrum of the target were measured under laboratory conditions with low beam currents but a high quality beam at the PTB Ion Accelerator facility. Here, the neutron as well as gamma spectrum was measured, making use of both techniques explained above. Later, the same detector was set up at DWIK accelerator at NECSA to repeat the measurement at the RFQ accelerator. In order to perform comparable measurements at both laboratories, the detector had to be modified somewhat: During the measurement campaign at NECSA, the temperature in the experimental hall occasionally exceeded $45°C$. Since detectors of this type are prone to temperature-related drifts of the pulse-height signal, each scintillating detector is usually equipped with a temperature stabilization. The stabilization is operating in a control range from 5 to $40\,°C$ [76]. Since the temperatures during the NECSA experiments were above the control range, the detector was placed inside an aluminum box together with a water cooling arrangement and several large resistors mounted on a fan-cooled radiator. To perform the temperature stabilization, the inside of the box was cooled employing a water chiller that is only roughly temperature controlled. Fine temperature stabilization is then achieved by a fast-reacting control of additional heating due to the resistor setup. The successful operation of the temperature stabilizer was validated at PTB prior to the the NECSA experiments in a climate-cabinet. Figure 6.12 shows the final setup of the detector temperature stabilization. Details of both measurement campaigns as well as their results are found in the following sections.

6.2.2 PTB Experiments

For the PTB experiments, the cyclotron was employed to produce a pulsed deuteron beam of $4\,MeV$ in energy, which bombarded the boron carbide target. The detector

Figure 6.12: Box of NE213 detector equipped with temperature stabilization

was located at the position of the neutron time-of-flight spectrometer (in the PIAF layout of figure 6.1 located on the lower floor, below the high-energy photon beamline). The distance between target and detector was $11.86\,m$. As a target, a plasma sprayed B_4C target described in section 6.1 was employed. A pulsed, incident deuteron beam (repetition rate $446.86\,kHz$ and pulse width $< 1\,ns$) with an average current of $0.3\,\mu A$ was employed to perform simultaneously TOF as well as pulse-height v. pulse-shape (PH-PS) measurements. Figure 6.13 shows the measurement results.

In this figure, a clear separation between a neutron region and a gamma region can

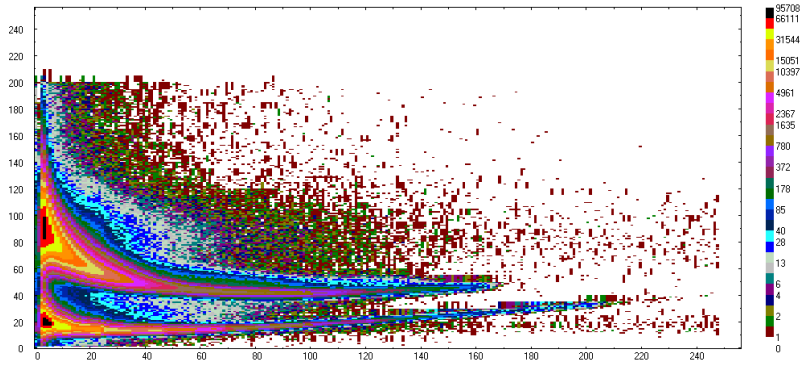

Figure 6.13: Pulse height vs. Pulse shape spectrum of deuteron on B_4C target reaction

be identified. The data in both regions can be used to calculate pulse height spectra for each event type. The pulse height spectra can then be converted into energy spectra, using gamma radiation of known energy from isotopic sources and, in the case of neutron spectra, known quenching factors of the light production for protons in the scintillator (as explained above). The same calibration can later be used to compare different neutron spectra of different measurements as well. For the energy calibration, a Na-22 source was employed. It features two peaks at energies of $511\,keV$

and 1.27 MeV (corresponding to Compton-edge energies of 341 keV and 1.06 MeV). Furthermore, an AmBe combined neutron and gamma source was employed which emits gamma rays at an energy of 4.4 MeV (corresponding to a Compton-edge energy of 4.198 MeV). The gamma-energy calibrated pulse-height spectra are shown in figure 6.14. It indicates the existence of gamma events up to 15 MeV.

However, the spectra in figure 6.14 do not show the true line energies spectra for

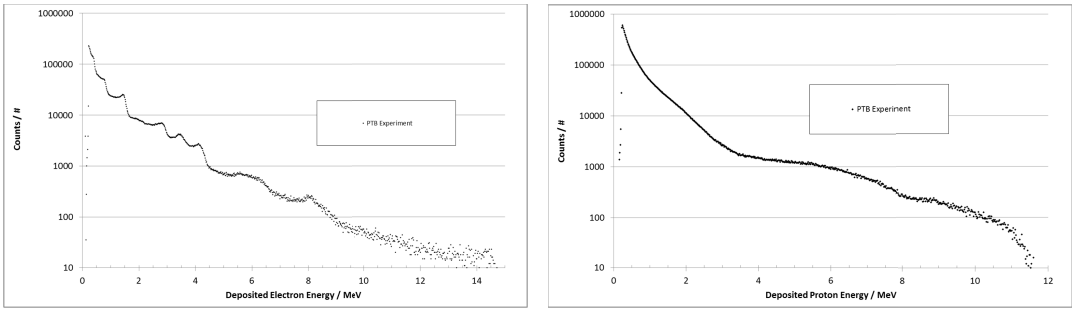

(a) (b)

Figure 6.14: Energy calibrated NE213 raw pulse-height spectrum (a) gamma events (b) neutron events

gammas or neutrons. For each of these, the entire Compton spectrum of secondary, electro-magnetic radiation produced in the scintillator is present and superposed over the lower energies. In the case of the gamma spectra, each visible feature represents the broad Compton edge of a gamma line produced in the target reaction. For instance, the Compton edge of the 4.43 MeV gamma line of the target reaction can easily be identified. Since natural boron and not pure ^{11}B was employed as target material, Compton edges of two other gamma lines, from bombardement of ^{10}B, are present between 5 and 10 MeV. To find the true gamma-line intensities emitted from the target, the spectra would have to be unfolded as described above. For neutrons, on the other hand, instead of unfolding, the neutron energy can also be determined, much more reliable from the time-of-flight measurement, taking into account the distance between target and detector of 11.86 m. Figure 6.15 shows the results of the time-of-flight measurements. The high peak at approximately 40 ns represents all measured gamma events produced in the target. The neutron energy is, in the non-relativistic approximation, proportionally inverse to the square root of time-of-flight. Since the selector frequency of the cyclotron was set to 800 kHz, the maximum time-of-flight is 1250 ns. Events that occur later will be counted at $TOF - n \cdot 1250\,ns$. The peak at 874 ns is a so called satellite peak. Here, a small fraction of beam is extracted from the cyclotron at a higher order harmonic of the selector frequency, a well known

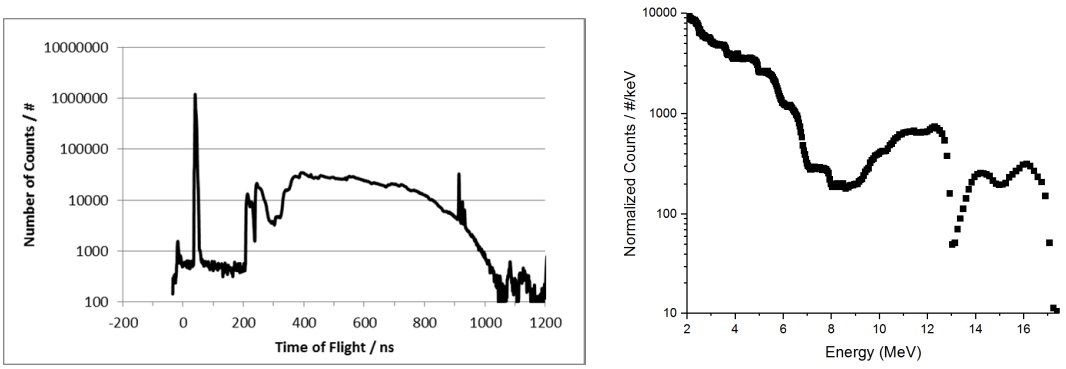

(a) (b)

Figure 6.15: (a) measured TOF spectrum (b) normalized energy spectrum

experimental artifact in such accelerators. From the flight path of 11.86 m and relying on reaction kinematics, the neutron energy can thus be reliably calculated. Due to the quadric dependence of flight-time on flight-path, the spectrum has to be normalized to the energy bin. Furthermore one needs to take the time-to-energy conversion into account as well as the fact that the gammas also have a finite time-of-flight of 39.57 ns, otherwise the rebinning will be incorrect and lead to an apparent shift to higher neutron energies than their true values. In addition, the results have to be normalized according to simulations performed by NRESP [77], which take into account (n,p) and (n,C) nuclear reactions in the scintillator itself, the geometry of the detector, the nonlinear response of the light production to different ions and their energies and the energy threshold (i.e. the cut-off energy, below which the neutron spectrum is not recorded anymore, since the number of photo-electrons produced before the charge-amplification can also be zero, within statistics).
The neutron energy spectra measured at 4 Mev deuteron energy employing a natural boron target fits well into the series of previous measurements employing a pure ^{11}B target (compare figure 2.13a). The gamma spectrum is however not sufficient for the ACCIS application, due to the presence of boron-induced gammas in the 5 to 15 MeV energy interval(see above, in section 2.3). Ultimately, for the field application the target should be manufactured employing isotopically pure (or at least highly enriched) ^{11}B.

6.2.3 Necsa Experiments

To be able to perform such experiments at the DWIK accelerator, a suitable target had to be prepared. The accelerator was equipped with a gas target (area marked in

orange), and a rotating tungsten wheel beam dump (marked red). Since a spare beam dump wheel was available, this wheel could be used to deposit a neutron and gamma radiation producing target consisting of a $250\mu m$ thick layer of B_4C employing plasma spraying techniques as described in section 6.1. Figure 6.16 [2] shows a schematic view of the DWIK target setup. Additionally, the reduced HEBT setup was employed (see

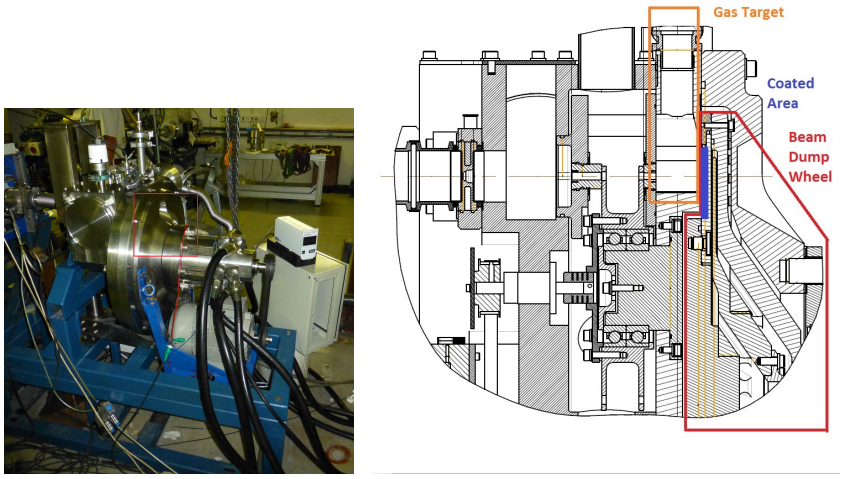

(a) (b)

Figure 6.16: DWIK gas target and beam dump wheel (a) picture (b) detailed view

chapter 3.3.3).

Since no fast-pulsing system was available at DWIK, a TOF measurement could not be performed. The deuteron beam energy in the experiments was determined to be $4.0\,MeV$ employing the TOF-probes in the MEBT of the DWIK accelerator (see 3.3). The detector was placed in the beam direction at a distance of $510\,cm$ to the target disk, as figure 6.17 indicates. During the first measurement, it turned out that the NE213 spectrometer was not able to cope with the bunch structure and the large rate at the DWIK facility: The DWIK delivered its beam in rather short bunches of approximately 400 μs with a repetition rate of $20\,Hz$ what corresponds to a duty cycle of 0.8%. The event processing time of the scintillation spectrometer and its electronics is of the order of $6\,\mu s$. This causes not only appreciable event losses due to high local dead time, but also loss of resolution due to event pile-up[3] as well as gain drift in the photo multiplier tube during a macro pulse. The DWIK accelerator was capable of accelerating a maximum average beam current of up to $2\,mA$ in the experiment. To reduce pile-up issues, the peak beam current was reduced during these measurements

[2]Private Communication - C. Franklyn, NECSA

[3]A measured pulse is produced by more than 1 absorbed particle during the same time-window of the analogue processing time of the electronic read out system

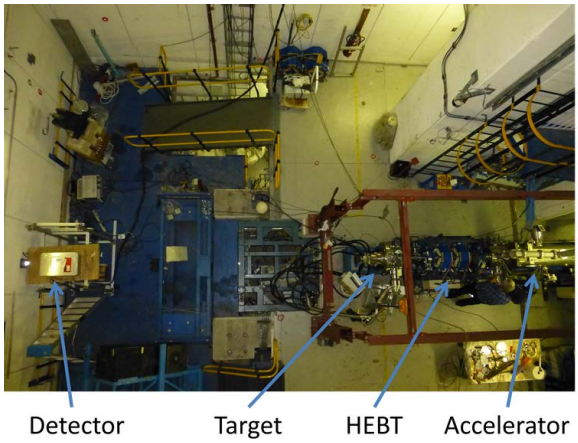

Figure 6.17: Picture of detector setup during first DWIK measurements

to 200 μA.
Since time-of-flight data could not be taken, only pulse-height vs. pulse-shape measurements were performed. By means of gamma source calibrations, the DWIK measurements were re-calibrated and compared to the spectra measured at th PTB 4 MeV deuteron beam. Since no quantitative beam current measurement was available during the DWIK experiments, the spectra were normalized to the falling edge of the first peak. Figure 6.18 shows the neutron as well as the gamma spectra comparison. Whereas the neutron spectrum fits the PTB measurements rather well, there are some

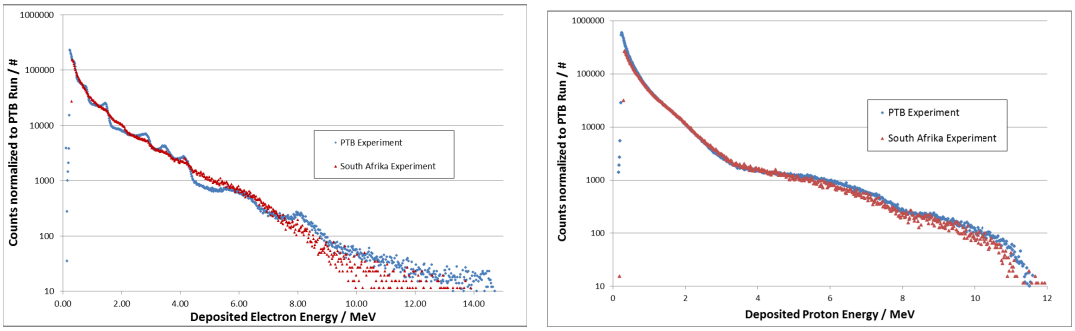

(a) (b)

Figure 6.18: Energy calibrated and normalized pulse-height spectra comparisons:(a) gamma events (b) neutron events

discrepancies in the gamma spectrum: Specifically, the gamma spectrum from NECSA exhibits less structure compared to that at PTB. Furthermore, the NECSA data do not exhibit high energy gammas above 14 MeV. This missing structure, as well as the high fluctuations above 10 MeV was attributed to pile-up and amplification loss due to current-loading of the photo-multiplier over the macro-pulse duration. Measuring

the spectrum at 90 degrees should lead to a reduced count rate due to the kinematics of the target reaction, the detector was moved from the in-beam direction to a floor above the target in the experimental hall (compare figure 6.19). Also these measure-

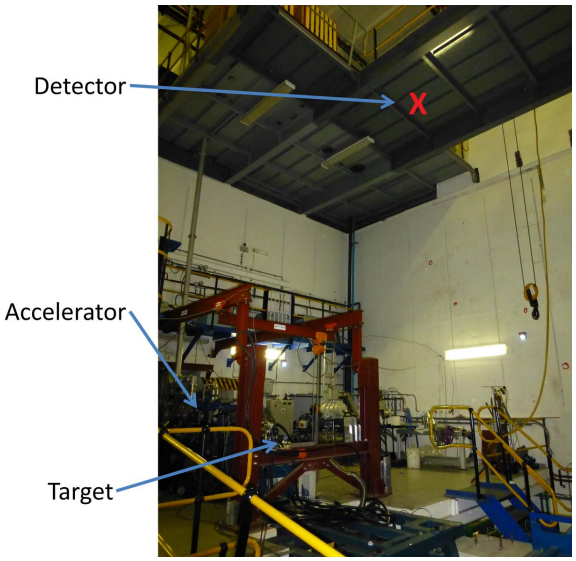

Figure 6.19: Second detector position: Above the target on top of runway

ments indicated the same result. In a final test, the smaller target disk employed in the PTB experiments was mounted instead of the target wheel, but the results remained the same. In attempting to explain the observed spectral differences, the possibility of parasitic radiation sources due to fractions of beam striking other materials than the B4C target was also considered. For this purpose, the radiation levels at NECSA - without beam - along the beamline between accelerator and target were investigated. At an aluminum aperture, just in front of the target, an intense activated spot was detected. The dose rate in close proximity to the beam tube ($\approx 10-20\,cm$) was measured as being above $100\mu Sv$ following an irradiation time of several hours. A reaction channel that may contribute to the above is the production of ^{28}Al due to inelastic neutron scattering: ^{28}Al decays by emitting a gamma at $1.78\,MeV$, with a halflife of $2.24\,min$. Since the duty cycle was only 0.8%, the activation leads to a significant event rate in between the accelerator pulses.

To summarize the target development, the target was found to be thermally and mechanically stable during all experiments. The neutron spectrum covers the required fast-neutron energy regime. The gamma spectrum is contaminated in the energy interval between $6\,MeV$ to $12\,MeV$, primarily due to the use of natural boron instead of enriched ^{11}B. The maximum deuteron energy of $4\,MeV$ during the DWIK experiments does not exhibit a sufficient yield for the $15\,MeV$ gamma line (compare [22]).

Furthermore it turned out, that a scintillator based detector using event counting techniques and analog pulse-height pulse-shape discrimination is not an appropriate detector for measurements in high-current beam-burst experiments. An alternative option could be a time-of-flight measurement employing a faster scintillator (see [78]).

7 Summary

In the framework of a joint Israeli-German research project, the feasibility of a combined fast-neutron and gamma radiography-based air-cargo inspection system was investigated. Besides the methodology of the employed imaging techniques as well as detector system development, the design of a suitable radiation source was elaborated very prominently in this research program. The work concerning the latter constitutes the central topic of this thesis: The basic concepts of the required radiation for the system was determined by studying methodology, detector and target-related issues. Thus, the target reaction of $^{11}B(d, n + \gamma)^{12}C$ was selected and the required deuteron bunch-charge of $200\,pC$ per bunch was established.

The search for a suitable deuteron accelerator was, in principle, successful with respect to RFQ accelerators: This type of compact accelerator is capable of accelerating ions to energies up to several MeV. An appropriate RFQ-design was designed in the course of this thesis: it is capable of accelerating a deuteron beam of $20\,mA$ average intensity (which leads to the bunch-charge of 200 pC in the required pulsing regime) to a final energy of $6\,MeV$, while occupying a footprint of only $7 \times 1.5\,m$. However, for the purpose of the application under examination here, such RFQ still lacks a key feature: Since both gamma- and fast-neutron based detection methods require time-of-flight experiments, the deuteron beam needs to be pulsed at a frequency of approximately $3\,MHz$, whereas each beam-burst should be shorter in duration than $1\,ns$ at the target.

Since the size of an RFQ scales inversely to its resonant frequency, the design of an RFQ operating at the above mentioned required frequency is incompatible with the inspection system footprint requirements. Thus, a novel solution was required in order to incorporate the required pulsing scheme to the beam. In the course of this work, a pulsing system located between LEBT and RFQ was conceived and its performance characteristics simulated. It is capable of performing the following operations: 1) chopping the deuteron beam into $3\,MHz$ bunches, each $10 - 30\,ns$ in duration, by means of high-voltage pulsed deflecting plates. 2) This chopper is followed by a drift-tube type buncher, to compress the bunches such that the bunching focus can be set to the beginning of the RFQ bunching section, to prevent space-charge related

bunch broadening in the first part of the RFQ. The single-bunch injection combined with the adiabatic bunching of the RFQ leads to beam pulses at the required duration and frequency.

To perform proof-of-principle experiments, a prototype of the pulsing system was manufactured. However, the pulsing and bunching properties of this prototype system could only be verified at low beam currents, since the cooling system of the pulsing assembly could not be used and the performance of the ion source was limited. The test bench comprised a CHORDIS ion source, an electrostatic LEBT as well as multiple diagnostic options. The bunching aspect of the system could not be verified for lack of time and funding to repair a defective RF amplifier.

The third main topic of this thesis was the development of a target capable of withstanding a sustained deuteron beam bombardment. Experiments employing a sintered pure boron target were unsuccessful, but an alternative manufacturing technique employing electro-spraying was found. Furthermore, the initial target material (pure boron) was replaced by boron carbide B_4C to improve the thermal and electrical conductivities.

However, experiments demonstrated that the gamma spectrum with a natural boron target is contaminated by lines between 5 and 15 MeV from reactions on ^{10}B. A future operational system would thus require isotopically enriched ^{11}B as the boron constituent of B_4C.

The target was tested and characterized at two different locations namely the PIAF facility at the Physikalisch- Technische Bundesanstalt (PTB) in Braunschweig, Germany, as well at the RFQ based accelerator facility of the South African Nuclear Energy Cooperation (NECSA) at Pelindaba, South Africa. Both experiments indicated that the neutron and gamma radiation produced at the target is suitable for the application and furthermore, the target survived the high demands of a high-power beam application.

The ACCIS project was discontinued due to a change of interest in cargo security methodology and a lack of funding. On this base the estimated costs of a demonstrator system are prohibitive. However, the radiation source presented here has multiple alternative use cases.

A different approach concerning security applications worked out by D. Brown and T. Gozani [79] called Pulsed Fast Neutron Analysis (PFNA) requires comparable beam parameters than the ACCIS system: a nanosecond-pulsed, 6 MeV deuteron beam to form mono-energetic neutrons. PFNA is not a neutron transmission imaging method. Instead, the object under investigation is activated by the neutron beam and the prompt, characteristic gamma-rays of different isotopes are detected by gamma detec-

tors to obtain element sensitive, three dimensional information.
But there are not only security applications for element sensitive imaging: Also for industry, neutron imaging with high spatial resolution is of interest. In opposition to x-ray imaging, neutrons can offer high contrast for organic materials in an heavily shielded environment [80].
Neutron time-of-flight capabilities are furthermore required for ongoing neutron metrology in several laboratories all over the world. The typical accelerator system in use here is a Van-de-Graaf or tandem accelerator due to their compactness and flexibility. The presented compact, high-intensity RFQ accelerator employing the nanosecond pulsing system might be a suitable alternative for the present DC-accelerators, which can in principle supply significantly higher radiation intensities.
Although the main achievement of the here presented accelerator system is the nanosecond pulsing which allows for time-of-flight fast neutron measurements, compact and accelerator based thermal and cold neutron sources are of great interest in the research community [81]: Most of the neutron research in the past decades was performed employing research reactors. Since many reactors are about to be (or are already) shut down, suitable replacements have to be found. While spallation sources are the high-end of this development which due to their investment costs of a billion euro and more are available only to a selected number of well established experiments, there is a demand for low-cost solutions for instrumentation and method development. High-intensity linear accelerators in combination with a suitable target for efficient neutron production and a moderator setup seem to be reasonable candidates and a valid alternative for low- and medium-scale research reactors. The presented RFQ accelerator with a moderately fast (ms) pulsing system in combination with a beryllium target and a moderator setup might be a suitable small scale system for thermal neutron research and applications.

List of Abbreviations

ACCIS Automated Contraband-in-Cargo Interrogation System

BAM German Federal Institute of Material Research and Testing

BMBF German Federal Ministry of Education and Research

CHORDIS Cold or HOt Reflex Discharge Ion Source

CW Continuous Wave

DDEGR Dual Discrete Energy Gamma Radiography

DTL Drift Tube Linac

DWA Dielectric Wall Accelerator

DWIK Diamonds WIthin Kimberlite

EMC Electromagnetic Compatibility

FNRR Fast Neutron Resonance Radiography

FRMII Forschungs-Reaktor München II

GB Gentle Buncher

HE High Energy

HEBT High Energy Beam Transport

HV High Voltage

IS Ion Source

LANL Los Alamos National Laboratory

LE Low Energy

LEBT Low Energy Beam Transport

MCP Multi Channel Plate

MOST Israeli Ministry of Science and Technology

NECSA Nuclear Energy Corporation of South Africa

OPA Optical Pre-Amplifier

PBIS Pulsed Beam Injection System

PCB Printed Circuit Board

PFNA Pulsed Fast Neutron Analysis

PH Pulse Height

PIAF PTB Ion Accelerator Facility

PMT Photo-Multiplier Tube

PS Pulse Shape

PTB Physikalisch-Technische Bundesanstalt

RF Radio Frequency

RFQ Radio-Frequency Quadrupole

RI RI Research Instruments GmbH

RM Radial Matching

SNM Special Nuclear Material

TATP Tri-Acetone Tri-Peroxide, improvised explovive

TOF Time-of-Flight

TRECOR Time Resolved Event Counting Optical Radiation detector

TRIOR Time Resolved Integrating Optical Radiation detector

TSA Transport Security Agency

List of Figures

Bibliography

[1] J. Petersen. Air freight Industry - White Paper. *The Supply Chain and Logistics Institiue, Georgia Institute of Technology*, 2007.

[2] UK Civil Aviation Authorit. Aviation Trends Quarter 3. *http://www.caa.co.uk/docs/80/AviationTrends_Q3_2013.pdf*, 2013.

[3] Bundesverband der Deutschen Luftverkehrswirtschaft. Report Luftfahrt und Wirtschaft. *http://www.bdl.aero/*, 2013.

[4] European Parliament and Council of the European Union. Verordnung (EG) Nr. 2320/2002 des europäischen Parlaments und des Rates. *Amtsblatt der Europäischen Union* *http://eur-lex.europa.eu/LexUriServ/LexUriServ.do?uri=OJ:L:2002:355:0001:0021:DE:PDF*, 2002.

[5] European Comission. Verordnung (EU) Nr. 185/2010 der Komission. *Amtsblatt der Europäischen Union* *http://eur-lex.europa.eu/LexUriServ/LexUriServ.do?uri=OJ:L:2010:055:0001:0055:DE:PDF*, 2010.

[6] Bart Elias. Air Cargo Security. *CRS Report for Congress*, 2007.

[7] 110th Congress. Implementing Recommendations of the 9/11 Comission Act of 2007. *US Public Law 110-53*, 2007.

[8] TSA Public Affairs. TSA and EU Achieve Unprecedented Air Cargo Security through Agreement. *Press Release,* *http://www.tsa.gov/press/releases/2012/06/01/tsa-and-eu-achieve-unprecedented-air-cargo-security-through-agreement*, 2012.

[9] The German Federal Ministry of Education and Research. Research for Civil Security - Cooperation between Germany and Israel in civil security research. 2010.

[10] Ilan Mor. High spatial resolution fast-neutron imaging detectors for Pulsed Fast-Neutron Transmission Spectroscopy. *2009 JINST 4 P05016*, 2009.

[11] M. B. Chadwick et al. ENDF/B-VII.0: Next Generation Evaluated Nuclear Data Library for Nuclear Science and Technology. *Nuclear Data Sheets, Vol. 107, Iss. 12,*, 2006.

[12] Ilan Mor et al. Reconstruction of Material Elemental Composition Using Fast Neutron Resonance Radiography. *Physics Procedia*, 2015.

[13] David Vartsky et al. Novel detectors for fast-neutron resonance radiography. *Nucl. Instrum. Meth. A623 pp. 603-605*, 2010.

[14] The 83rd United States Congress. Atomic Energy Act of 1954. *United States Federal Law*, 1954.

[15] M. B. Goldberg. Method and System for Detecting Substances such as Special Nuclear Materials. *U.S. Patent 7381962*, 2008.

[16] Michal Brandis. Development of a Gamma-Ray Detector for Z-Selective Radiographic Imaging. *PhD Thesis, Hebrew University of Jerusalem*, 2013.

[17] Thomas G. Miller et al. Contraband detection using neutron transmission. *Proc. SPIE 2936*, 1997.

[18] National Research Council. The Practicality of PFNTS for Aviation Security. *NAS Panel report*, 1999.

[19] Volker Dangendorf. Multi-Frame Energy-Selective Imaging System for Fast-Neutron Radiography. *IEEE Trans. Nucl. Sci. Vol. 56, No. 3, pp. 1135 - 1140*, 2009.

[20] S. Schossler et al. Time and position sensitive single photon detector for scintillator read-out. *Journal of Instrumentation Volume 7*, 2012.

[21] M. Brandis et al. Nuclear-Reaction-Based Radiation Source For Explosives-And SNM-Detection In Massive Cargo. *AIP Conference Proceedings, Vol 1336*, 2011.

[22] M. Brandis et al. Nuclear-Reaction-Based Radiation Source For Explosives-And SNM-Detection In Massive Cargo. *AIP Conference Proceedings, Volume 1336, Issue 1, p.711-716*, 2011.

[23] British Airways World Cargo. Unit Load Devices / Aircraft Dimensions; `http://www.baworldcargo.com/configs/BAWCconfigurations.pdf`.

[24] S.T. Melnychuk. Operation Characteristics of a High Current Electrostatic Accelerator for a Contraband Detection System. *Proceedings of the 1999 Particle Accelelerator Conference, New York*, 1999.

[25] R. Baartman. Space Charge Limit in Separated Turn Cyclotrons. *Proceedings of Cyclotrons2013, Vancouver*, 2013.

[26] L.M.Onischenko et al. Current Limit in the Compact Cyclotron with External Injection. *Proceedings of Cyclotrons and Their Applications, Italy*, 2007.

[27] I.M. Kapchinskii and V.A. Teplyakov. Linear ion accelerator with spatially homogeneous strong focusing. *Instrum. Exp. Tech. No. 2*, 1970.

[28] L. M. Young et al. High Power Operations of LEDA. *LA-UR-00-3650, Proceedigs of the LINAC 2000 Conference*, 2000.

[29] Ernest D. Courant et al. The Strong-Focusing Synchrotron - A New High Energy Accelerator. *Phys. Rev. 88*, 1952.

[30] Philipp Fischer. Ein Hochleistungs-RFQ-Beschleuniger für Deuteronen, Doktorarbeit. *Goethe Universität, Frankfurt am Main*, 2007.

[31] T. Wangler. *RF Linear Accelerators*. John Wiley and Sons, Inc., 2008.

[32] V. A. Teplyakov et al. *Sov. Phys. Tech. Phys. 22*, 1977.

[33] R. W. Hamm et al. The RF Quadrupole Linac: A new low Energy Accelerator. *Proc. International Conference on Low Energy Ion Beams 2, pp. 54*, 1980.

[34] B. Koubek et al. Development of a 325 MHz 4-rod RFQ. *Proceedings of 2011 Particle Accelerator Conference, New York*, 2011.

[35] K. Crandall et al. RFQ Design Codes. *LA-UR-96-1836*, 1996, revised 2005.

[36] Frank Brown. Introduction to Bessel Functions. *Courier Dover Publications*, 2012.

[37] K. R. Crandall and D. P. Rusthoi. Trace 3-D Documentation. *LA-UR-97-88*, 1997.

[38] K. Halbach et al. SUPERFISH - A Computer Program for Evaluation of RF Cavities with Cylindrical Symmetry. *Particle Accelerators 7, pp. 213-222*, 1976.

[39] CST - Computer Simulation Technologies. Microwave Studio Suite. *www.cst.com*, 2014.

[40] W.D. Kilpatrick. Criterion for Vacuum Sparking Designed to Include Both RF and DC. *Review of Scientific Instruments 28*, 1957.

[41] Joseph R. Davis. Copper and Copper Alloys. *ASM International*, 2001.

[42] K.-H. Grote et al. Dubbel, Taschenbuch für den Maschinenbau. *Springer*, 2007.

[43] The South African Nuclear Energy Corporation SOC Limited (Necsa).

[44] Arbeitsgruppe Ionenbeschleuniger - Institut für Angewandte Physik - Goethe Universität Frankfurt am Main. Webpage: `http://iaprfq.physik.uni-frankfurt.de/RFQ_Home/Home.html`.

[45] NTG Neue Technologien GmbH and Co. KG. `www.ntg.de`.

[46] De Beers Consolidated Mines, Kimberley, South Africa - `http://www.debeersgroup.com/`.

[47] J. Häuser et al. Properties of spiral loaded cavities. *Nucl. Inst. and Meth., Volume 135, Issue 3, p. 409-414*, 1976.

[48] L. M. Young. Parmela. *Los Alamos National Laboratory report LA-UR-96-1835*, Revised 2013.

[49] Stanley Humphries, Jr. Principles of Charged Particle Acceleration. *John Wiley and Sons*, 1986.

[50] S. S. Kurrenoy et al. Progress with SNS Fast Beam Chopper. *Proceedings of the 2001 Particle Accelerator Conference, Chicago*, 2001.

[51] D. Noll et al. Rebuncher Cavities for the FRANZ Bunch Compressor. *Proceedings of Linear Accelerator Conference LINAC2010, Tsukuba, Japan* , 2010.

[52] R. W. Hamm et al. A single pulse sub-nanosecond proton rfq. *Conference Proceedings of the 10th International Topical Meeting on Nuclear Applications of Accelerators, Knoxville*, 2011.

[53] Gerald Dugan. Introduction to Accelerator Physics. *USPAS Accelerator School*, Jan 2002.

[54] Webpage: Wikipedia. `https://en.wikipedia.org/wiki/Einzel_lens`. checked 2018.

[55] U.Schumann et al. Break Down Voltage of Electrode Arragnemenmts in Vacuum Circuit-Breakers. *IEEE Transactions on Dielectrics and Electrical Insulation*, 2003.

[56] K. W. Leo et al. Einzel lens chopper and behavior of the chopped beam in the KEK digital accelerator. *Phys. Rev. ST Accel. Beams 16*, 2013.

[57] Tokuyama Corporation, Japan. Datasheet of Machinable AlN ceramics SHAPAL Hi M-soft. *http://www.tokuyama.co.jp/*.

[58] METOXIT AG, Switzerland. Datasheet for Alumina Ceramics. *http://www.metoxit.com/*.

[59] MTC Wesgo Metals, USA. Cusil-ABA Datasheet. *http://www.wesgometals.com/*.

[60] Emerson and Cuming. Stycast 2850 FT - Thermally Conductive Epoxy Encapsulant. *http://research.physics.illinois.edu/bezryadin/labprotocol/stycast2850.pdf*.

[61] R. Keller et al. A High-Current Ion Source System for Gases and Non Volatile Elements. *Proc. Int. Ion Engeneering Conf., Kyoto, p. 25-30*, 1983.

[62] R. Keller et al. New developments with a high-current ion source. *Proc. IEEE PAC*, 1987.

[63] Danfysik A/S. Gregersensvej 8, DK-2630 Taastrup, Denmark.

[64] Danfysik. Datasheet of the Chordis Source Model 921A.

[65] B.Torp et al. Highcurrent ion beams of metallic elements. *Rev. Sci. Instrum. 61*, 1990.

[66] Bernhard Wolf. Handbook of Ion Sources. *CRC Press*, 1995.

[67] Behlke Power Electronics GmbH. *Am Auernberg 4, 61476 Kronberg im Taunus, http://www.behlke.com*.

[68] H. J. Brede et al. The Braunschweig accelerator facility for fast neutron research: 1: Building design and accelerators. *Nucl. Instr. and Meth., Vol. 169, Iss. 3*, 1980.

[69] Ceradyne, Inc. 3M 11B Enriched Boron Datasheet. *Quapaw, OK, USA*.

[70] RHP-Technology GmbH. *Forschungs- und Technologiezentrum, 2444 Seibersdorf, Austria*.

[71] J.F. Ziegler. SRIM - The Stopping and Range of Ions in Solids. *Lulu Press Co.*, 2009.

[72] LERMPS - Laboratory of Studies and Research on Materials, Processes and Surfaces, Université de Technologie de Belfort Montbéliard, France, 2014.

[73] J. B. Birks. The Theory and Practice of Scintillation Counting. *Pergamon Press*, 1964.

[74] H. Klein et al. Neutron and photon spectrometry with liquid scintillation detectors in mixed fields. *Nucl. Instr. and Meth. A 479*, 2002.

[75] F.J. Lynch. Basic Limitation of Scintillation Counters in Time Measurements. *IEEE Transactions on Nuclear Science 22*, 1975.

[76] Kai Tittelmeier et al. Stabilization of Scintillation Detectors. *PTB Laboratory Report*, 2003.

[77] G. Dietze et al. NRESP4 and NEFF4 - Monte-Carlo Codes for the Calculationof Neutron Response Functions and Detector Efficiencies for NE 213 Scintillation Detectors. *PTB Bericht PTB-ND-22*, 1982.

[78] Ronald Lauck et al. Low-Afterglow, High-Refractive-Index Liquid Scintillators for Fast-Neutron Spectrometry and Imaging Applications. *IEEE Trans.Nucl.Sci.56*, 2009.

[79] D. Brown and T. Gozani. Cargo inspection system based on pulsed fast neutron analysis. *Nuclear Instruments and Methods in Physics Research Section B*, 2001.

[80] Christian Grünzweig et al. Progress in Industrial Applications using Modern Neutron Imaging Techniques. *Physics Procedia Vol.43*, 2013.

[81] U. Rücker et al. The Jülich High Brilliance Neutron Source Project. *Eur. Phys. J. Plus*, 2016.